

# **Numerical Modelling of Zonal Winds on Gas Giants**

Dissertation

zur Erlangung des mathematisch-naturwissenschaftlichen Doktorgrades

“Doctor rerum naturalium”

der Georg-August-Universität Göttingen

im Promotionsstudiengang Physik

der Georg-August University School of Science (GAUSS)

vorgelegt von

**Paula N. Wulff**

aus Kanazawa, Japan

Göttingen, 2023

Betreuungsausschuss

Prof. Dr. Ulrich R. Christensen  
Max-Planck-Institut für Sonnensystemforschung, Göttingen, Germany

Dr. Johannes Wicht  
Max-Planck-Institut für Sonnensystemforschung, Göttingen, Germany

Prof. Dr. Andreas Tilgner  
Georg-August University School of Science (GAUSS), Göttingen, Germany

Mitglieder der Prüfungskommision

Referent: Prof. Dr. Ulrich R. Christensen  
Max-Planck-Institut für Sonnensystemforschung, Göttingen, Germany

Korreferent: Prof. Dr. Andreas Tilgner  
Georg-August University School of Science (GAUSS), Göttingen, Germany

Weitere Mitglieder der Prüfungskommission:

Prof. Dr. Stefan Dreizler  
Georg-August University School of Science (GAUSS), Göttingen, Germany

Prof. Dr. Wolfram Kollatschny  
Georg-August University School of Science (GAUSS), Göttingen, Germany

PD Dr. Olga Shishkina  
Max-Planck-Institut für Dynamik und Selbstorganisation

Prof. Dr. Hardi Peter  
Max-Planck-Institut für Sonnensystemforschung, Göttingen, Germany

Tag der mündlichen Prüfung: 25.10.2023

© Paula N. Wulff



This work is distributed under a  
Creative Commons Attribution 3.0 License

Printed in Germany



# Contents

<b>1</b>	<b>Introduction</b>	<b>9</b>
1.1	Surface Zonal Winds on the Gas Giants . . . . .	9
1.2	Gas Giant Interiors . . . . .	12
1.2.1	Gravimetry . . . . .	14
1.2.2	Kronoseismology . . . . .	18
1.2.3	<i>Ab-Initio</i> Models . . . . .	18
1.2.4	Experiments . . . . .	20
1.2.5	Magnetic Fields . . . . .	20
1.3	Surface Processes . . . . .	22
1.3.1	Eddies . . . . .	23
1.3.2	Vortices . . . . .	23
1.3.3	Meridional Flow . . . . .	25
1.4	Theory . . . . .	26
1.4.1	Governing Equations . . . . .	26
1.4.2	Adiabatic Reference State and Convective Perturbations . . . . .	28
1.4.3	Non-Dimensionalisation . . . . .	30
1.4.4	Characteristics of a Rotating System . . . . .	31
1.4.5	Flows with Stable Stratification . . . . .	32
1.4.6	Planetary Magnetic Fields and Zonal Flows . . . . .	33
1.5	Models for (Deep) Zonal Jets . . . . .	34
1.5.1	Theoretical . . . . .	34
1.5.2	Numerical . . . . .	38
1.6	Numerical Models and their Limitations . . . . .	40
1.6.1	Numerical Technique . . . . .	40
1.6.2	Limitations . . . . .	41
<b>2</b>	<b>Zonal Winds in the Gas Planets driven by Convection above a Stably Stratified Layer</b>	<b>45</b>
2.1	Introduction . . . . .	45
2.2	Numerical Methods and Model Set-Up . . . . .	48
2.2.1	Hydrodynamic Equations . . . . .	48
2.2.2	Background Profiles . . . . .	49
2.2.3	Numerical Methods . . . . .	50
2.2.4	Parameter values . . . . .	51
2.3	Diagnostic Methods . . . . .	52
2.3.1	Penetration Distance . . . . .	52

## Contents

---

2.3.2	Force Balance . . . . .	53
2.4	Results . . . . .	54
2.4.1	The pattern and distribution of Zonal Winds . . . . .	54
2.4.2	Zonal wind penetration distance . . . . .	58
2.4.3	Force Balance . . . . .	60
2.4.4	Varying the Background Density Profile . . . . .	60
2.5	Discussion and Conclusions . . . . .	62
<b>3</b>	<b>The Effects of a Stably Stratified Region with radially varying Electrical Conductivity on the Formation of Zonal Winds on Gas Planets</b>	<b>65</b>
3.1	Introduction . . . . .	65
3.2	Methods . . . . .	68
3.2.1	MHD Equations . . . . .	68
3.2.2	Hydrodynamic Control Parameters . . . . .	69
3.2.3	Stably Stratified Layer . . . . .	70
3.2.4	Magnetic Parameters . . . . .	70
3.2.5	Numerical Methods . . . . .	71
3.3	Results . . . . .	73
3.3.1	Zonal Wind Distribution . . . . .	73
3.3.2	Flow Amplitude Versus Depth . . . . .	76
3.3.3	Magnetic Field Induction . . . . .	78
3.3.4	Zonal Wind Truncation Mechanism . . . . .	80
3.3.5	Anelastic Simulations . . . . .	82
3.4	Discussion and Conclusions . . . . .	83
<b>4</b>	<b>Conclusion and Outlook</b>	<b>85</b>
4.1	Depth and Extent of Stably Stratified Layer . . . . .	86
4.2	Downward Continuation of Zonal Winds . . . . .	88
4.3	Further Work . . . . .	88
<b>Bibliography</b>		<b>91</b>
<b>Appendix</b>		<b>102</b>
<b>Acknowledgements</b>		<b>103</b>
<b>Publications and Presentations</b>		<b>105</b>
<b>Curriculum Vitae</b>		<b>107</b>

# Summary

The outer regions of both Jupiter and Saturn feature strong, alternately eastward and westward zonal winds. Cloud tracking has yielded latitudinal profiles of these winds, which are essentially steady in time and cover all latitudes, albeit diminished in amplitude at the mid-high latitudes. The Juno and Cassini missions at Jupiter and Saturn, respectively, have recently made *in-situ* measurements of the gravity moments and the magnetic potentials. These help to reveal how processes observed on the surface may be linked to their interiors. The gravity moments hold information about the mass fluxes in the outer envelopes of the respective planet. They have revealed that the zonal winds observed on the surface must extend deep into the planets' convective regions, from the 1 bar surface to  $> 10^4$  bar pressure levels. In both gas giants there is a transition from molecular hydrogen to metallic hydrogen as pressure and temperature increase with depth. This leads to a smooth increase in electrical conductivity from being negligible in the outer envelope to highly conducting. The magnetic field measurements help to constrain the interaction between the strong zonal winds and the deeper conducting regions.

However, numerical simulations have had difficulties in reproducing winds that form at the higher latitudes and are quenched at these inferred depths, in the same models. This thesis addresses this conundrum and shows that the key structural element is a stably stratified layer. In this region, radial flows are inhibited and convection is quenched. How this can also lead to a damping of zonal winds and a decoupling from underlying conducting regions is explored in two studies.

Firstly, purely hydrodynamic numerical models are investigated. These explore the effects of the degree of stratification, of a stably stratified region on the formation of zonal winds in a convective envelope above. For models with strongly stratified layers, the winds formed in the convective layer above reach the high latitudes. How far these zonal winds then penetrate into the underlying stable region is analysed and found to be dependent both on degree of stratification, and the width of the jet. Furthermore, the structure of the zonal jets changes when reaching the stable region and they are no longer invariant along the axis of rotation, as they are in the convective region.

A second degree of complexity is then added by including magnetic effects. This is done by implementing a radially varying electrical conductivity, increasing with depth, and imposing a magnetic dipole at the inner boundary of the simulated spherical shell, a proxy for a dynamo below. We analyse how this combination affects the zonal winds formed in an overlying convecting region, and how deep they penetrate into the stably stratified and moderately conducting regions. The winds are quenched in the stable region, with their penetration into the stratified layer being dependent on the local product of the squared magnetic field strength and the electrical conductivity,  $B^2\sigma$ .

In both studies, the key mechanism for the drop-off of the zonal wind amplitude is a merid-

## Summary

---

ional circulation which introduces a latitudinal perturbation of the density structure in the stable layer. In the hydrodynamic study this leads to a comparatively gradual drop-off in zonal wind amplitude, unlike the steep decay inferred from the gravity measurements. In the magnetohydrodynamic study, the quenching of zonal winds is more efficient. This is due to electromagnetic forces deeper in the stable region, which drive meridional flow. Our simulations suggest that the presence of stable stratification that reaches upwards into a region of weak conductivity is essential for maintaining strong winds at mid-to-high latitudes, that drop off at a depth that is consistent with constraints from the measured gravity and magnetic fields.

# 1 Introduction

This introduction seeks to give a comprehensive context to the publications associated with this work. Firstly, an overview is given of the main focus of the study: the measured surface zonal winds on Jupiter and Saturn. This is followed by a systematic description of our current understanding of gas giant interiors, and what measurements have brought us to this stage. Building up numerical models which seek to replicate, and thereby understand, the features of these zonal winds requires this grasp of processes deeper in the planets as they help to constrain the structure of the outer envelopes, in particular their stratification and conducting regions.

Some theory on the nature of rotating fluids is also presented in this introduction. This aims to provide a deeper understanding of the approximations made using the numerical methods and how we can then use them to draw conclusions about gas giant interiors.

## 1.1 Surface Zonal Winds on the Gas Giants

Zonal winds refer to longitudinally averaged (i.e. axisymmetric) east-west travelling winds, measured in the reference frame of a rotating planet. Therefore an eastwards jet is super-rotating, or prograde, while a westwards jet is sub-rotating; retrograde. The reference frame is easy to define for terrestrial planets which rotate as solid bodies. However, for the gas giants there are two additional potential complications:

- as the gas giants are fluid, aside from a relatively small inner core, they may experience deep differential rotation, extending into the planet on concentric cylinders,
- their rotation rates are more difficult to determine. For Jupiter the rotation rate of its magnetic field can be used as its axis is tilted by around  $10^\circ$  from its spin axis (May et al. 1979, Riddle and Warwick 1976), similar to that of the Earth. For Saturn the two axes are almost perfectly aligned so its rotation rate cannot be as well determined by the same method.

Zonal flows are a wide-spread phenomenon in planetary atmospheres, e.g. the Earth's atmospheric jet streams. They can be excited by interaction of the rotation of the planet with some source of energy, i.e. solar irradiation, thermal, or compositional convection. However, on the gas planets they dominate the dynamics of their outer convective envelopes as they are not hampered by topography or under the influence of strong seasonal variations - solar irradiance at Jupiter and Saturn is 3.7% and 1.1% of that at Earth, respectively. The regions between the alternating flows have been named "belts" and "zones"; belts are regions of cyclonic vorticity while zones have anticyclonic vorticity. On Jupiter

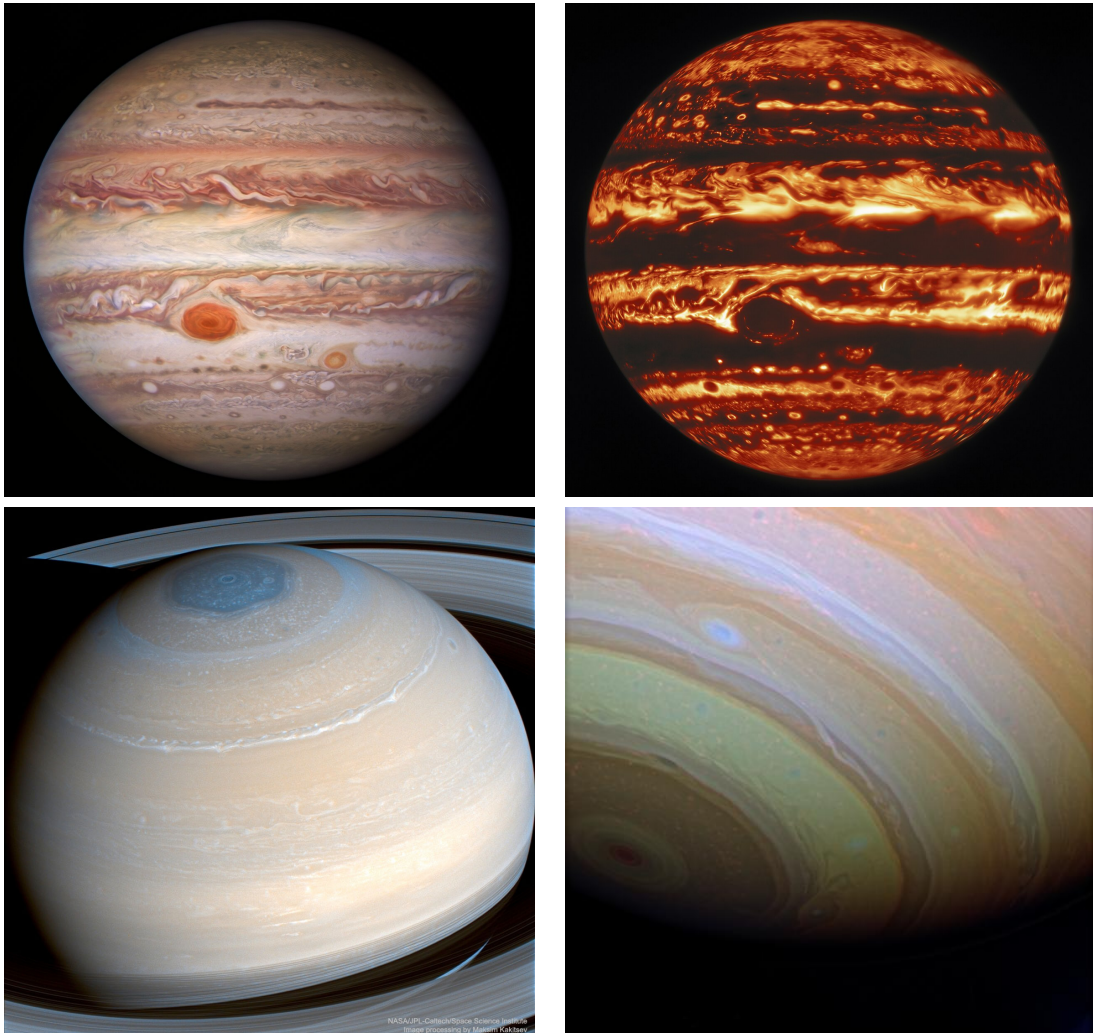


**Figure 1.1.** Top panels show Jupiter in visible wavelengths (left) and infrared (right). The former was made by the Hubble Space Telescope, the latter from the Near-Infrared Imager (NIRI) instrument at the Gemini observatory, both composed of multiple images captured in 2017. Image credit: Credit: NASA, ESA, NOIRLab, NSF, AURA, M. H. Wong and I. de Pater et al. Bottom panels show Saturn (left: 2014, right: 2007). Both are composite infrared images where colour enhancement has been used to make structures visible to the eye. Image Credit: NASA, JPL-Caltech, Space Science Institute, Maksim Kakitsev.

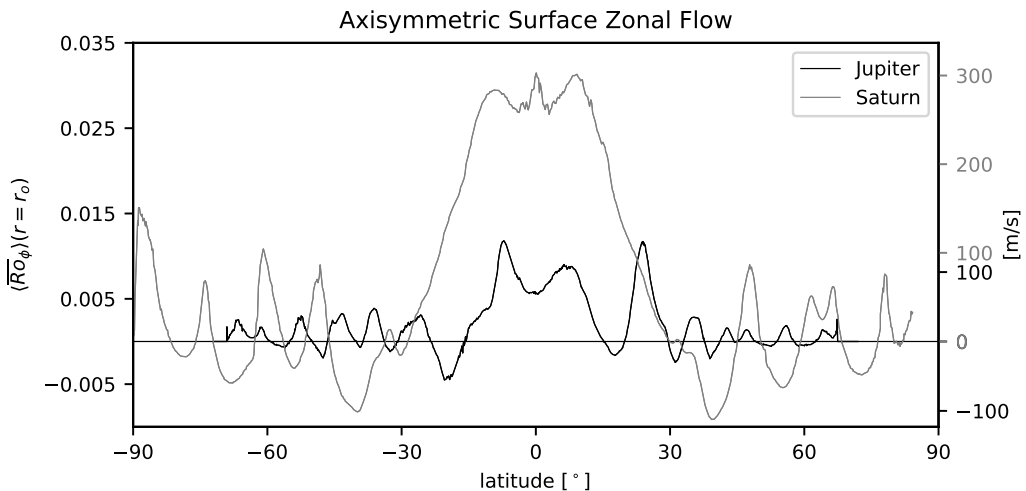


**Figure 1.2.** Axisymmetric surface zonal flow given in m/s (right axis). The grey curve is Saturn’s surface profile from García-Melendo et al. (2011) (‘CB’ filter) adjusted with the rotation period from Mankovich et al. (2019). The black curve shows Jupiter’s surface zonal winds (from Tollefson et al. (2017), measured in December 2016, roughly Juno’s 3rd perijove). They are both plotted as a function of planeto-graphic latitude and the volumetric mean radius was used to convert to Rossby number  $\overline{Ro}_\phi$  (left axis) to facilitate relative comparison.

the belts and zones have a very striking visual manifestation due to ammonia and water phase changes (Fletcher et al. 2020). Upwellings dominate in the zones, which are colder and host ammonia ice, giving them a lighter colouring than the belts, though these phase changes are still not well understood. Due to the different composition of Saturn’s atmosphere, its zonal banding is less eye-catching (see Fig. 1.1). The velocities of the zonal flows in both planets have been measured by cloud-tracking, limiting the only direct zonal flow data to this thin outer layer. As these measurements are not restricted to being performed in *in-situ*, there are several available data-sets made over different time-periods by Voyager I and II, Hubble Space Telescope (HST), Cassini (see Table 1 in Tollefson et al. (2017) and Table 4.5 in Sánchez-Lavega et al. (2019)). Fig. 1.2 shows that both profiles are dominated by strong equatorial prograde flows, measuring around 100 m/s for Jupiter and even 300 m/s for Saturn, using this rotation rate. Saturn’s profile and Jupiter’s southern latitudes then have a similar structure as a retrograde jet flanks the equatorial one and is then followed by multiple alternating jets at the higher latitudes. These are typically narrower for Jupiter than for Saturn. Jupiter’s northern hemisphere has a prominent prograde jet at around 25°N, just as strong as its equatorial jet, giving the zonal flow structure a significant degree of equatorial antisymmetry.

The left axis of Fig. 1.2 gives the zonal flow amplitude in terms of a Rossby number  $\overline{u}_\phi/(\Omega R)$ , where  $\overline{u}_\phi$  is the azimuthal flow, averaged over longitude,  $\Omega$  is the rotation rate and  $R$  is the planetary radius. This allows a more direct comparison between the two planets as it effectively describes the flow amplitude relative to the rotational velocity at the surface. The differences between the two profiles are striking, considering they are both fast rotators and have similar radii. Fundamentally, these are due to Jupiter having

a much larger mass, leading to considerable differences in their interior structures. These affect the outer convective region where the winds are located.

## 1.2 Gas Giant Interiors

Even before data from the Juno and Cassini missions became available it was evident that both Jupiter and Saturn depart strongly from the classical picture of a homogeneous ball of hydrogen and helium with a dense core at the centre. Fig. 1.3 shows a very simplified schematic of our current understanding of the interiors of both planets. In this section we discuss the features marked on this figure by giving a broad summary of recent reviews: Guillot and Gautier (2015), Militzer et al. (2016), Helled and Guillot (2018), Helled (2019).

The physical constraints, from measurements, that must be satisfied when constructing interior models include their radii, masses (see Table 1.1), gravitational fields, temperatures at 1-bar pressure and elemental abundances in their atmospheres.

	Jupiter	Saturn
Distance to Sun (AU)	5.204	9.582
Mass ( $10^{24}$ kg)	$1898.13 \pm 0.19$	$568.319 \pm 0.057$
Equatorial Radius (km)	$71492 \pm 4$	$60268 \pm 4$
Mean Radius (km)	$69911 \pm 6$	$58232 \pm 6$
Mean Density ( $\text{g}/\text{cm}^3$ )	$1.3262 \pm 0.0004$	$0.6871 \pm 0.0002$
Rotation Period	9h 55m 29.56s	10h 39m $\pm \sim 10\text{m}$

**Table 1.1.** Properties of Jupiter and Saturn. Taken from <https://nssdc.gsfc.nasa.gov/planetary/factsheet/jupiterfact.html>

The key characteristics we are interested in constraining are:

- **The depth of the zonal winds.** Prior to the Juno and Cassini era there was no direct evidence for the winds being deep-seated, i.e. several thousand kilometres deep, rather than shallow surface features, associated with a thin weather layer.
- **The nature of the gas giants' cores.** Evidence is gathering that we must update our classical view of a central dense core, surrounded by hydrogen and helium. Rather, both planets may host a gradual transition in their centres, of increasing helium and heavy elements. Should such a dilute core be stable to convection, this would limit the dynamo region for both planets.
- **The depth and thickness of a helium rain layer.** Helium rain refers to a regime, found at certain temperatures and pressures, where hydrogen and helium demix. In such a region helium is thought to form droplets which rain downwards, leaving the layer above helium-poor and that below helium-rich. While the uncertainty of such specific conditions being reached in Jupiter is higher, it is supported by the measured helium- and neon-depletion in the Jovian atmosphere, as neon is thought to ‘piggy-back’ on the helium droplets. The existence of a region of hydrogen-helium

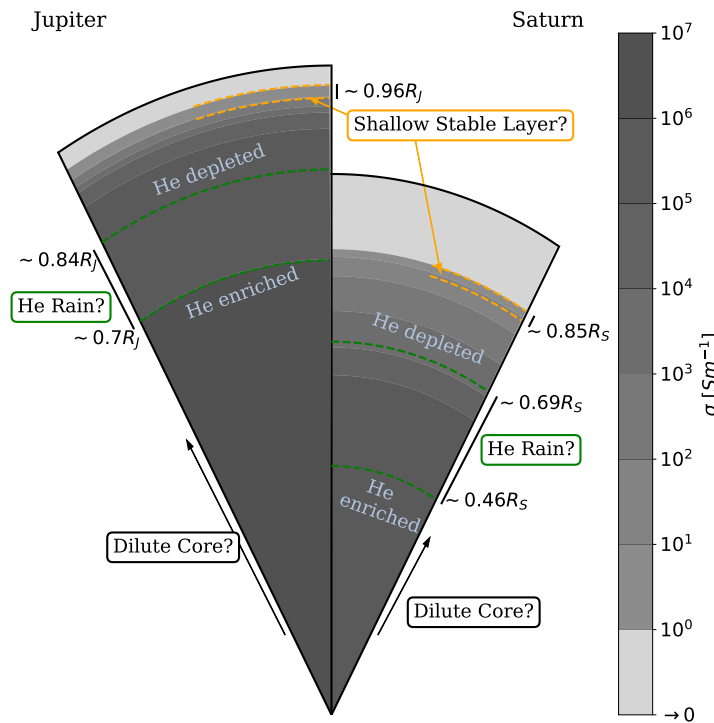


**Figure 1.3.** Schematic of the interiors of Jupiter (left) and Saturn (right), primarily based on similar ones found in Helled (2019), Guillot et al. (2022), Militzer and Hubbard (2023). Grey shading indicates electrical conductivity, based on the profiles from French et al. (2012) and Liu et al. (2008) respectively. For both planets the existence of a dilute core is indicated as well as a roughly mid-depth helium rain layer (green dashed lines), where the depths are taken from Militzer and Hubbard (2023), though for both different depths can be found in the literature. Contrary to most previous works, a shallow stable layer (orange dashed lines) is also indicated here, located in the transition to the semi-conducting region.

immiscibility on Saturn was already proposed by Stevenson (1979), as a stably stratified layer above the dynamo region could help to filter the planet's magnetic field, removing small-scale components.

- **Variation of electrical conductivity with depth.** While the outer envelopes of the planets are primarily made up of non-conducting, molecular hydrogen, the extreme pressures reached in their interiors leads to a transition of hydrogen to a metallic fluid by pressure ionisation. In the pressure-temperature regimes found in the gas giants this is a smooth transition. However, due to the steep increase in pressure, it occurs over a relatively small depth, especially in the more massive Jupiter.

The crucial point to note is that all methods discussed in the following subsections rely on each other to provide constraints. Especially now with the wealth of data available from Juno and Cassini, it is a hard task to reconcile the results from these methods to obtain one cohesive interior model for each gas giant.

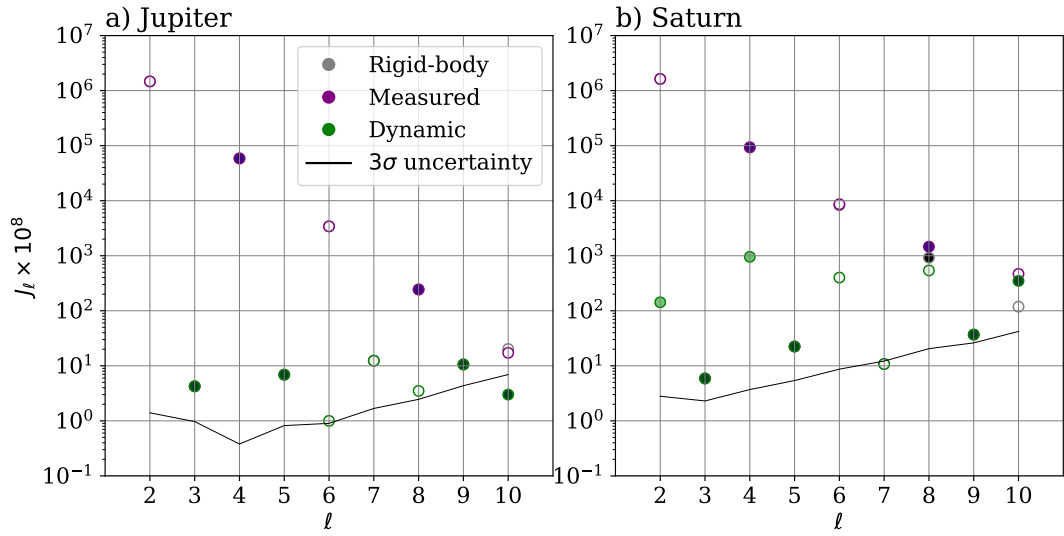


**Figure 1.4.** The first ten gravity moments of **a)** Jupiter and **b)** Saturn, taken from Kaspi et al. (2020) and Galanti and Kaspi (2020), respectively. Positive (negative) values are unfilled (filled). The direct Juno and Cassini measurements (purple), are also split into the calculated rigid-body contributions (grey) and dynamic contributions,  $\Delta J_\ell$  (green). The uncertainty associated with the measured gravity moments is indicated by the black line.

### 1.2.1 Gravimetry

The crucial addition to data in Table 1.1 used to constrain the internal mass distribution of the gas giants are the gravity moments, measured *in-situ* by Juno (Iess et al. 2018, Durante et al. 2020) and Cassini (Iess et al. 2019) and shown in Fig. 1.4. These measurements required tracking the accelerations of the space-craft relative to the respective planet, as well as a third mass, in this case Earth. This is done by transmitting signals from Earth at two different frequencies which are then retransmitted from the spacecraft. The difference in the transmitted and received frequencies then gives the Doppler measurement.

Gravity moments are expansion coefficients used when expressing the planet's gravitational potential in spherical harmonics. In this case, the expansion is only in terms of degree  $\ell$ , not order  $m$ , as any azimuthal variations are minuscule<sup>1</sup>. They are defined as:

$$J_\ell = -\frac{2\pi}{MR^\ell} \int_0^R \int_0^\pi \rho(r, \theta) r^{\ell+2} \sin \theta P_\ell(\cos \theta) d\theta dr, \quad (1.1)$$

where  $\rho$  is the axisymmetric part of the density at radius  $r$  and co-latitude  $\theta$ ,  $M$  is the planetary mass,  $P_\ell$  are the Legendre polynomials, and  $R$  is the planetary radius. From this expression we see that the lower degree moments are more sensitive to the deeper interior than higher degree coefficients which mainly probe the outer envelope, due to the  $r^\ell$  dependence.

In Fig. 1.4 these measured  $J_\ell$  are shown by the purple symbols. The dynamic contribution  $\Delta J_\ell$  (green) is due to the zonal winds. The rigid-body contribution, (grey) is required

<sup>1</sup>Note that in most literature the gravity moments are referred to as  $J_n$ . In this work  $J_\ell$  is used in order to be consistent with other references to the degree,  $\ell$  in the text.

to make inferences with respect to the planet's deep interior. Note that only the even  $J_\ell$  make such a contribution as any interior stratification can be assumed to be equatorially symmetric. This is because the main cause for the gas planets' departure from perfect sphericity is due to the fast rotation, causing them to be oblate - sometimes referred to as an equatorial bulge.

### Gravity Moments: Dynamic Contribution

The odd gravity moments are direct evidence of a non-equatorially symmetric redistribution of mass inside the planets. These form the main parts of the dynamic contribution  $\Delta J_\ell$  and are due to the mass flux introduced by the zonal winds. While the rigid-body contributions dominate the even gravity moments, they also have a non-negligible dynamic component, especially for Saturn, as the winds also have a significant degree of equatorial symmetry. The  $\Delta J_\ell$  can be used to infer the depth of the zonal winds in the two planets. For Jupiter, the surface zonal wind profile has a higher degree of equatorial antisymmetry and thus the odd moments suffice to carry out this analysis. For Saturn the dynamic part of the even moments is also required, adding a significant additional uncertainty as these contain not only the instrumental errors but also errors associated with the evaluation of the rigid-body contribution which are subtracted from the measured  $J_\ell$ .

Although density is much greater in Jupiter, Saturn's winds are both stronger and deeper-reaching, so have a greater mass flux associated with them: in Jupiter the winds involve only  $\sim 1\%$  of the planet's mass compared to  $\sim 7\%$  on Saturn. Thus, in general the  $\Delta J_\ell$  are larger for Saturn. Further analysis then relies on the following assumptions:

- The measured cloud-level winds are representative of those at depth. This excludes the possibility of significant flow variation in the outer weather layer.
- The zonal wind structures are invariant with respect to the rotation axis, i.e. are geostrophic (see Section 1.4.4). Therefore, the surface profiles can be extrapolated downwards in each hemisphere. This yields a two-dimensional zonal flow structure which is only a function of  $s$ , the distance from the axis of rotation.
- The quenching of the zonal winds is purely depth dependent. Thus, a radially dependent damping function, applied to the  $\bar{u}_\phi(s)$  profile should represent each planet's zonal flow in 2D.

Based on theory and simulations as well as some direct comparisons with alternative approaches (e.g. a non-geostrophic continuation of the jets) by Galanti et al. (2021), these assumptions seem reasonable, within the uncertainties of the measurements.

The next step in the analysis involves linking these dynamics to the gravity perturbations they would cause, thereby obtaining values for  $\Delta J_\ell$  which are dependent on the radial decay profile used, where both onset-depth and rate of decay are varied. These are then matched as closely as possible to the measured values.

This method was already suggested before Juno reached Jupiter (Kaspi et al. 2009, Kaspi 2013). However, its exact execution was a topic of hot debate for a whole decade. The link between the 2D flow structure and the gravitational potential is made using the so-called Thermal-(Gravitational)-Wind Equation (TWE; TGWE). A brief summary of the

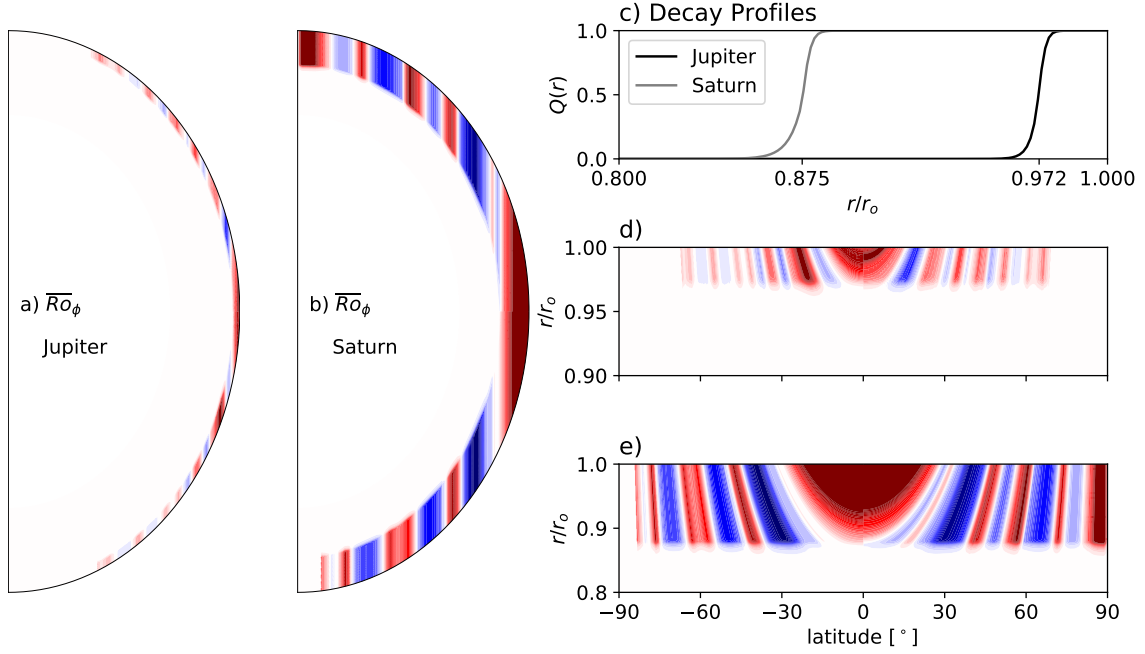


**Figure 1.5.** Measured surface zonal wind profiles shown in Fig. 1.2 extrapolated downwards, invariant to  $z$  in each hemisphere for a), d) Jupiter, and b), e) Saturn. c) the radially dependent damping functions from Galanti and Kaspi (2020) are applied. The four 2D plots, given in zonal Rossby numbers, have the same colour-scale of  $\pm 0.01$ , where prograde (retrograde) flow is red (blue).

this method is outlined below.

We first separate density  $\rho$ , gravity  $g$ , and pressure  $p$  into a background profile (denoted by tilde and dependent only on radius) and a perturbation (denoted by subscript  $c$  and dependent on radius and colatitude  $\theta$ ). The static first order expansion of the Navier-Stokes equation is then:

$$2\Omega \times (\tilde{\rho}\mathbf{u}) = -\nabla p_c + \underbrace{\rho_c \nabla \tilde{\Psi}}_{(a)} + \underbrace{\tilde{\rho} \nabla \Psi_c}_{(b)}. \quad (1.2)$$

Here, the Coriolis force is on the left hand side, where  $\Omega$  is the planetary rotation vector and  $\mathbf{u}$  is the velocity vector. The last terms on the right hand side are the gravity force, separated into a) the product of the density perturbation caused by the winds  $\rho_c$  and the gradient of the effective background potential  $\nabla \tilde{\Psi}$ , and b) the product of the background density  $\tilde{\rho}$  and the gravity perturbation due to the winds  $\nabla \Psi_c$ . The T(G)WE is obtained by taking the curl of Eq. 1.2 and from this the density anomaly is found, which is required to calculate the  $\Delta J_\ell$ .

Justifying which approximations are valid when solving this equation caused much dispute. Firstly, the non-sphericity of the planet is neglected (Cao and Stevenson 2017). Secondly, term (b) in Eq. 1.2, is neglected in the TWE (used in Kaspi et al. (2016), Galanti et al. (2017), Kaspi et al. (2018), Iess et al. (2019)) while the TGWE deems it important (Zhang et al. 2015, Kong et al. 2016, 2018). In Wicht et al. (2020), we explored the impact of  $\Psi_c$ , calling it the Dynamic Self Gravity (DSG), applying it to the Juno measurements

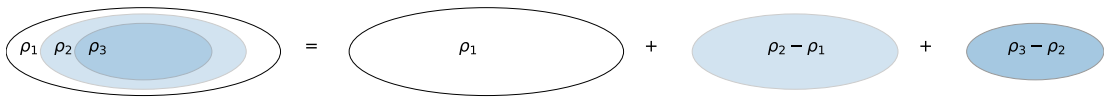


**Figure 1.6.** Schematic illustrating the Concentric Maclaurin Spheroid method based on figures from Hubbard (2013). The oblateness of the spheroids is extremely exaggerated. Each spheroid has a different density with  $\rho_1 < \rho_2 < \rho_3$ .

in Dietrich et al. (2021).

Our results remained broadly consistent with the inferred depths of 2,500 – 3,000 km found by Kaspi et al. (2018), also using the measurements  $J_3$ ,  $J_5$ ,  $J_7$  and  $J_9$ . Some further analysis has been carried out since these first works, using the higher degree of accuracy achieved with the additional fly-by's and adding constraints from the magnetic field; i.e. restrictions based on how much the winds interact with the conducting region (Cao and Stevenson 2017, Wicht et al. 2019, Moore et al. 2019). These yielded a slightly shallower estimate of a depth of  $\sim 2,000$  km, with a decay of the surface zonal wind amplitudes to almost zero over only around 2% planetary radius (Galanti and Kaspi 2020).

For Saturn some even gravity moments were also required (analysis is based on  $J_3$  and  $J_5 - J_{10}$ ) as constraints and to find a satisfactory agreement with the measurements the surface profile was also tweaked slightly. As with Jupiter, adding magnetic field constraints reduced the penetration depth slightly from around 8,000 km in Galanti et al. (2019) to  $\sim 7,000$  km in Galanti and Kaspi (2020), and sharpened the decay.

The two 2D flow structures are shown in Fig. 1.5, where the surface profiles from Fig. 1.2 have been extrapolated downwards and the decay functions from Galanti and Kaspi (2020) have been applied.

### Gravity Moments: Rigid-body Contribution

Two main methods are used to yield information about the homogeneity of the planetary interior from the gravity moments. Both methods rely on the reasonable assumption that equipotential surfaces exist in the planet, where pressure and density are constant. These are Theory of Figures (ToF) (Zharkov and Trubitsyn 1978) and ‘Concentric Maclaurin Spheroids’ (CMS), developed by Hubbard (2012, 2013). This method is based on superimposing a series of ellipsoids, each incompressible and of a different density, to reproduce the prescribed barotrope, as shown in Fig. 1.6. These must fit the even gravity moments as well as the planetary radius, rotation rate and the chemical composition of the atmosphere.

Militzer and Hubbard (2023) give a good overview when comparing their own results with the other most recent models made using these methods in their Table 3; for Jupiter see Militzer et al. (2022), Miguel, Y. et al. (2022), Nettelmann et al. (2021), for Saturn see Militzer et al. (2019), Nettelmann et al. (2021), Mankovich and Fuller (2021). We recommend these works for details on the methods and only describe the results here.

Broadly, for Jupiter the models strongly suggest a dilute core, reaching around  $0.4 - 0.6R_J$  over which the transition to the metallic hydrogen region takes place (Wahl et al. 2017).

This is bounded by a helium rain layer at  $\sim 70\%$ , reaching  $\sim 84\%$  planetary radius. Above this the electrical conductivity decreases by many orders of magnitude and zonal winds dominate in the outer, convecting, molecular hydrogen envelope. In Saturn it is less certain whether there is a compact core or a dilute one, as in Jupiter. As the planet is much less dense, the pressures at which helium rain occurs (around 80 – 100 GPa) are reached deeper in the planet’s interior,  $\sim 0.46 – 0.69R_J$  in Militzer and Hubbard (2023). This makes the outer molecular hydrogen layer much deeper.

Fig. 1.3 illustrates these two structures.

### 1.2.2 Kronoseismology

The detection of normal modes in Saturn using ring seismology marked a tremendous advance in constraining the planet’s interior structure, in particular the possible location of stably stratified layers. The measurements are made by observing density waves in the Kronian rings, which are interpreted to be caused by normal-mode oscillations inside the planet as they do not coincide with any possible resonances with the moons (Hedman and Nicholson 2013). These normal modes can be manifestations of internal gravity waves which occur in stably stratified layers, due to an oscillatory radial motion caused by the inverse buoyancy force (see Section 1.4.5 for a discussion of these).

A new bulk rotation period of  $10^h33^m38s^{+1m52s}_{-1m19s}$  has been inferred using these measurements (Mankovich et al. 2019), faster than that obtained from kilometric radiation period measurements which is how previous estimates were calculated. The character of the gravity modes strongly suggests that up to half of the inner planet is stable against convection (Mankovich 2020, Dewberry et al. 2021).

The key task is still to build comprehensive interior models based on both gravitational and seismological constraints. See Fortney et al. (2023) for an overview of Saturn’s interior at this point in the Cassini era.

### 1.2.3 *Ab-Initio* Models

To build internal structure models, equations of state (EOS) - relevant to the pressures of up to  $\sim 70$  TPa reached in Jupiter - are a necessity. Despite hydrogen being the simplest molecule, the Equation of State (EOS) is not simple. At small pressures and temperatures, it behaves like an ideal gas while at higher pressures it deviates strongly. This is complicated even further when helium and heavy elements are added. *Ab-initio* models rely on first principles to carry out large-scale quantum molecular dynamics simulations, within the framework of finite-temperature density functional theory (Dreizler and Gross 1990). These are extremely difficult to carry out and computationally expensive. Furthermore, different models can lead to differences in density and temperature approximations on the order of 10%.

In Fig. 1.7 the results of French et al. (2012) are shown, which are based on calculations made along a Jupiter adiabat from a model by Nettelmann et al. (2012). The model from Nettelmann et al. (2012) is a two-layer model and provides constraints such as core-mass, gravity moments and the pressure at which the transition between the two outer layers takes place. The advantage of the profiles from French et al. (2012) the whole data-set is derived using the same method for both the equation of state and the transport properties.

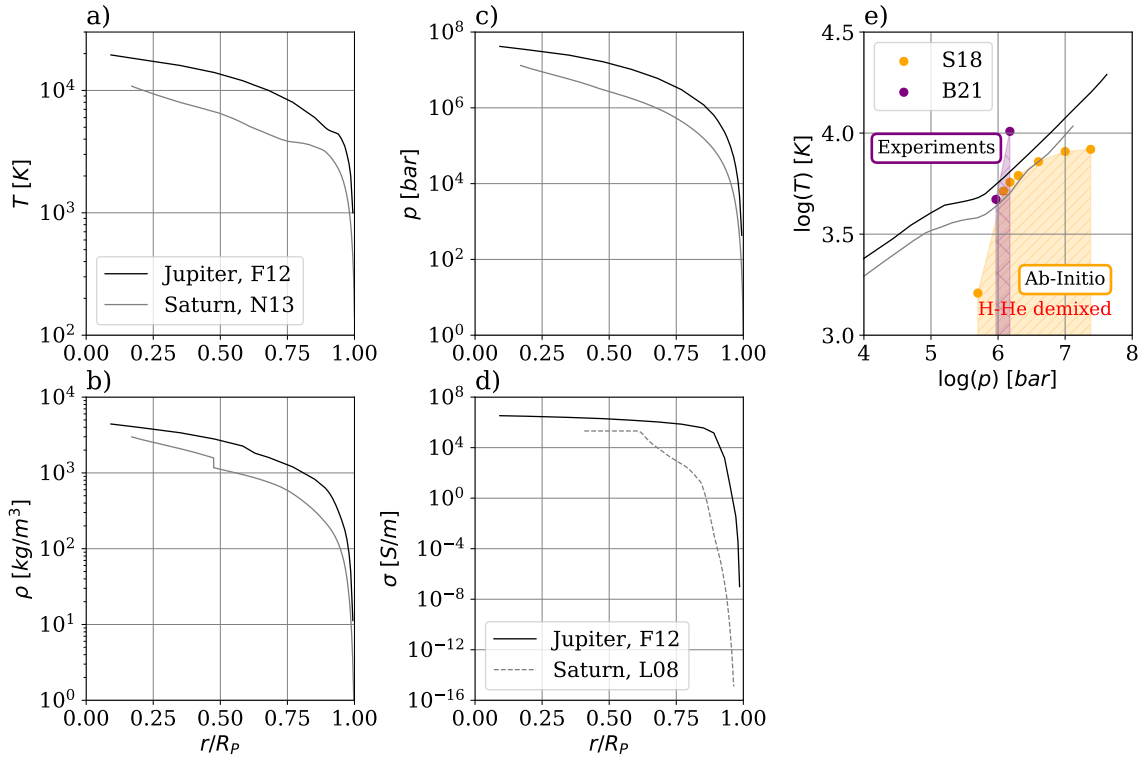


**Figure 1.7.** Interior profiles of Jupiter (black) and Saturn (grey). **a)** temperature, **b)** density and **c)** pressure as a function of radius, from French et al. (2012), F12, and Nettelmann et al. (2013), N13. **d)** electrical conductivity as a function of radius, with the Saturn profile taken from Liu et al. (2008). **e)** temperature as a function of pressure, with the hydrogen-helium immiscibility region indicated, as inferred from *ab-initio* models (orange, Schöttler and Redmer (2018) interpolated to 11 mol% He fraction) and experiments (purple, Brygoo et al. (2021)). This is a simplified version of Fig. 2 in Guillot et al. (2022).

Not only does it include the electrical conductivity shown in Fig. 1.7d, for the density, temperature and pressure profiles shown in Fig. 1.7a-c, but also thermal conductivity, heat capacities, and the Grüneisen parameter, among other parameters.

Unfortunately, for Saturn such a consistently derived data set does not exist, yet, so we show the adiabats from Nettelmann et al. (2013) and the electrical conductivity profile from Liu et al. (2008).

With respect to the formation of a helium rain layer, the critical question is whether helium's phase separation from metallic hydrogen takes place within the gas giant adiabats - see the p-T adiabats plotted in Fig. 1.7e. While Saturn's adiabat is within the *ab-initio* model results from Schöttler and Redmer (2018), Jupiter's lies above the predicted immiscibility regime. This would leave the question of why Jupiter's atmosphere is depleted in helium unanswered.

### 1.2.4 Experiments

The pressures and temperatures reached in gas giant interiors are extremely difficult to achieve in laboratory experiments. They are carried out using hydrogen-helium samples which have been compressed using diamond-anvil cells. They are then exposed to laser-driven shock compression. We do not go into further detail, but have included the two data points from Brygoo et al. (2021) in Fig. 1.7e. These are the first experimental evidence that hydrogen-helium demixing should occur in Jupiter, too.

### 1.2.5 Magnetic Fields

While both gas giants have dipole-dominated magnetic fields - see Fig. 1.8a, b and e, f - there are many significant differences between them. Not only are the amplitudes two order of magnitude apart (see colourbars on Fig. 1.8a and b), but their structures also differ dramatically.

#### Jupiter

Jupiter showcases a hemispheric dichotomy in its magnetic field, albeit still dipole-dominated (see Fig. 1.8e), with its northern hemisphere being the more irregular (Moore et al. 2018, Connerney et al. 2022). This is seen in the radial magnetic field  $B_r$  shown in Figures 1.8a and c. While its southern hemisphere is very dipolar, there are two intense flux patches in its northern hemisphere: a large mid-latitudinal patch of positive  $B_r$ , as well as the so-called "Great Blue Spot", a very localised patch of negative  $B_r$  near the equator.

Magnetic field observations have now also been used to make inferences about the zonal wind penetration depth, made possible by the high number of orbits of Juno and comparison with older missions, allowing the measurement of the time dependence of the field (secular variation), see Moore et al. (2019), Bloxham et al. (2022). Depending on the extent of the zonal winds' interaction with Jupiter's semi-conducting region, they may be the cause of a zonal drift of the field. From Fig. 1.5 it is clear that if the winds were to reach the semi-conducting region (around  $0.9 R_J$ ), the most significant contribution near the equator would be from the prominent prograde jet (at  $\sim 25^\circ\text{N}$  at the surface). However, the differential rotation inferred from the secular variation analysis by Bloxham et al. (2022) is extremely equatorially symmetric in this region - and also much slower - suggesting that these are deeper flows, separate from those observed on the surface. Bloxham et al. (2022) point out that these are much more similar to the flows observed in numerical simulations which tend to have a high degree of equatorial symmetry.

#### Saturn

The results from Cassini, in particular from its closest approaches at the Grand Finale, have allowed an accurate characterisation of Saturn's magnetic field (Dougherty et al. 2018, Cao et al. 2020), completing the picture from Pioneer 11 (Smith et al. 1980), Voyager I (Ness et al. 1981) and Voyager II (Ness et al. 1982). These most recent measurements have only confirmed the extraordinary degree of axisymmetry of the field, as seen in Fig. 1.8b. The dipole tilt was found to be less than  $0.007^\circ$  (Cao et al. 2020). The

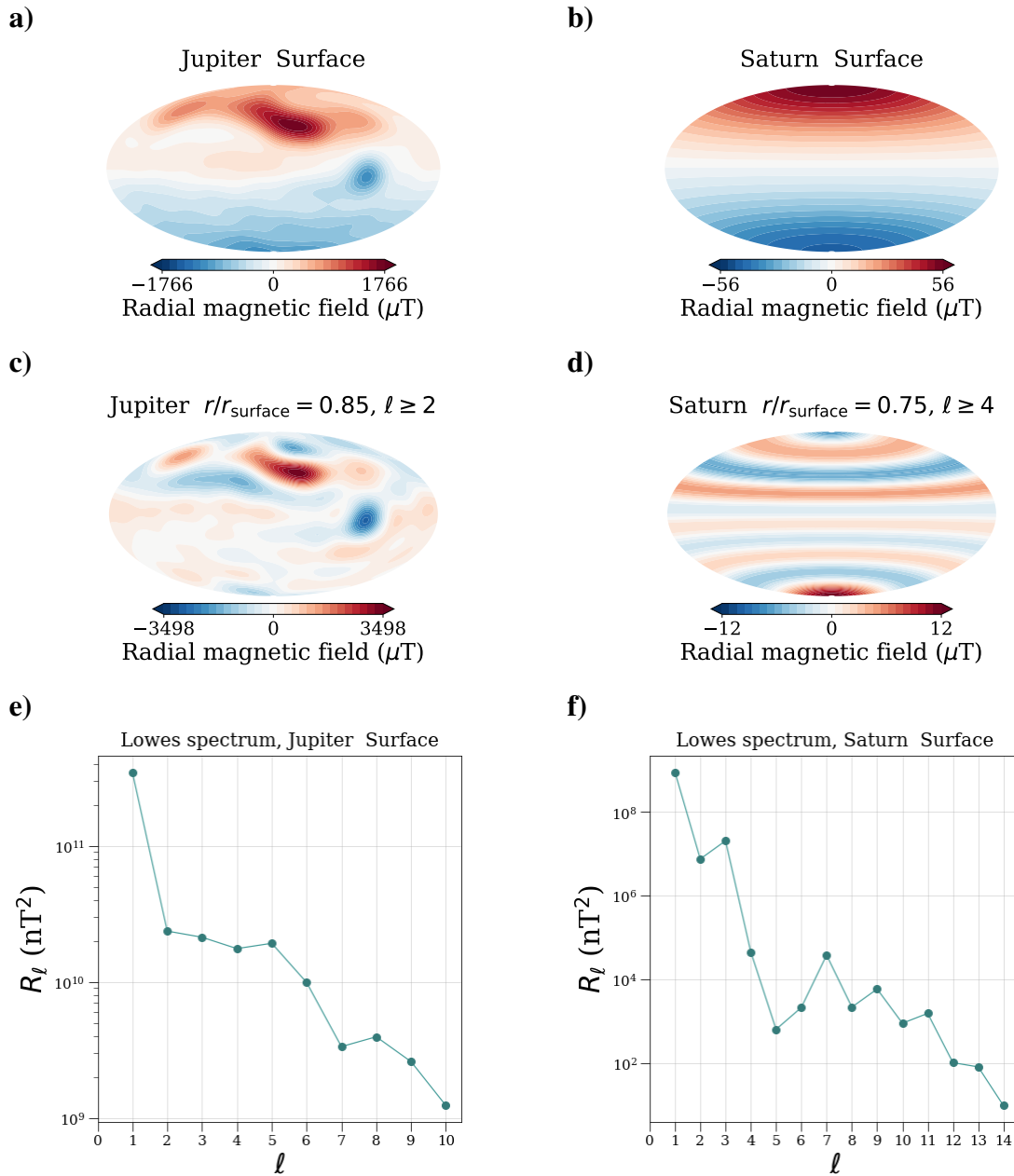


**Figure 1.8.** Surface magnetic fields of **a)** Jupiter and **b)** Saturn, given in  $\mu T$ . In **c** and **d** these two radial fields are shown on the dynamo surface  $r_d$ , around  $0.85 R_J$  and  $0.75 R_S$  respectively, for only the smaller scales;  $\ell \geq 2$  and  $\ell \geq 4$ . Lowes spectrum at the surface for **e)** Jupiter and **f)** Saturn. Jupiter data is from Connerney et al. (2018), Saturn data is from Cao et al. (2020). Plots were made using the open-source code from Ankit Barik: <https://github.com/AnkitBarik/planetMagFields>.

axisymmetry is also observed in the higher degree moments (Fig. 1.8d), where a prominent latitudinal banding is seen. These  $\sim 15^\circ$  wide bands correspond to the widths of the zonal jets on the dynamo surface; see the lower extent of the winds shown in Fig. 1.5e. This strong correlation points to the higher order ( $\ell \geq 4$ ) moments originating from a fairly shallow secondary dynamo region where the zonal winds interact with the semi-conducting layer. The winds may induce such a field perturbation if there is a low-order background field from below. This primary dynamo region is most likely located between a dilute core and a helium rain layer (see Fig. 1.3) where, therefore, magnetoconvection must be possible. This would preclude a direct transition from a stable dilute core to a helium rain layer. The theory of a secondary dynamo is supported by the two orders of magnitude difference in the first three magnetic moments compared to the higher degrees (see Fig. 1.8f), which corresponds to around one order of magnitude difference between  $B_r$  (total radial field) and  $\Delta B_r$  ( $\ell \geq 4$  radial field) at  $r_d = 0.75 R_S$ .

### 1.3 Surface Processes

While strong zonal flows dominate the dynamics at the surfaces of the two gas planets, more detailed measurements of the weaker and smaller-scale flows have also been possible. In this section we discuss the small-scale eddies, vortices and meridional flow.

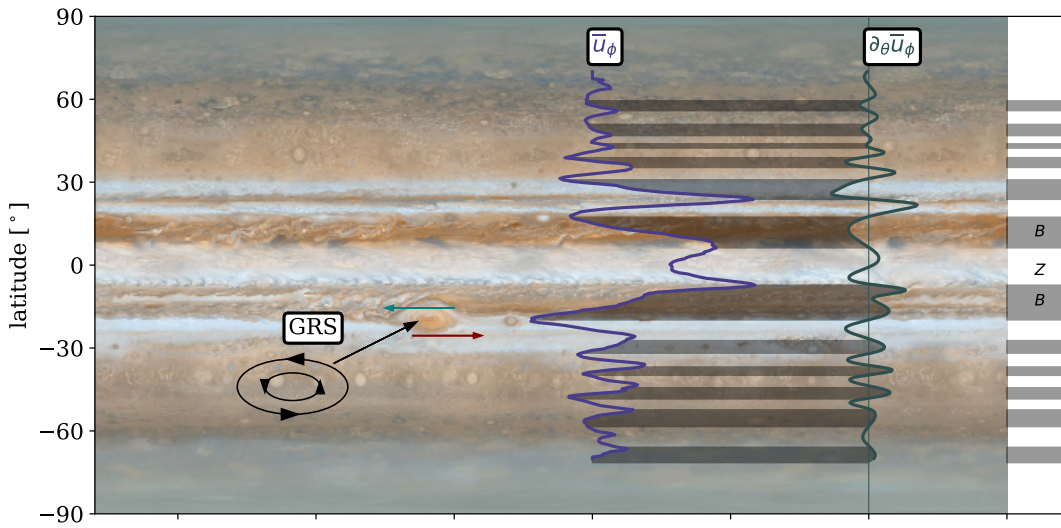


**Figure 1.9.** Image of Jupiter's surface (NASA image PIA07782, NASA/JPL/Space Science Institute). The surface zonal wind velocity is plotted in purple and the shear  $\partial_\theta \bar{u}_\phi$  in dark grey. Belts are shaded, corresponding to regions of negative vorticity and primarily host anticlockwise (clockwise) vortices in the northern (southern) hemisphere. The zones are left unshaded and the cyclonic Great Red Spot (GRS) is marked in its zone in the southern hemisphere.

### 1.3.1 Eddies

The zonal winds on the gas giants are not considered to be driven by a direct acceleration of the zonal velocity. Rather, they are driven by small-scale eddies. In this context, eddies describe a remainder left after the longitudinal mean has been subtracted from a flow. We denote this by a prime, while the longitudinal average is denoted by an overbar, e.g. for azimuthal flow  $u_\phi = \bar{u}_\phi + u'_\phi$ , and similarly in the other directions in a spherical coordinate system.

In order to transport angular momentum and form zonal winds, Reynolds stresses are crucial. They are defined as  $\rho \overline{\mathbf{u}'_m u'_\phi}$ , where  $\mathbf{u}'_m$  is non-axisymmetric flow in the meridional plane, i.e. the co-latitudinal and radial directions;  $\theta$  and  $r$ . On the surface, where direct measurements have been made, these reduce to  $\rho u'_\theta u'_\phi$ , where  $\rho u'_\theta$  is a southward eddy flux and  $u'_\phi$  is an eastward eddy velocity. Note that these correlations of the small-scale flows must be considered in a statistical sense, i.e. averaged over a long time period.

In the region between a retrograde (westward) jet in the northern hemisphere and a prograde jet that is closer to the equator (a so-called ‘belt’, marked by a shaded region in Fig. 1.9), there is positive Reynolds stress as momentum is entering the prograde jet and leaving the retrograde one. Thus, the direct correlation is between the Reynolds stresses and the shear; the co-latitudinal derivative of  $\bar{u}_\phi$ .

For Jupiter, the strong correlation between Reynolds stresses and zonal flows has been observed since the first Voyager 1 and 2 images (Beebe et al. 1980, Ingersoll et al. 1981), providing evidence for the conversion of energy from these smaller scales to the large-scale zonal flow. The Cassini fly-by in 2000 allowed Salyk et al. (2006) to carry out a similar analysis with an even greater number of velocity vectors.

A similar study was carried out for Saturn by Del Genio and Barbara (2012), also suggesting that the alternating divergent and convergent Reynolds stresses were transporting momentum inwards or outwards and forming the zonal jets. This analysis was extended to the poles by (Read et al. 2022), confirming that eddies were also transferring energy to the high-latitude jets, although the dynamics are slightly more complex near its north polar vortex (see the following section).

### 1.3.2 Vortices

After the bright zones and dark belts, the eye is drawn to the ovals that feature on the Jovian surface, white and red in colour, such as the Great Red Spot (GRS). This is both the most famous and the largest vortex, with a diameter similar to the width of the zonal jets (see Fig. 1.9), while smaller ones on the scale of a couple of hundred kilometres have also been identified using cloud-tracking. In the mid-latitudes 90% of these vortices are anticyclonic, rotating clockwise in the northern hemisphere or anticlockwise in the southern hemisphere, like the GRS. Belts, with their cyclonic vorticity, host the cyclonic vortices and visa-versa, from which we infer that the shear from the zonal winds makes vortices rotating the opposite way weaker and short-lived. This is illustrated by the blue (westward) and red (eastward) arrows marking flow direction northwards and southwards of the GRS in Fig. 1.9. This makes it stable and allows it to be long-living. A cyclonic vortex in this shear region would be unstable as it would be rotating against the direction of the zonal wind bounding it.

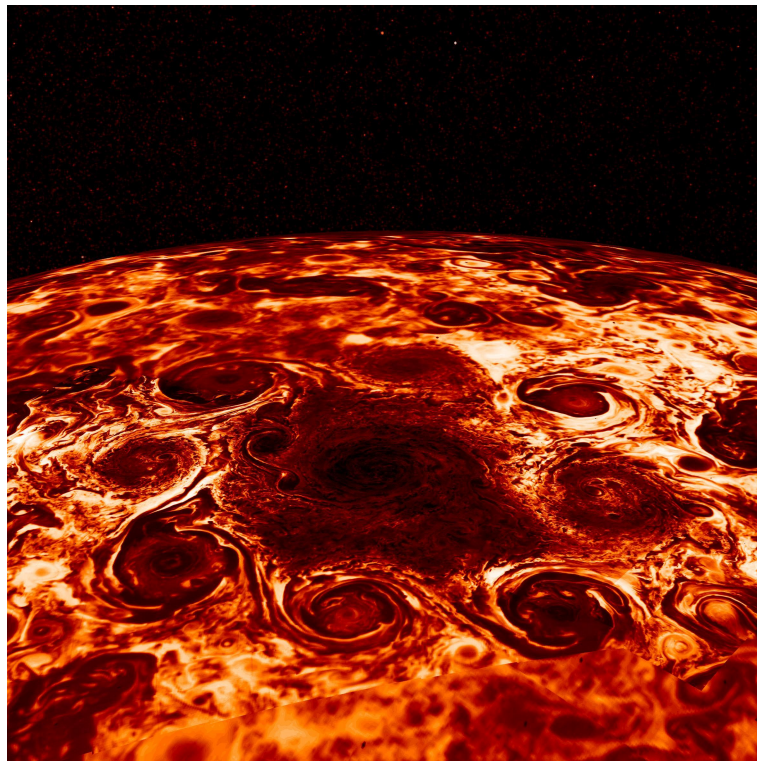


**Figure 1.10.** Jupiter’s North pole in the infrared taken by JIRAM (Jovian Infrared Auroral Mapper) from 2017. Dark red is low radiance while white is high. The 8 circumpolar cyclones (CPC’s) at the north pole are clearly visible. Image credit: NASA/JPL-Caltech/SwRI/ASI/INAF/JIRAM.

It is known that the largest of these vortices can survive for centuries as the GRS was first observed over 150 years ago. For the GRS there are now even estimates of its depth, thanks to the Juno gravity data. Parisi et al. (2021) inferred that it is no more than 500 km deep. This is much shallower than the winds which extend at least 2,000 km into the interior, yet it is clear that this storm is not just a weather layer phenomenon.

Another noticeable type of vortex was observed at Jupiter’s poles (Orton et al. 2017, Adriani et al. 2018). These number eight at the north pole, shown in Fig. 1.10, and five in the south. Both sets of circumpolar cyclones are bounded by a prograde jet and each has a diameter of around 3,000 km. As they are so near to the pole, their axis is essentially parallel to the axis of rotation, unlike the GRS at the midlatitudes.

Similarly, Saturn’s mid-latitudes are dominated by anticyclones, though slightly less extremely, while its circumpolar vortices are cyclonic (Sánchez-Lavega et al. 2006, Baines et al. 2009). Many of its anticyclones are found in its ‘Storm Alley’; the region between the equatorial prograde jet to the flanking retrograde jets, where the shear amplitude is greatest. At the poles, there is no polygonal circumpolar cyclone pattern, rather a single cyclone at the pole (see Fig. 1.11). This is, however, surrounded by the ‘Polar Hexagon’ (Sánchez-Lavega et al. 2014, Antuñano et al. 2015) at the north pole, which is thought to be a trapped Rossby wave.

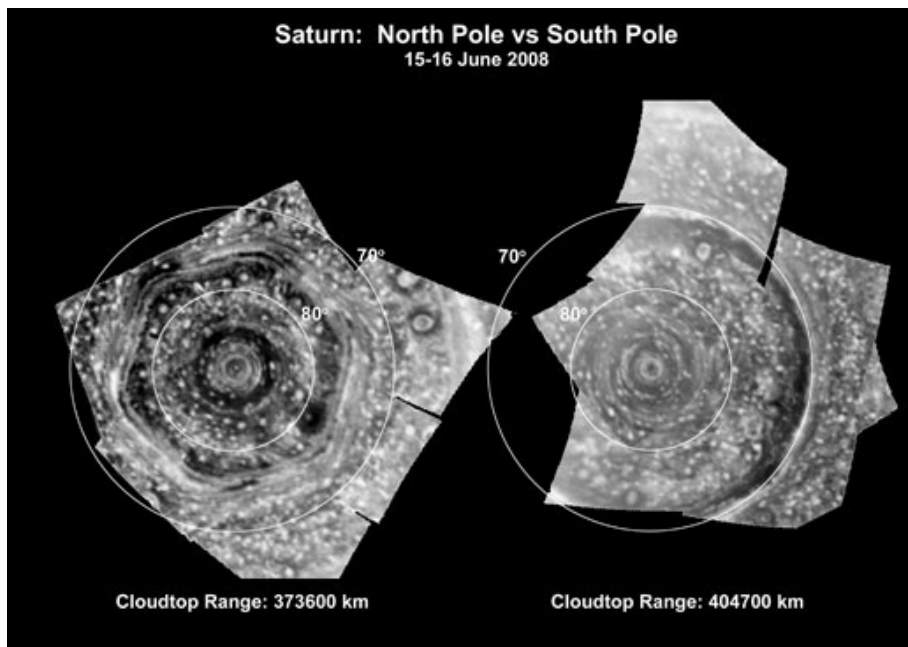


**Figure 1.11.** North pole (left) and south pole (right) of Saturn in infrared, obtained by the visual and infrared mapping spectrometer onboard the Cassini spacecraft, from 2008. The circles indicate  $\pm 70^\circ$  and  $\pm 80^\circ$  latitude. The polar hexagon at the north pole and the polar cyclone in the south are clearly visible. Image credit: NASA/JPL/University of Arizona.

### 1.3.3 Meridional Flow

The dynamics of Earth's zonal flows, driven by eddy momentum flux convergence, and their connection with "Ferrel" cells lead to the question if similar cells may exist on Jupiter. These are meridional circulation cells, i.e. axisymmetric radial,  $\bar{u}_r$ , and latitudinal,  $\bar{u}_\theta$ , flow.

While the only direct measurements of surface flows are those accessible by cloud tracking, data from Juno's Microwave Radiometer (MWR) has enabled further inferences to be made about the dynamics slightly below the 1-bar level. Its six microwave channels each measure the brightness temperature at depths ranging between  $\sim 0.7 - 240$  bar. However, the analysis of the available data is complicated due to interactions with the shallow weather layer (Fletcher et al. 2020, Read et al. 2020) and the behaviour of ammonia when being advected needs to be understood. This is because the brightness temperature measurement essentially yields an ammonia distribution. It is thought that in upwellings ammonia is dragged up from deeper regions, where its concentration is higher, to shallower, less ammonia-rich regions. Duer et al. (2021) found that each jet between  $20^\circ - 60^\circ$  N/S is associated with a circulation cell in the meridional plane. However, it is difficult to say if these are mainly connected to surface processes (Fletcher et al. 2021) or the deeper convective region below.

## 1.4 Theory

In this section we lay out the theory describing motion in a rotating, convective, and electrically conducting fluid. The system consists of a spherical shell with outer radius  $r_o$  and inner radius  $r_i$ , rotating with angular velocity  $\Omega$ . We use both spherical  $(r, \theta, \phi)$  and cylindrical  $(s, z, \phi)$  coordinate systems, where  $s$  is the distance from the axis of rotation,  $e_z$  is parallel to the axis and  $\phi$  is longitude.

### 1.4.1 Governing Equations

In this section we outline the governing equations of the system. These include conservation equations for mass, momentum and energy, Maxwell's equations and an evolution equation for the magnetic field.

#### Conservation of Mass

We begin with the equation for mass conservation:

$$\frac{\partial \rho}{\partial t} = -\nabla \cdot (\rho \mathbf{u}), \quad (1.3)$$

#### Conservation of Momentum

The general equation for momentum conservation for a fluid in a rotating reference frame, the so-called "Navier-Stokes Equation":

$$\rho \frac{D\mathbf{u}}{Dt} + 2\rho \boldsymbol{\Omega} \times \mathbf{u} = -\nabla p + \rho \mathbf{g} + \mathbf{j} \times \mathbf{B} + \rho \mathbf{F}_v, \quad (1.4)$$

where  $D\mathbf{u}/Dt = \partial/\partial t + \mathbf{u} \cdot \nabla$  is the material derivative. Here,  $\mathbf{u}$  is the velocity of the fluid,  $t$  is time,  $\rho$  is the density,  $\mathbf{g}$  the gravity and  $p$  the pressure. The second term on the left hand side represents the Coriolis force. The centrifugal force term,  $\boldsymbol{\Omega} \times (\boldsymbol{\Omega} \times \mathbf{r})$ , is technically absorbed into the gravitational force on the right hand side. This means that, strictly speaking, this term would not be completely radial. However, this is neglected in numerical simulations, therefore the effects of oblateness cannot be modelled. The remaining three terms on the right hand side are the pressure gradient; the Lorentz force,  $\mathbf{j} \times \mathbf{B}$  (where  $\mathbf{j}$  is the current density and  $\mathbf{B}$  is the magnetic field); and the viscous force  $\rho \mathbf{F}_v$ .

The viscous force is written as

$$F_i^v = \frac{1}{\rho} \partial_j \left[ \rho \nu (\partial_j u_i + \partial_i u_j - \frac{2}{3} \delta_{ij} \nabla \cdot \mathbf{u}) \right], \quad (1.5)$$

where  $\nu$  is the kinematic viscosity.

## Conservation of Thermal Energy

The heat transport equation can be written as

$$\rho T \frac{DS}{Dt} = \nabla \cdot (k \nabla T) + Q_{ohm} + Q_v. \quad (1.6)$$

Here  $T$  is the temperature,  $S$  is the entropy and  $k$  is the thermal conductivity.  $Q$  are heat sources:

$$Q_{ohm} = \frac{\lambda}{\mu} (\nabla \times \mathbf{B})^2, \quad (1.7)$$

$$Q_v = \rho v \left( \frac{\partial u_i}{\partial x_j} \frac{\partial u_i}{\partial x_j} + \frac{\partial u_i}{\partial x_j} \frac{\partial u_j}{\partial x_i} - \frac{2}{3} \delta_{ij} (\nabla \cdot \mathbf{u})^2 \right), \quad (1.8)$$

due to Ohmic heating and viscous heating respectively. Here,  $\lambda$  is the magnetic diffusivity and  $\mu$  is the magnetic permeability.

## Induction Equation

The final equations concern the magnetic field, which has to fulfil the condition

$$\nabla \cdot \mathbf{B} = 0. \quad (1.9)$$

The induction equation is derived from Maxwell's equations by starting with Ohm's law for a moving conductor and the Maxwell Faraday equation:

$$\frac{1}{\sigma} \mathbf{j} = (\mathbf{E} + \mathbf{u} \times \mathbf{B}), \quad (1.10)$$

$$\nabla \times \mathbf{E} = - \frac{\partial \mathbf{B}}{\partial t}, \quad (1.11)$$

where  $\sigma$  is the electrical conductivity. This is related to the magnetic diffusivity by  $\sigma = 1/\mu\lambda$ . Taking the curl of Ohm's law allows us to substitute in the expression for  $\nabla \times \mathbf{E}$  from the latter. To arrive at the induction equation in its final form Ampère's law is required, simplified in the non-relativistic limit:

$$\mathbf{j} = \frac{1}{\mu} \nabla \times \mathbf{B}. \quad (1.12)$$

This yields:

$$\frac{\partial \mathbf{B}}{\partial t} = \nabla \times (\mathbf{u} \times \mathbf{B}) - \nabla \times (\lambda \nabla \times \mathbf{B}). \quad (1.13)$$

The fact that the magnetic diffusivity remains inside the curl means that spatial derivatives in  $\lambda$  influence the dynamics.

### 1.4.2 Adiabatic Reference State and Convective Perturbations

In gas giants, the fluid motions are assumed to be vigorous enough so that there is efficient heat transfer. Therefore, the system is assumed to be close to adiabatic. Thus, the governing equations are approached by solving for small convective perturbations, denoted by subscript  $c$ , around an adiabatic, steady reference state, denoted by tilde:

$$x = \tilde{x}(r) + x_c(r, \theta, \phi, t), \quad \frac{x_c(r, \theta, \phi, t)}{\tilde{x}(r)} = \epsilon \ll 1. \quad (1.14)$$

The reference state is hydrostatic, adiabatic, and non-magnetic:

$$0 = -\nabla \tilde{p} + \tilde{\rho} \tilde{\mathbf{g}} = -\frac{d\tilde{p}}{dr} - \tilde{\rho} \tilde{\mathbf{g}}, \quad (1.15)$$

$$0 = \nabla \cdot (k \nabla \tilde{T}), \quad (1.16)$$

Subtracting the hydrostatic balance, Eq. 1.15, from Eq. 1.4, expanded using this formulation, allows us to write the Navier-Stokes equation for these convective perturbations:

$$\partial_t \mathbf{u} + (\mathbf{u} \cdot \nabla) \mathbf{u} + 2\boldsymbol{\Omega} \times \mathbf{u} = -\frac{1}{\tilde{\rho}} \nabla p_c + \mathbf{g}_c + \frac{\rho_c}{\tilde{\rho}} \tilde{\mathbf{g}} + \frac{1}{\tilde{\rho}} \mathbf{j} \times \mathbf{B} + \mathbf{F}_v, \quad (1.17)$$

where higher order terms have been neglected.

The conservation of mass, Eq. 1.3, can be approximated in two ways:

$0 = \nabla \cdot (\tilde{\rho} \mathbf{u})$	Anelastic Approximation	(1.18)
--	-------------------------	--------

$0 = \nabla \cdot \mathbf{u}$	Boussinesq Approximation	(1.19)
-------------------------------	--------------------------	--------

The anelastic approximation neglects the term  $\partial_t(\rho_c)$  by assuming that convective density perturbations are much smaller than the values of the adiabatic background state. We consider the convective turnover time  $\tau_{conv} = d_c/U_c$  as a reference, where  $d_c$  and  $U_c$  are typical convective eddy length-scales and velocities respectively. Shorter time-scales are essentially not considered in this system, effectively filtering out sound waves. The Boussinesq approximation goes one step further and assumes that the adiabatic background density is constant. This yields that the divergence of  $\mathbf{u}$  must be zero. This has the benefit of simplifying many of the equations. However, it is only really a valid assumption for layers with a very small density gradient. Nevertheless, the simpler Boussinesq equations can still be used effectively to analyse phenomena that are not strongly influenced by a background density stratification (see discussion of numerical models in Section 1.5.2).

To make the final expansion for the heat equation (1.6), a slightly adapted expression is used for the entropy:  $S = \tilde{S} + S_*(r) + S_c(r, \theta, \phi, t)$ . Here,  $\tilde{S} = const.$  as we assume the system is near-to adiabatic;  $S_*(r)$  is a particular radial background profile which is introduced, in the form of a prescribed  $dS_*/dr$ , to implement a stably stratified layer (see Section 1.4.5); and  $S_c$  is the convective perturbation. As  $\tilde{S}$  has no temporal or spacial derivatives associated with it, it is dropped before substituting in the entropy. This yields:

$$\begin{aligned} \tilde{\rho} \tilde{T} (\partial_t S_c + (\mathbf{u} \cdot \nabla) S_* + (\mathbf{u} \cdot \nabla) S_c) &= \nabla \cdot (k \nabla T_c) + Q_{ohm} + Q_v, \\ \rightarrow \quad \partial_t S_c + u_r \frac{dS_*}{dr} + (\mathbf{u} \cdot \nabla) S_c &= \frac{1}{\tilde{\rho} \tilde{T}} \nabla \cdot (k \nabla T_c) + \frac{1}{\tilde{\rho} \tilde{T}} Q_{ohm} + \frac{1}{\tilde{\rho} \tilde{T}} Q_v. \end{aligned} \quad (1.20)$$

### Adiabatic Reference State

To continue, the adiabatic reference state must be defined. Henceforth, the ideal gas approximation is made, so  $p = (c_p - c_v)\rho T$ . The change in entropy can be written as:

$$0 = dS = \left. \frac{\partial S}{\partial T} \right|_p dT + \left. \frac{\partial S}{\partial p} \right|_T dp = \frac{c_p}{T} dT - \frac{1}{T\rho} dp, \quad (1.21)$$

$$\text{or } 0 = dS = \left. \frac{\partial S}{\partial \rho} \right|_p d\rho + \left. \frac{\partial S}{\partial p} \right|_\rho dp = -\frac{c_p}{\rho} d\rho + \frac{c_v}{p} dp, \quad (1.22)$$

where the specific heat capacity at constant pressure  $c_p$ , the specific heat capacity at constant volume  $c_v$ , and the thermal expansion coefficient  $\tilde{\alpha}$  are defined as:

$$c_p = T \left. \frac{\partial S}{\partial T} \right|_p, \quad c_v = T \left. \frac{\partial S}{\partial T} \right|_v, \quad \tilde{\alpha} = \rho \left. \frac{\partial S}{\partial p} \right|_T = \frac{1}{\tilde{T}} \quad (\text{for Ideal Gas}). \quad (1.23)$$

Considering first Eq. 1.21 then Eq. 1.22 and using the equation for hydrostatic balance, it follows that:

$$\frac{1}{\tilde{T}} \frac{d\tilde{T}}{dr} = -\frac{\tilde{g}}{c_p \tilde{T}} \quad (1.24)$$

$$\frac{1}{\tilde{\rho}} \frac{d\tilde{\rho}}{dr} = -\frac{c_v}{c_p(c_p - c_v)} \frac{\tilde{g}}{\tilde{T}}. \quad (1.25)$$

### Convective Perturbations

Eqs. 1.21 and 1.22 can also be linearised around a background state to give expressions for the perturbed terms:

$$\frac{T_c}{\tilde{T}} = \frac{c_p - c_v}{c_p} \frac{p_c}{\tilde{p}} + \frac{1}{c_p} S_c, \quad (1.26)$$

$$\frac{\rho_c}{\tilde{\rho}} = \frac{c_v}{c_p} \frac{p_c}{\tilde{p}} - \frac{1}{c_p} S_c. \quad (1.27)$$

Using these relations the following expression can be written:

$$-\frac{1}{\tilde{\rho}} \nabla p_c + \frac{\rho_c}{\tilde{\rho}} \tilde{\mathbf{g}} + \mathbf{g}_c \approx -\frac{1}{\tilde{\rho}} \nabla p_c + \mathbf{g}_c - \frac{S_c}{c_p} \tilde{\mathbf{g}} \quad (1.28)$$

$$\approx -\nabla \pi - \frac{S_c}{c_p} \tilde{\mathbf{g}}, \quad (1.29)$$

where  $\pi = p_c/\tilde{\rho} + \Psi_c$  and  $\nabla \Psi_c = -\mathbf{g}_c$ , following Braginsky and Roberts (1995). This further simplifies the Navier-Stokes equation in the form given in Eq. 1.17.

$$\partial_t \mathbf{u} + (\mathbf{u} \cdot \nabla) \mathbf{u} + 2\boldsymbol{\Omega} \times \mathbf{u} = -\nabla \pi - \frac{S_c}{c_p} \tilde{\mathbf{g}} + \frac{1}{\tilde{\rho}} \mathbf{j} \times \mathbf{B} + \mathbf{F}_v. \quad (1.30)$$

In addition, thermal conductivity can be expressed as  $k = \kappa \tilde{\rho} c_p$ , where  $\kappa$  is the thermal diffusivity. Approximating the entropy flux with an entropy diffusion, means Eq. 1.20 can be written as:

$$\partial_t S_c + u_r \frac{d\tilde{S}}{dr} + (\mathbf{u} \cdot \nabla) S_c = \frac{1}{\tilde{\rho}\tilde{T}} \nabla \cdot (\kappa \tilde{\rho} \tilde{T} \nabla S_c) + \frac{1}{\tilde{\rho}\tilde{T}} Q_{ohm} + \frac{1}{\tilde{\rho}\tilde{T}} Q_v. \quad (1.31)$$

### 1.4.3 Non-Dimensionalisation

To solve the governing equations, they are first non-dimensionalised using the shell thickness for the length-scale  $d = r_o - r_i$ , viscous diffusion time as the time scale  $\tau = d^2/\nu$  and the entropy gradient at the upper boundary for the entropy scale  $d|d\tilde{S}/dr|_o$ .

$$\frac{\partial \mathbf{u}}{\partial t} + (\mathbf{u} \cdot \nabla) \mathbf{u} = -\nabla \pi - \frac{2}{E} \mathbf{e}_z \times \mathbf{u} + \frac{Ra}{Pr} \tilde{g} S_c \mathbf{e}_r + \frac{1}{Pm E \tilde{\rho}} (\mathbf{j} \times \mathbf{B}) + \mathbf{F}_v \quad (1.32)$$

$$\partial_t S_c + u_r \frac{dS_*}{dr} + (\mathbf{u} \cdot \nabla) S_c = \frac{1}{Pr \tilde{\rho} \tilde{T}} \nabla \cdot (\kappa \tilde{\rho} \tilde{T} \nabla S_c) + \frac{Pr Di}{Ra} \frac{1}{\tilde{\rho} \tilde{T}} \left[ Q_{ohm} + \frac{1}{Pm^2 E} Q_v \right], \quad (1.33)$$

$$\frac{\partial \mathbf{B}}{\partial t} = \nabla \times (\mathbf{u} \times \mathbf{B}) - \frac{1}{Pm} \nabla \times (\lambda \nabla \times \mathbf{B}), \quad (1.34)$$

where Dissipation number  $Di = (\alpha d/c_p) \tilde{g}$ , a measure of the background density stratification. The further non-dimensional parameters introduced here (see Section 1.4.3 for a discussion of their values in the gas planets and in typical simulations) have been defined as:

$$\boxed{\text{Rayleigh Number: } Ra = \frac{\text{buoyancy}}{\text{viscous diffusion}} \approx \frac{gd^4}{c_p \kappa \nu} \frac{dS_*}{dr}} \quad (1.35)$$

Convection starts above the critical Rayleigh number  $Ra_*$  and the more supercritical it becomes, the more vigorous convection is.

$$\boxed{\text{Ekman Number: } E = \frac{\text{viscous diffusion}}{\text{Coriolis force}} \approx \frac{\nu}{\Omega d^2}} \quad (1.36)$$

The gas giants are characterised by extremely low Ekman numbers as viscosity is very low and they are rapidly rotating planets. It also defines the thickness of the "Ekman Layer", i.e. the boundary layer due to drag, in systems with a no-slip boundary condition.

$$\boxed{\text{Prandtl Number: } Pr = \frac{\text{viscous diffusivity}}{\text{thermal diffusivity}} = \frac{\nu}{\kappa}} \quad (1.37)$$

$$\boxed{\text{Magnetic Prandtl Number: } Pm = \frac{\text{viscous diffusivity}}{\text{magnetic diffusivity}} = \frac{\nu}{\lambda}} \quad (1.38)$$

The two Prandtl numbers describe what form of diffusion dominate the system. At large values of  $Pr$  and  $Pm$  viscous diffusion governs the behaviour. At small  $Pr$ , thermal diffusion is more significant while at small  $Pm$  magnetic diffusion dominates.

As well as the numbers above which are typically the control parameters for numerical simulations, there are also helpful non-dimensional diagnostic parameters which help to characterise the dynamics of the system:

$$\boxed{\text{Rossby Number: } Ro = \frac{\text{advection}}{\text{Coriolis force}} \approx \frac{U}{\Omega d}} \quad (1.39)$$

The Rossby number was previously introduced to quantify the zonal wind speed at the surfaces of Jupiter and Saturn in Fig. 1.2 as it facilitates the comparison of speeds relative

to the rotating system they are in. Here,  $U$  is the zonal flow amplitude and the length scale is the planetary radius. It can also be used with respect to convection, often termed the convective Rossby number  $Ro_c$  (see Chapters 2 and 3 for the definition), where a flow with  $Ro_c < 1$  is rotationally dominated.

$$\text{Reynolds Number: } Re = \frac{\text{advection}}{\text{viscous diffusion}} \approx \frac{Ud}{\nu} \quad (1.40)$$

The Reynolds numbers, in particular those associated with the zonal flow, are extremely high in the gas giants.

$$\text{Magnetic Reynolds Number: } Rm = \frac{\text{induction}}{\text{magnetic diffusion}} \approx \frac{UL}{\lambda} \quad (1.41)$$

The relative importance of the two terms in the induction equation (see Eq. 1.34) is quantified by the magnetic Reynolds number. Here, in systems with variable conductivity, the length scale is often best characterised using the conductivity scale height  $d_\sigma = d \ln(\sigma)/dr$ .

#### 1.4.4 Characteristics of a Rotating System

Rotationally dominated systems have certain features, already alluded to in the description of the analysis of the zonal wind associated gravity moments in Section 1.2.1.

#### Geostrophy and Taylor-Proudman Theory

When considering rapidly rotating systems where the Coriolis force dominates over both inertial and viscous forces,  $Ro \ll 1$  and  $E \ll 1$ . Furthermore, motions are assumed to be very slow, so the time derivative can be neglected, and electrical conductivity is still negligible so there are no Lorentz forces. In this limit the conservation of momentum, Eq. 1.32, reduces to:

$$0 = -\nabla\pi - \frac{2}{E}\mathbf{e}_z \times \mathbf{u} \left[ + \frac{Ra}{Pr}\tilde{g}S_c\mathbf{e}_r \right]. \quad (1.42)$$

In the convective region the term in brackets is negligible (discussed in the following section) and the remainder describes the ‘geostrophic balance’, where forces due to pressure gradients are balanced by the Coriolis force. Taking the curl of this yields the equation for the conservation of vorticity, in this reduced form, where latitudinal and longitudinal entropy variations are neglected for now:

$$0 = (2\Omega \cdot \nabla)\mathbf{u} \rightarrow \partial_z u_\phi = \partial_z u_s = \partial_z u_z = 0. \quad (1.43)$$

This describes the ‘Taylor-Proudman Theorem’. The physical implication is that flow is invariant along  $z$ , the axis of rotation. Note that this applies to velocity, not mass flux, so is equally valid in compressible systems.

## Thermal Wind

As a crucial part of this thesis concerns the quenching of zonal winds, it is clear that there must be a depth at which geostrophy, i.e.  $z$ -invariance, is broken and the winds decay. When analysing this, the term in brackets in Eq. 1.42 is vital. Again taking the curl of this equation, while retaining the term, and considering the azimuthal components leads to:

$$\frac{2}{E} \partial_z (\bar{u}_\phi) \simeq \frac{Ra}{Pr} \frac{\tilde{g}}{r} \partial_\theta S', \quad (1.44)$$

This represents the "Thermal Wind" equation. This balance indicates that if zonal flow is attenuated at depth, latitudinal entropy variations must be responsible. It has been found that even in regions where Lorentz forces play a dominant role, the magnetic term which has been neglected here remains small (discussed in Section 3.3.4) and thermal wind still governs the balance.

### 1.4.5 Flows with Stable Stratification

As detailed in Section 1.2, regions of stable stratification play a crucial role in gas planet interiors and affect both their magnetic fields and zonal winds. The two studies described in this thesis consider both incompressible and compressible flows (using the Boussinesq and anelastic approximations respectively). Both studies have regions of stable stratification. Whether these are due to differences in chemical composition or thermal stratification, the physical effect on convection is the same and illustrated in Fig. 1.12.

In a stably stratified layer, a displaced fluid parcel will return to its equilibrium depth due to the restoring buoyancy force. The parcel overshoots its equilibrium position in an oscillatory motion with a characteristic frequency called the Brunt-Väisälä frequency  $N$ . This is derived by taking the radial component of the Navier-Stokes equation (Eq. 1.32), retaining only the time evolution and buoyancy term, and the heat equation:

$$\begin{aligned} \frac{\partial u_r}{\partial t} &= \frac{Ra}{Pr} \tilde{g} S_c, & \frac{\partial S_c}{\partial t} &= -u_r \frac{dS_*}{dr}, \\ \rightarrow \quad \frac{\partial^2 u_r}{\partial t^2} &= \frac{Ra}{Pr} \tilde{g} \left( -u_r \frac{dS_*}{dr} \right) = N^2 u_r \end{aligned} \quad (1.45)$$

$$\text{Brunt-Väisälä frequency: } N = \sqrt{-\frac{Ra}{Pr} \tilde{g} \frac{dS_*}{dr}}. \quad (1.46)$$

$$\text{Relative to rotation } \frac{N}{\Omega} = \sqrt{-\frac{Ra E^2}{Pr} \tilde{g} \frac{dS_*}{dr}}. \quad (1.47)$$

Eq. 1.45 is the wave equation for gravity waves which can be solved for  $u_r \propto U_r \exp(Nt)$ . When  $dS_*/dr > 0$ , the exponent is imaginary and the solution describes sinusoidal oscillations. Thus, the buoyancy force provides a restoring force for a rising fluid parcel which then sinks again (left panel of Fig. 1.12), causing an oscillating motion and suppressing convection. When  $dS_*/dr < 0$  the exponent is real and a radially upward motion is not inhibited and the region is convectively unstable (Fig. 1.12 right panel).

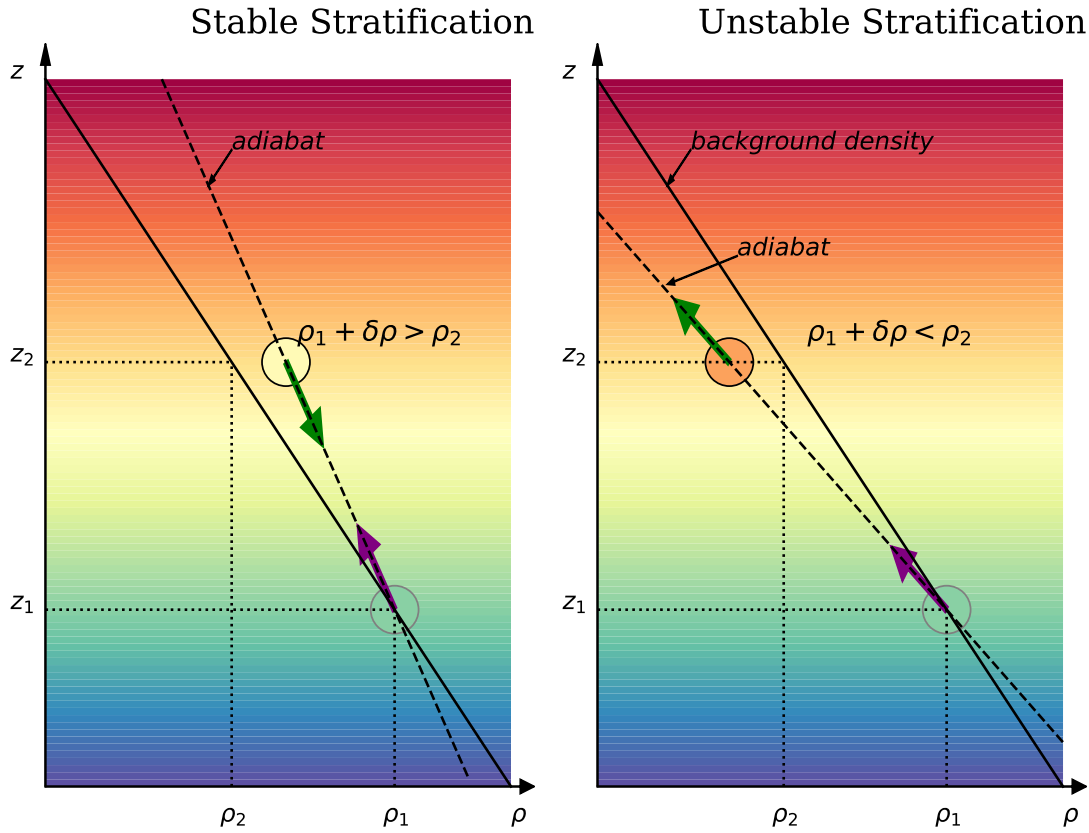


**Figure 1.12.** Schematic showing stable and unstable stratification in a compressible fluid. The solid black line marks the background density profile. Purple arrows show the initial displacement of the fluid parcel, indicated by the filled circle. Under stable stratification, the parcel will rise, where the adiabat is given by a dashed line. As it rises the density decrease is smaller than that of the adiabat and the resultant buoyancy force, shown by the green arrow, is downwards and the parcel sinks again. When the fluid parcel rises and is decompressed in the unstable case its density decrease is greater than that of the ambient density, and the parcel continues to rise (the green arrow points upwards).

#### 1.4.6 Planetary Magnetic Fields and Zonal Flows

In this section some key mechanisms describing how zonal flows and magnetic fields interact are outlined. Eq. 1.13 in Section 1.4.1 comprises of two terms on the right hand side. The first,  $\nabla \times (\mathbf{u} \times \mathbf{B})$ , is the induction term and the second,  $-\nabla \times (\lambda \nabla \times \mathbf{B})$ , is the diffusion term. The induction equation can be expanded to:

$$\nabla \times (\mathbf{u} \times \mathbf{B}) = \underbrace{\mathbf{u}(\nabla \cdot \mathbf{B})}_{=0} - \underbrace{\mathbf{B}(\nabla \cdot \mathbf{u})}_{\text{compression}} + \underbrace{(\mathbf{B} \cdot \nabla)\mathbf{u}}_{\text{shear}} - \underbrace{(\mathbf{u} \cdot \nabla)\mathbf{B}}_{\text{advection}}. \quad (1.48)$$

The first term is zero, see Eq. 1.9, and the second term is also zero when using the Boussinesq approximation. Under the anelastic approximation we have  $\nabla \cdot \mathbf{u} = -u_r d \ln(\tilde{\rho})/dr$ . Since we are interested in the action of zonal flow we focus on the shear term and first decompose the velocity and magnetic fields into their axisymmetric (overbar) and non-

axisymmetric (primed) constituents:

$$\overline{(\mathbf{B} \cdot \nabla) \mathbf{u}} = \overline{((\bar{\mathbf{B}} + \mathbf{B}') \cdot \nabla)(\bar{\mathbf{u}} + \mathbf{u}')} = (\bar{\mathbf{B}} \cdot \nabla) \bar{\mathbf{u}} + \overline{(\mathbf{B}' \cdot \nabla) \mathbf{u}'}, \quad (1.49)$$

where Reynolds averaging rules have been used. Taking the azimuthal component of this yields the expression for the so-called  $\Omega$ -effect<sup>2</sup>, which describes the induction of  $\bar{B}_\phi$ :

$$[(\bar{\mathbf{B}} \cdot \nabla) \bar{\mathbf{u}}]_\phi = \bar{B}_r \frac{\partial}{\partial r} \left( \frac{\bar{u}_\phi}{r} \right) + \frac{\bar{B}_\theta \sin \theta}{r} \frac{\partial}{\partial \theta} \left( \frac{\bar{u}_\phi}{\sin \theta} \right). \quad (1.50)$$

In this expression we can directly see the connection between the zonal winds,  $\bar{u}_\phi$ , and the azimuthal field that is generated. Its strength and structure will depend on the shear of the dipole-dominated radial and latitudinal field by the flow profile in the radial direction (typically decaying in amplitude with depth, in the semi-conducting region that the winds penetrate into) and the gradients between alternating jets, respectively.

The diffusive term destroying this  $\bar{B}_\phi$  field is given by:

$$[\nabla \times (\tilde{\lambda} \nabla \times \bar{\mathbf{B}})]_\phi = -\tilde{\lambda} \nabla^2 \bar{B}_\phi - \frac{\tilde{\lambda} \bar{B}_\phi}{r^2 \sin^2 \theta} + \frac{\partial \tilde{\lambda}}{\partial r} \frac{1}{r} \frac{\partial (r \bar{B}_\phi)}{\partial r}, \quad (1.51)$$

where  $\tilde{\lambda}$  is the radially dependent background magnetic diffusivity. We can also rewrite this prefactor using the diffusivity scale height  $d_\lambda = d \ln(\tilde{\lambda})/dr$ . The third term is zero if this is constant. However, if there is a sharp decrease in diffusivity, when entering the conducting region, this term is crucial.

## 1.5 Models for (Deep) Zonal Jets

### 1.5.1 Theoretical

Before the gravity measurements from the Juno and Cassini missions revealed the extent of the zonal winds into the gas giants, both deep and shallow zonal jet models were studied extensively. In fact, the two types of model rather divided the scientific community. As this debate was then laid to rest with the gravity measurements, this thesis reviews only those concerned with deep-rooted zonal flow structures. These models typically treat the outer convective region as purely hydrodynamic, effectively decoupled from the electrically conducting region below. The winds' inherent connection with small scale flows has already been hinted at when describing the eddies measured at the surface in Section 1.3.1. This can be better understood by taking the azimuthal component of the Navier-Stokes equation (Eq. 1.32) and averaging over longitude. Considering only the inertial term first and using:

$$\mathbf{u} \cdot \nabla \mathbf{u} = \frac{1}{\tilde{\rho}} \nabla (\tilde{\rho} u u) - \frac{1}{\tilde{\rho}} \mathbf{u} \underbrace{\nabla \cdot (\tilde{\rho} \mathbf{u})}_{=0}, \quad (1.52)$$

<sup>2</sup>Not to be confused with the planetary rotation rate. We use  $\Omega$  in this context as it is the accepted name. It comes from the solar MHD community where it refers to the local rotation vector, i.e. differential rotation, which is the cause of this effect.

Reynolds averaging rules then yield:

$$\overline{(\mathbf{u} \cdot \nabla) \mathbf{u}}|_{\phi} = \overline{[(\bar{\mathbf{u}} + \mathbf{u}') \cdot \nabla] (\bar{\mathbf{u}} + \mathbf{u}')}|_{\phi} = (\bar{\mathbf{u}} \cdot \nabla) \bar{\mathbf{u}}|_{\phi} + \overline{(\mathbf{u}' \cdot \nabla) \mathbf{u}'}|_{\phi} \quad (1.53)$$

$$\begin{aligned} &= \bar{u}_s \frac{\partial \bar{u}_{\phi}}{\partial s} + \bar{u}_z \frac{\partial \bar{u}_{\phi}}{\partial z} + \frac{\bar{u}_{\phi} \bar{u}_s}{s} + \frac{1}{\tilde{\rho}} \nabla (\tilde{\rho} \bar{u}' \bar{u}')|_{\phi} \\ &= \underbrace{\frac{\bar{u}_s}{s} \partial_s (s \bar{u}_{\phi}) + \bar{u}_z \partial_z (\bar{u}_{\phi})}_{\text{advective force}} + \underbrace{\frac{1}{s^2 \tilde{\rho}} \partial_s (s^2 \tilde{\rho} \bar{u}'_s \bar{u}'_{\phi}) + \frac{1}{\tilde{\rho}} \partial_z (\tilde{\rho} \bar{u}'_z \bar{u}'_{\phi})}_{\text{Reynolds stress divergence}}. \end{aligned} \quad (1.54)$$

Here, the first two terms have been called the advective force while last two terms represent the Reynolds stress divergence. In this discussion the Lorenz force is neglected as the winds reside in the non-conducting region. The time derivative  $\partial_t u_{\phi}$  vanishes under the assumption that the zonal winds are steady in time. The azimuthal force balance is then given by:

$$\begin{aligned} 0 &= \frac{2}{E} \tilde{\rho} \bar{u}_s && \boxed{\text{Coriolis force}} \\ &+ \frac{\tilde{\rho} \bar{u}_s}{s} \partial_s (s \bar{u}_{\phi}) + \tilde{\rho} \bar{u}_z \partial_z (\bar{u}_{\phi}) && \boxed{\text{Advective force}} \\ &+ \frac{1}{s^2} \partial_s (s^2 \tilde{\rho} \bar{u}'_s \bar{u}'_{\phi}) + \partial_z (\tilde{\rho} \bar{u}'_z \bar{u}'_{\phi}) && \boxed{\text{Reynolds stress divergence}} \\ &- \frac{1}{s^2} \partial_s \left[ \tilde{\rho} s^3 \partial_s \left( \frac{\bar{u}_{\phi}}{s} \right) \right] - \partial_z \left[ \tilde{\rho} \partial_z (\bar{u}_{\phi}) \right]. && \boxed{\text{Viscous force}} \end{aligned} \quad (1.55)$$

Integrating this equation over cylinders, with radius  $s$  and height  $h$ , where this is the height of the convective region, reveals the driving force of the zonal winds:

$$\begin{aligned} 0 &= \int_h \frac{1}{s^2} \partial_s (s^2 \tilde{\rho} \bar{u}'_s \bar{u}'_{\phi}) dz - \int_h \frac{1}{s^2} \partial_s \left[ s^3 \tilde{\rho} \partial_s \left( \frac{\bar{u}_{\phi}}{s} \right) \right] dz \\ \rightarrow \quad 0 &= \int_h \tilde{\rho} \bar{u}'_s \bar{u}'_{\phi} dz - \int_h s \tilde{\rho} \partial_s \left( \frac{\bar{u}_{\phi}}{s} \right) dz. \end{aligned} \quad (1.56)$$

The Coriolis force vanishes since there can be no net mass flux across a vertical cylinder. Furthermore, as the winds extend down geostrophically, invariant to  $z$ , the remaining terms from the advective and viscous forces also do not contribute. Thus, Eq. 1.56 demonstrates that there is a balance between the zonal wind shear and non-linear inertial effects. This is shown in an idealised way in Fig. 1.13a. Here, a top-down view shows how the tilt of the convective cylinders leads to a positive or negative correlation of  $u'_s u'_{\phi}$  and corresponds to the shear between the zonal winds. However, note that the balance in Eq. 1.56 holds over the integrated cylinder, not necessarily locally. Therefore, while the shear term  $\partial_s (\bar{u}_{\phi}/s)$  may be assumed to be constant along  $z$  due to Taylor-Proudman theory, the Reynolds stresses may be distributed unevenly over the cylindrical surface. Therefore, it is possible that the winds are mainly driven near the surface, despite reaching through the whole outer convective region.

In the following section the concepts of zonal flows extending on vertical cylinders, into a planetary interior are discussed with an idealised theoretical approach.

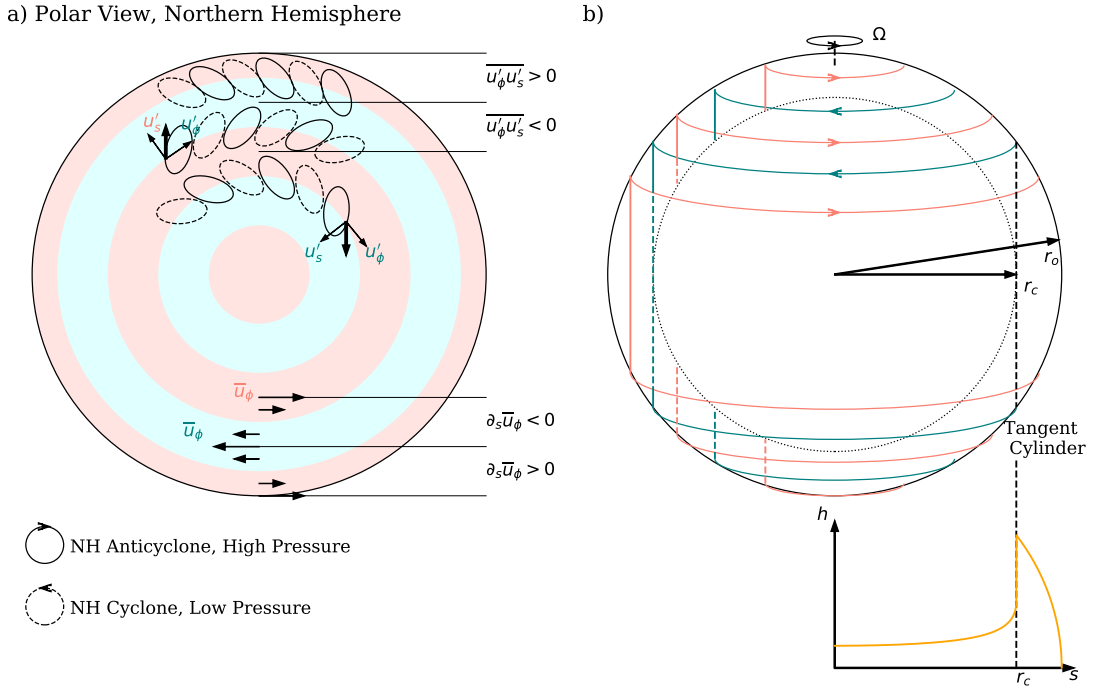


**Figure 1.13.** a) Schematic of a polar view of surface zonal flows (red and blue shading represents opposite flow). In the lower half a zone,  $\partial_s \overline{u}_\phi < 0$ , and a belt,  $\partial_s \overline{u}_\phi > 0$  is indicated. The connection with the tilt of the convective columns in the respective regions, leading to a correlation of the small-scale flows with the same sign, is illustrated in the top half. Note that this very extremely idealised; convective cylinders are enlarged for visibility and the correlations of these eddies only has a clear significance of long term averaging. b) Illustration of ‘Busse Cylinders’ (Busse 1976), based on similar schematics in Heimpel et al. (2005), Heimpel and Aurnou (2007). Turbulent convection takes place in a thin, rapidly rotating shell, representing the outer envelope of a planet. Red (prograde flow) and blue (retrograde flow) arrows represent zonal jets observed on the surface; vertical lines indicate how they continue downwards as cylinders, aligned with the axis of rotation. The tangent cylinder is marked and the discontinuity in the axial shell height  $h(s)$  at this location, where the two hemispheres directly interact, is plotted below.

### The Busse Cylinder

In Busse (1970, 1976) the theory that the fast surface winds continue on cylinders, into the interior, was first proposed. This entails them being the manifestation of deep rotationally dominated convection in the outer regions of the gas giants and first only explained low latitude jets, which are located outside the TC (the Tangent Cylinder, parallel to the rotation axis and attached to the lower boundary of the convective region).

The classic concept consists of an annulus with tilted ends, representing a cylinder of fluid within a sphere, aligned with its rotation axis. It can be shown that for a very thin annulus, and using the Boussinesq approximation, the system experiences a topographic “ $\beta$ -effect”, as the height of the cylinder is changing due to the tilted ends (Busse 1970).

The  $\beta$ -effect parameterises the spatial dependence of the influence of the Coriolis force, due to curvature in this case.

If, instead, the cylinder has flat ends but a density gradient is applied ( $\tilde{\rho}(s)$ , as gravity is assumed to act towards the centre of the annulus), this gives rise to a compressible  $\beta$ -effect (Busse and Simitev 2014). The two models can also be combined to analyse a compressible system with a change in shell height.

In both simplified models it is found that convection is initiated by thermal Rossby waves travelling in the longitudinal direction and its onset is delayed by increasing rotation rate. The theory enables the prediction of the onset of convection, i.e. a critical Rayleigh number, for three-dimensional spherical shell models (Jones et al. 2009).

### Rhines Scaling

In classical 2D turbulence, energy transfers from larger to smaller scales. However, in a planet there are additional effects due to rotation and boundary curvature, introduced by the spherical shape. These can cause energy to be passed from small eddies to slightly larger ones (Rhines 1975). This inverse energy cascade roughly reaches wavenumber  $k_\beta$ . To parameterise this, the so-called  $\beta$ -effect is considered. See Ingersoll and Pollard (1982), Gastine et al. (2014), Verhoeven and Stellmach (2014) for a derivation and discussion on the topographic  $\beta_h$  and compressible  $\beta_\rho$  parameter. As this rapidly rotating deep convection has a predominantly cylindrical flow structure, the Rhines scaling is given by wavevector in the  $s$  direction;  $\mathbf{k} = \sqrt{|\beta|/2U_{rms}} \hat{s}$  and the Rhines scale is the length scale  $\lambda_\beta = 2\pi/k_\beta$ . For the two approximations the wavenumbers are given by:

$$k_\beta = \sqrt{\frac{|\beta_h|}{2U_{rms}}} = \sqrt{\frac{\Omega}{U_{rms}} \frac{d \ln h}{ds}}, \quad \text{topographic}; \quad (1.57)$$

$$= \sqrt{\frac{|\beta_\rho|}{2U_{rms}}} = \sqrt{\frac{\Omega}{U_{rms}} \frac{\partial \ln M}{\partial s}}, \quad \text{compressible}, \quad (1.58)$$

where  $M$  is the mass integrated along the  $z$  direction;  $M = \int_h \tilde{\rho} dz$ . Note that here the lengthscale  $\lambda_\beta$  applies in the  $s$  direction, i.e.  $\lambda_\beta/2$  is considered to be the cylindrical width of a zonal jet. To reach a relation connecting the jet width with its peak amplitude, one must assume that  $U_{rms}$  is dominated by the zonal wind.

The result is that faster jets are expected to be wider. Heimpel and Aurnou (2007) tested the predicted relation for Jupiter, using the topographic  $\beta$ -parameter and thus obtained an estimate for the depth of its zonal flows of  $0.85–0.95 R_J$ , by testing different aspect ratios. They also noted that Rhines scaling seemed to break down in the equatorial region.

Gastine et al. (2014) studied both Jupiter and Saturn and compared the predictions for the two  $\beta$  parameters. At the mid-latitudes the results are very similar and the topographic and compressible  $\beta$ -parameters approach the same value, especially for very thin convective layers (i.e. Jupiter). Outside the tangent cylinder, the difference is largest and  $\beta_\rho$  predicts a unrealistically narrow jet, just as the topographic  $\beta$ -effect prediction does. As found in Heimpel and Aurnou (2007), therefore, both predictions break down at the equator.

### 1.5.2 Numerical

The era of the study of gas planet-like zonal winds, using three-dimensional numerical models, started at the beginning of this century with Christensen (2001, 2002). These numerical simulations reproduced alternating zonal jets, though with fewer jets than observed on the gas planets. Since then, with increasing computing power, simulations have been driven to gradually more extreme parameters. This started to yield models displaying multiple zonal jets, also at the higher latitudes when using stress-free boundary conditions (Heimpel et al. 2005).

Gastine et al. (2013) explored the transition from rotation to buoyancy dominated regimes, which can be parameterised using the convective Rossby number  $Ro_c$ , as described in Section 1.4.3. It was found that in rotationally dominated systems a prograde equatorial jet forms, driven by Reynolds stresses. This is similar to what is found on the gas giants, and also the sun. For  $Ro_c > 1$ , this reverses and a retrograde equatorial jet is observed, similar to zonal flows on the ice giants. This study was carried out using the MagIC code (<https://magic-sph.github.io/>), also used for this work.

### The Effect of Compressibility

Jones and Kuzanyan (2009), Gastine and Wicht (2012) made numerical studies using the anelastic approximation and found that as the density contrast across the simulated spherical shell is increased, convective motion which is usually initiated near the tangent cylinder, moves progressively further outwards in the shell. Convective flows were also found to be strongest in the less dense outer regions while the denser regions had weaker and larger-scale convective motion. Furthermore, the critical Rayleigh number is found to be higher compared to Boussinesq simulations (Jones et al. 2009).

Gastine et al. (2013) found that in models with a large density gradient a "dimple" started to form within the equatorial jet, similar to that observed on Jupiter (see Fig. 1.2).

### The Effect of Stable Stratification

Both earlier work by Takehiro and Lister (2001) and more recent studies such as Dietrich and Wicht (2018), Gastine et al. (2020) showed that convection is suppressed by a stably stratified layer. It was found that the higher-degree convective motions are quenched first while larger scales can penetrate further into the layer. Furthermore, it was found that the higher the degree of stratification, controlled by a variation of the Brunt-Väisälä frequency (introduced in Section 1.4.5), the more effective the damping of convective motions.

Stable stratification has also been employed at the surface, representing some of the potential effects of a weather layer (Heimpel et al. 2016, Heimpel et al. 2022). These have been more successful in reproducing vortices at the surface, as observed on Jupiter, while being thin enough to still allow the zonal flows to penetrate through from below.

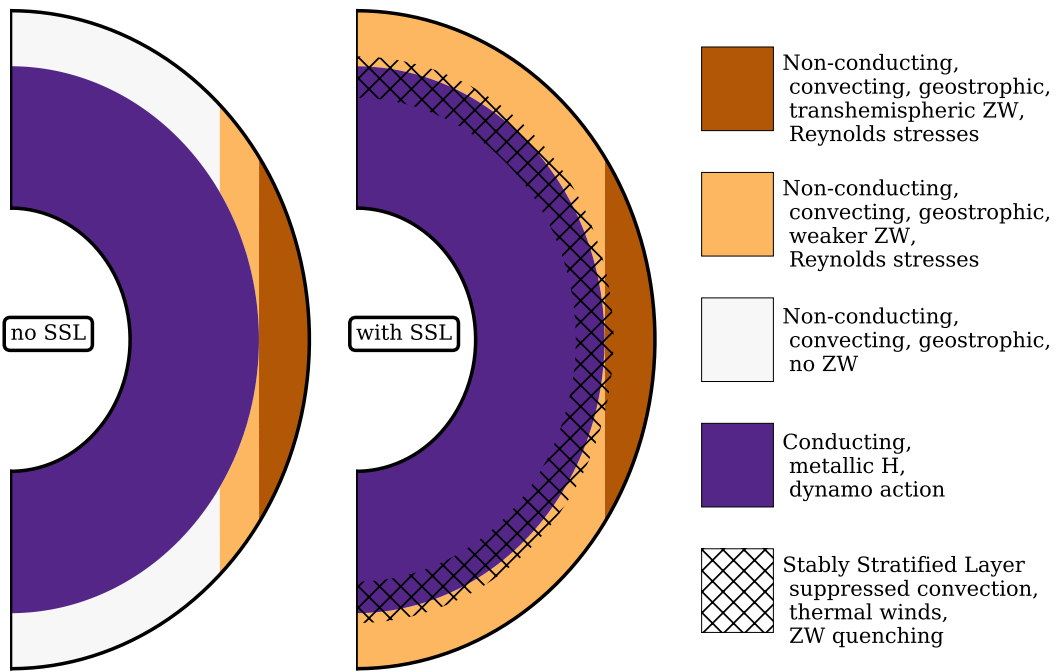


**Figure 1.14.** Schematic illustrating lack of zonal wind formation inside the tangent cylinder when there is a straight transition from convection to the dynamo region. The presence of a stably stratified layer (SSL) helps to decouple the two regions so zonal jets can form above, driven by Reynolds stresses, before being damped in the SSL.

### Limiting the Vertical Extent of Zonal Flows

The critical issue when simulating zonal flows has been finding models which feature zonal jets inside the TC and also account for their decay at depth, illustrated in Fig. 1.14.

- Even the earlier models soon reached parameters where zonal winds formed at the higher latitudes, as described above. However, these were fully convective spherical shells with stress-free lower (and upper) boundary conditions. Therefore, they cannot explain what happens below the outer, hydrodynamic, convective envelope.
- In these earlier studies (e.g. Heimpel et al. (2005), Heimpel and Aurnou (2007)), as well as those calculating zonal wind depth from gravity moments (e.g. Kaspi et al. (2018)), it was often postulated that Lorentz forces could be responsible for the quenching of the zonal winds. However, since then there are studies which have included a variable electrical conductivity, increasing with depth, such as Heimpel and Gómez-Pérez (2011), Duarte et al. (2013), Duarte et al. (2018), Dietrich and Jones (2018). These studies found that either the generated dynamo was weak and multipolar or had a strong dipole. In the former, the Lorentz force had little impact and there was effectively no magnetic tangent cylinder. The zonal flow had a similar morphology as for a thick-shell hydrodynamic model: zonal wind at high latitudes,

but no multiple jets. In the latter, zonal winds were greatly diminished inside the TC associated with the dynamo radius and the only strong flow was the prograde equatorial jet.

Recently, Christensen et al. (2020) proposed that a shallow stably stratified layer may aid in decoupling the deeper electrically conducting region from the convective envelope. Both this study, where the winds were maintained by an ad-hoc driving force, and a later full dynamo simulation by Gastine and Wicht (2021), showed that winds can then be sustained at the higher latitudes and attenuated upon encountering the stable layer. This thesis is based on these new ideas and explores them in two thorough parameter studies.

## 1.6 Numerical Models and their Limitations

### 1.6.1 Numerical Technique

The numerical magnetohydrodynamic (MHD) code used in this thesis is MagIC, available at <https://magic-sph.github.io/>. In this thesis the code is introduced only in a rudimentary fashion and the reader is referred to the website given above for more details.

The MagIC code stems from the pseudo-spectral MHD code developed by Glatzmaier (1984). Both the Boussinesq (Wicht 2002) and anelastic (Gastine and Wicht 2012) version of the code have been well-benchmarked against other codes (see Christensen (2001) and Jones et al. (2011) respectively).

Spectral methods, as opposed to local methods such as finite differences, have the advantage that less grid-points are required. Furthermore, partial derivatives can be calculated analytically, greatly improving the accuracy. The governing equations 1.32, 1.33 and 1.34 are solved in their dimensionless form for a fluid in a spherical shell. From the non-dimensionilisation described in Section 1.4.3, it follows that the velocity field is expressed in terms of a Reynolds number  $Re$  and the magnetic field as an Elsasser number  $\Lambda = B^2\sigma/\rho\Omega$ , a measure for the ratio of the Lorentz force relative to the Coriolis force:

$$[u] = v/d \quad [B] = \sqrt{\rho\Omega/\sigma}. \quad (1.59)$$

#### Poloidal/Toroidal Decomposition

Equations 1.18 or 1.19 (if using the anelastic or Boussinesq approximation respectively) and Eq. 1.9 are automatically satisfied by using a poloidal/toroidal decomposition. This decomposition is given by:

$$\mathbf{u} = \nabla \times (\nabla \times W\mathbf{e}_r) + \nabla \times Z\mathbf{e}_r, \quad \boxed{\text{Boussinesq}} \quad (1.60)$$

$$\tilde{\rho}\mathbf{u} = \nabla \times (\nabla \times W\mathbf{e}_r) + \nabla \times Z\mathbf{e}_r, \quad \boxed{\text{Anelastic}} \quad (1.61)$$

$$\mathbf{B} = \underbrace{\nabla \times (\nabla \times g\mathbf{e}_r)}_{\text{poloidal}} + \underbrace{\nabla \times h\mathbf{e}_r}_{\text{toroidal}}, \quad (1.62)$$

Here,  $Z(r, \theta, \phi)$  and  $h(r, \theta, \phi)$  are the toroidal potentials and  $W(r, \theta, \phi)$  and  $g(r, \theta, \phi)$  are the poloidal potentials. Thus, the three unknown field components of vectors  $\mathbf{u}$  and  $\mathbf{B}$  can be replaced by two scalar fields, respectively, reducing the number of unknowns by two.

Therefore, six unknowns remain: the four potentials, pressure and entropy. These are solved for in the following six equations:

- $W$ : radial component of the Navier-Stokes equation.
- $Z$ : radial component of the curl of the Navier-Stokes equation.
- $g$ : radial component of the induction equation.
- $h$ : radial component of the curl of the induction equation.
- $p$ : horizontal part of the Laplacian, applied to the Navier-Stokes equation.
- $s$ : heat equation.

### Angular and Radial Grid-point Distribution

Spherical harmonic functions are used in the angular directions, e.g. for the magnetic poloidal potential:

$$g = \sum_{\ell=0}^{\ell_{max}} \sum_{m=0}^{\ell} g_{\ell m}(r) Y_{\ell m}(\theta, \phi), \quad (1.63)$$

where  $Y_{\ell m}(\theta, \phi) = P_{\ell m}(\cos \theta) \exp(im\phi)$ .  $\ell$  is the degree and  $m$  is the order (longitudinal wavenumber).

In the radial direction Chebyshev polynomials,  $C_n(x) = \cos(n \arccos(x))$ , are used to expand the coefficients. E.g.  $g_{\ell m}$ :

$$g_{\ell m} = \sum_{n=0}^N g_{n \ell m} C_n(r), \quad (1.64)$$

where  $n$  is the order of the Chebyshev polynomial. The mapping from the radius into the Chebyshev domain is given by:

$$x(r) = 2 \frac{r - r_i}{r_o - r_i} - 1, \quad (1.65)$$

where  $-1 \leq x \leq 1$  and  $r_i \leq r \leq r_o$ .

The choice of radial grid-point distribution, where the  $N_r$  points are located on the extrema of the Chebyshev polynomial of order  $N_r - 1$ , means that Fast Fourier Transforms can be used to evaluate the expansion. This grid also has the convenient property that the grid-point distribution is denser near  $r_i$  and  $r_o$ , so rather optimised for resolving boundary layers sufficiently.

## 1.6.2 Limitations

It is clear that these 3D MHD simulations cannot capture all of the physics in the outer parts of the gas giants. It is important to recognise their limitations when interpreting the results and applying them in the planetary context.

## Boundary Conditions

Simulating a spherical shell as a representation of a specific region within a planet always entails choosing the most appropriate boundary conditions. These are rarely fully accurate for the dynamics in a planet. The most straight-forward is perhaps a shell describing the whole region between a solid core at the centre and the outer surface of a gas planet. In this case a no-slip mechanical boundary condition at  $r_i$  and stress-free at  $r_o$  are the most appropriate.

However, conducting these low aspect ratio simulations is often not the best way to answer specific questions about the dynamics. Thick shell models must incorporate an inner dynamo region and perhaps multiple stable layers. It is near-to impossible to model such a variety of dynamic regions, with different dynamic time-scales, meaningfully in one simulation.

The studies described in this thesis concern themselves with the outer parts of the gas giants. Therefore, both studies take a generalised approach, not seeking to model either planet exactly. We keep an aspect ratio of 0.7, effectively simulating the outer 30% of a planet, with the lower third stably stratified and the upper part convecting.

For the hydrodynamic study, described in Chapter 2, rigid boundary conditions are chosen. In previous fully-convecting models with rigid lower boundary conditions, it was found that no strong zonal winds formed inside the tangent cylinder attached to the inner shell boundary (see Chapter 2, Fig. 2.3a). This was due to viscous stresses at this lower boundary. A similar effect was observed for models with increasing conductivity (as discussed in Section 1.5.2), for a magnetic tangent cylinder. Therefore, we argue that in this particular respect, the viscous stresses at a rigid boundary can act as a proxy for the Maxwell stresses, acting in the MHD models. Therefore, this hydrodynamic set-up allows us to investigate how a stable layer can decouple the dynamics in the overlying convection region from deeper braking mechanisms.

Stress-free conditions are used in the MHD study (described in Chapter 3), where we now include these magnetic effects. As our model does not include the deep dynamo region, the internal magnetic field is incorporated into the boundary condition. To keep the model simple, we assume that an axial dipole can represent this internal field. Therefore, this mode is held fixed at the boundary, for the poloidal magnetic field, while all other modes are solved for a conducting inner "core". As the focus of the study is on the zonal winds formed in the outer convecting envelope, this generalised set-up is effective in studying how the winds interact with a deeper conducting region with such an (imposed) internal field.

## Boussinesq and Anelastic Approximations

The anelastic approximation is valid when the Mach number (defined as  $U/c_s$ , where  $c_s$  is the speed of sound) is small, as it is in these gas giant interiors. For near-surface solar simulations this would not be suitable, for example. When using the anelastic approximation, one should also take care with the adiabatic background profiles that are prescribed as they cannot evolve away from this, as fully compressible simulations allow.

The Boussinesq approximation is even more limited. It affects the onset of convection and its distribution in the spherical shell (see Section 1.5.2). However, it significantly

simplifies the governing equations. Therefore, it can be helpful when reducing a problem down to the key essentials. This is done in the study described in Chapter 3, and some equivalent simulations are conducted using the anelastic approximation to show that the observed trends still hold.

### Non-Dimensional Parameters

The non-dimensional parameters introduced in Section 1.4.3 are given here in Table 1.2. In particular the Ekman numbers are still much lower than what can be achieved with nu-

	Jupiter	Saturn
$\beta = r_i/r_o$	0.96-0.972	0.85-0.875
$E = \nu/\Omega r_o^2(1-\beta)^2$	$10^{-15} - 10^{-20}$	$10^{-15} - 10^{-20}$
$Ra = \alpha g_o \Delta T r_o^3 (1-\beta)^3 / \kappa \nu$	$10^{25} - 10^{30}$	$10^{25} - 10^{30}$
$Pr = \nu/\kappa$	$\sim 0.1$	$\sim 0.1$
$Re = U(r_o - r_i)/\nu$	$10^{15}$	$2 \times 10^{15}$
$Ro = U/(\Omega r_o)$	0.01	0.03

**Table 1.2.** Estimates of non-dimensional parameters for Jupiter and Saturn. Aspect ratio  $\beta$  is based on the depth of the zonal winds. Reynolds number  $Re$  and Rossby number  $Ro$  are based on maximum zonal wind amplitudes.

merical simulations. Thus, it is important to bear in mind that viscosity plays a larger role in these models than would be expected in the gas giants. At the same time the Rayleigh numbers are much higher in the planets. However, the Prandtl number is more achievable (in these studies  $Pr = 1$  and  $Pr = 0.5$  were used). Furthermore, the higher  $E$  and lower  $Ra$  combine to yield a convective Rossby number,  $Ro_c = \sqrt{Ra/PrE}$ , that is also more comparable to that obtained from the values given in Table 1.2.

### Oblateness

Saturn is the least spherical planet in our solar system, with a flattening of  $(R_{eq} - R_{Pol})/R_{eq} = 9.8\%$  at the 1-bar surface (Cao and Stevenson 2017). For Jupiter this is 6.5%. At depth oblateness is less pronounced as it decreases as pressure increases.

All pseudo-spectral codes such as MagIC are restricted to the spherical geometry and it is unclear how incorporating oblateness would affect the models, especially when studying these outer regions.

### Cloud-level Processes

The surface of the gas giants hosts rich dynamics of its own, where the degree of coupling between these shallow processes and the deeper convection, studied in this thesis, is a long-standing point of debate. Density and pressure change dramatically with altitude in this upper region, where the 1 bar pressure level is typically used as the reference

"surface". These steep gradients and the compositional changes associated with them lead to cloud formation, including ammonia clouds at the lower temperatures (higher altitudes), ammonium sulphide clouds, and water clouds at the higher temperatures (lower altitudes). Lightning is also observed on Jupiter, often associated with upflows.

The models discussed in this thesis neglect all of these dynamics, which can make it difficult to connect some observations such as the meridional circulation (Section 1.3) with simulations.

Solar irradiation is also neglected in this work. However, as pointed out in Section 1.1 this is extremely weak on the gas giants, compared to Earth.

# 2 Zonal Winds in the Gas Planets driven by Convection above a Stably Stratified Layer

## *Abstract*

The analysis of the recent gravity measurements of Jupiter and Saturn reveal that the zonal winds observed on their surfaces reach several thousand kilometres deep into their atmospheres. However, it remains unclear which mechanism prevents them from penetrating deeper. Recent models suggest that a stably stratified region would yield the desired effect. In this numerical study we systematically explore the dynamics of flow in a rotating spherical shell where the lower third is stably stratified while convection in the outer region drives multiple zonal winds, similar to those observed on Jupiter or Saturn. When using a rigid lower boundary condition, only an equatorial jet pair is formed without an underlying stable layer. When including a stable layer, fierce multiple jets also develop at mid to high latitudes, once the stable stratification is strong enough to effectively decouple the jet dynamics from the lower boundary. We find that the decay of the jet amplitude near the stable layer boundary is controlled by  $\Omega/N$ , where  $\Omega$  is the rotation rate and  $N$  the Brunt-Väisälä frequency that quantifies the degree of stable stratification. Furthermore, the penetration distance of the jets is proportional to the jet width. In the convective region, the winds are invariant along the axis of rotation, whereas their extension in the stable layer tends to become radially aligned.

## 2.1 Introduction

The zonal winds on our Solar System's Giant Planets, Jupiter and Saturn, have been observed for centuries. Space missions in the last decades, eg. Voyager and Cassini (Porco et al. 2003), as well as Hubble data (Simon et al. 2015), have provided measurements of

---

The contents of this chapter has been reproduced from the article: P. N. Wulff, W. Dietrich, U. R. Christensen, J. Wicht. *Zonal Winds in the Gas Planets driven by Convection above a Stably Stratified Layer*, published in Monthly Notices of the Royal Astronomical Society (2022).

**Contribution:** I ran all of the simulations, performed analyses and wrote the first draft of the paper. After thorough revisions, much of the original content and structure is preserved. W. Dietrich greatly helped with learning how to use the MagIC code and implementing the model. U. R. Christensen established the main research aims and approach. All three co-authors contributed to writing the final draft, physical interpretations of the results and research supervision.

their velocities over almost all latitudes. From these we know that on Jupiter (Saturn) the zonal wind profile is dominated by fierce prograde equatorial jets on the scale of 150 m/s (400 m/s, Sanchez-Lavega et al. (2000)) with multiple, alternating, jets reaching up to the higher latitudes.

Jupiter's surface zonal wind profile also has a considerable degree of equatorial antisymmetry. Therefore, the mere fact that the recent in-situ gravity measurements have revealed non-zero odd gravity moments (Iess et al. 2018) confirmed that these winds reach sufficiently deep to carry enough mass with them to alter the gravity signal. These measurements have provided valuable constraints on how the winds may be extrapolated into the planet's interior. They indicate that, upon continuing downwards geostrophically (invariant along the axis of rotation), the winds in Jupiter are braked at around 2,500-3,500 km depth (Kaspi et al. 2018, Dietrich et al. 2021). For Saturn a depth of around 9000 km has been inferred using similar methods (Galanti et al. 2019). While first estimations of how the winds are quenched with depth in Jupiter gave a rather soft decay profile (Kaspi et al. 2018), this is not reconcilable with the absence of strong secular variation of Jupiter's magnetic field (Moore et al. 2019, Connerney et al. 2022, Bloxham et al. 2022). More recent studies confirm that a sharper decay profile is also compatible with the gravity moment measurements (Galanti et al. 2021). Galanti et al. (2019) find that the winds in Saturn are quenched over a depth of around 3,000 km, but with a rather large uncertainty. Large-scale jets are driven by an upscale transfer of energy through Reynolds stresses, i.e. a correlation of velocity components of small-scale convective vortices (eg. Aurnou and Olson (2001), Christensen (2001), Heimpel et al. (2005), Salyk et al. (2006)). It has been the aim of many numerical modellers in the field to accommodate the various known features of the winds in simulations. One of the main difficulties is reproducing the multiple jets, reaching to the higher latitudes. They can be found in models with stress-free lower boundaries (eg. Heimpel and Aurnou (2007)), which is however, physically unrealistic. For non-magnetic models with a rigid lower boundary, representing some sort of artificial braking, viscous stresses effectively kill all flows within the tangent cylinder (TC), i.e. within the cylinder that touches the inner boundary at the equator and is coaxial to the rotation axis (Aurnou and Heimpel 2004, Jones and Kuzanyan 2009). However, experimental studies, such as Cabanes et al. (2017), Lemasquerier et al. (2021), have had some success in observing rather strong jet flow above a rigid boundary in their experimental setups at Ekman numbers 1-2 orders of magnitude lower than what had been typically achieved in previous numerical simulations, suggesting these suffer from being overly viscous. In our numerical simulations the rigid boundary condition serves as a proxy for the influence of electromagnetic forces, which likewise tend to eliminate jets inside the TC (Heimpel and Gómez-Pérez 2011, Gastine et al. 2014). In magnetic cases the TC boundary is given by the depth at the equator where the electrical conductivity has reached a sufficiently high value (Dietrich and Jones 2018).

More recently it has been proposed that a stably stratified layer (SSL), below the outer convective region, may be the key to producing jets within the TC (Christensen et al. 2020, Gastine and Wicht 2021). In these cases, the TC is then positioned at the boundary to the SSL. For Saturn such a SSL may have its origin in compositional stratification, due to Helium rain. The compositional (He) gradient bridging the He-depleted outer to the He-enriched inner convective zone of Saturn leads to a stably stratified sandwich layer (Lorenzen et al. 2011). Recent experimental studies reaching ever more extreme pressure

and temperature conditions suggest that such a layer may also exist in Jupiter. Brygoo et al. (2021) suggest that this H-He phase-separated layer inside Jupiter would be between  $0.68 - 0.84R_J$ .

Further indications of a SSL in Jupiter, albeit at a shallower depth, emerge from modelling the planet's interior using gravity measurements. Nettelmann et al. (2021) use theory of figures and find that in order to fit these measurements both with the atmospheric metallicity and the surface temperature measured by the Galileo probe, there must be a sub-adiabatic region. Debras et al. (2021) show that a combination of compositional and entropy changes can lead to a stable stratification of this kind.

A measurement which may help to determine the presence of a stably stratified layer are the planet's dynamical Love numbers. With regards to Jupiter, Lai (2021) has shown, by incorporating both a deep ( $r/r_o \in [0.5, 0.7]$ ) and more shallow ( $r/r_o \in [0.85, 0.93]$ ) stably stratified layer into planetary models, that the induced g-mode resonances would be strong enough to affect the observable Love numbers. This could be vital to further constrain the depth of such a layer, should the stratification be strong enough.

There have been some previous studies of how a SSL may effect both convection and larger-scale zonal flows. Takehiro and Lister (2001) and Takehiro (2015) concentrate on small-scale motions and penetrative convection. These hydrodynamic and MHD studies were then extended in Takehiro and Lister (2002) and Takehiro and Sasaki (2018), to analyse penetration of steady zonal winds into the stable layer. These studies predict that, in non-magnetic cases and for strongly stratified stable layers, the penetration distance of the zonal flows into the layer depends only on the jet's length-scale and is almost independent of the degree of stratification. However, all four of these studies use the Boussinesq approximation, and having a more Earth-like focus, position the SSL above the unstable region, similarly to Gastine et al. (2020). Dietrich and Wicht (2018) also investigated penetrative convection in the context of a Saturn-like set-up, with a stably stratified sandwich layer. It was found that the penetration depth of radial flows into the sandwich layer scaled with the square root of the entropy gradient and that the layer acted as a low-pass filter, damping the small-scale flows most effectively.

Christensen et al. (2020) performed simplified axisymmetric simulations with an imposed magnetic field in which winds were driven by an ad-hoc force. They found that a combination of stable stratification and MHD effects leads to winds that decay over a narrow depth interval at the top of the SSL. Thus far, Gastine and Wicht (2021) is the only full MHD study for Jupiter which has incorporated such a layer. They found that the SSL facilitates zonal winds inside the tangent cylinder (TC), although restricted to the region close to the TC boundary. Both studies emphasised the need for both a SSL and magnetic effects to dampen the zonal winds.

Here we take a more simplified approach to study the effect of a stable layer without interference from magnetic effects. We use anelastic simulations of convection in a rotating spherical shell with partially stable stratification and conduct a systematic parameter sweep. We explore how a SSL affects the braking of zonal winds and how they penetrate into this layer. In a gas planet it appears likely that some braking force acts on zonal flows deeper down in a stable region; at a depth where the electrical conductivity becomes significant, electromagnetic forces will enter the force balance and could have a braking effect. In our simulations we apply a rigid boundary condition at the bottom of the stable layer as a proxy for this. The main parameters that we explore are the degree of stability

in the SSL and the degree of background density variation.

## 2.2 Numerical Methods and Model Set-Up

### 2.2.1 Hydrodynamic Equations

We consider a convecting ideal gas in a spherical shell rotating about the  $z$  axis, where the aspect ratio in our main parameter sweep is  $r_i/r_o = 0.7$  (corresponding to outer shell boundary,  $r_o = 3.33$ , and inner boundary,  $r_i = 2.33$ ). As we model the outer 30% of the planet, making the approximation that gravity  $g \propto 1/r^2$  is reasonable. We use the anelastic approximation (Braginsky and Roberts 1995) for the governing equations. We write density, temperature, pressure and entropy as a sum of their reference state (denoted by a tilde) and their fluctuation about this state (denoted by a prime):

$$\rho = \tilde{\rho} + \rho', \quad T = \tilde{T} + T', \quad p = \tilde{p} + p', \quad S = \tilde{S} + S'. \quad (2.1)$$

We non-dimensionalise our governing equations using shell thickness as the length-scale ( $d = r_o - r_i$ ) and viscous diffusion time,  $d^2/\nu$ , as the timescale, where  $\nu$  is a constant kinematic viscosity.  $\nu/d$  is used to scale the velocity and entropy is non-dimensionalised with respect to  $d|d\tilde{S}/dr|_{r_o}$ , i.e. using the imposed entropy gradient at the outer boundary. Reference values for temperature, pressure and gravity are all taken at the upper boundary. We therefore write the continuity equation as:

$$\nabla \cdot (\tilde{\rho}\mathbf{u}) = 0, \quad (2.2)$$

and the momentum equation:

$$\frac{\partial \mathbf{u}}{\partial t} + \mathbf{u} \cdot \nabla \mathbf{u} + \frac{2}{E} \mathbf{e}_z \times \mathbf{u} = -\nabla \frac{p'}{\tilde{\rho}} + \frac{Ra}{Pr} g S' \mathbf{e}_r + \mathbf{F}_v, \quad (2.3)$$

where  $\mathbf{F}_v$  is the viscous force:

$$\mathbf{F}_v = \frac{1}{\tilde{\rho}} \left[ \frac{\partial}{\partial x_j} \tilde{\rho} \left( \frac{\partial u_i}{\partial x_j} + \frac{\partial u_j}{\partial x_i} \right) - \frac{2}{3} \frac{\partial}{\partial x_i} \tilde{\rho} \frac{\partial u_j}{\partial x_j} \right]. \quad (2.4)$$

In order to conserve thermal energy we have:

$$\frac{\partial S'}{\partial t} + \mathbf{u} \cdot \nabla S' + u_r \frac{d\tilde{S}}{dr} = \frac{1}{Pr\tilde{\rho}\tilde{T}} \nabla \cdot (\tilde{\kappa}\tilde{\rho}\tilde{T}\nabla S') + \frac{PrDi}{Ra} \frac{1}{\tilde{\rho}\tilde{T}} Q_v, \quad (2.5)$$

where  $Q_v$  is the viscous heating:

$$Q_v = \sigma_{ij} \frac{\partial u_i}{\partial x_j}, \quad \sigma_{ij} = \tilde{\rho} \left( \frac{\partial u_i}{\partial x_j} + \frac{\partial u_j}{\partial x_i} - \frac{2}{3} \delta_{ij} \nabla \cdot \mathbf{u} \right), \quad (2.6)$$

with  $\sigma_{ij}$ ; the stress tensor. The non-dimensional parameters Rayleigh number, Prandtl number, Ekman number and Dissipation number are defined as:

$$Ra = \frac{\alpha_o T_o g_o d^4}{c_p \nu \kappa_o} \left| \frac{d\tilde{S}}{dr} \right|_{r_o}, \quad Pr = \frac{\nu}{\kappa_o}, \quad E = \frac{\nu}{\Omega d^2}, \quad Di = \frac{\alpha_o g_o d}{c_p}, \quad (2.7)$$

where subscript o indicates values at the outer boundary.  $c_p$  is the specific heat and  $\kappa$  is the thermal diffusivity (which varies with radius as described in Dietrich and Wicht (2018)). In later analysis we will primarily use spherical polar coordinates  $(r, \theta, \phi)$ , but also cylindrical coordinates,  $(s, z, \phi)$ , where more appropriate. Here  $s = r \sin \theta$ , the distance from the axis of rotation, and  $z = r \cos \theta$ , the distance from the equatorial plane, parallel to the axis of rotation.

The mechanical boundary conditions are impenetrable and stress-free at the top boundary and no-slip at the bottom boundary, except for one comparison case, where stress-free are used. The thermal boundary conditions are fixed entropy at the top of the shell ( $S' = 0$ ) and fixed entropy flux ( $dS'/dr = 0$ ) at the inner shell boundary.

### 2.2.2 Background Profiles

In order to implement the SSL, we fix the background entropy gradient in the unstable top layer to  $d\tilde{S}/dr = -1$  and in the deep stably stratified layer to a positive value  $A_s$ . The transition is smoothed using a hyperbolic tangent function:

$$\frac{d\tilde{S}}{dr} = -\frac{1}{2}(A_s + 1) \cdot \left[ 1 - \tanh\left(\frac{r_s - r}{\delta_s}\right) \right] + A_s, \quad (2.8)$$

where  $\delta_s$  is the radial extent of the transition region and  $r_s$  is the midpoint of the hyperbolic tangent.

There is neutral stratification where  $d\tilde{S}/dr = 0$ , which separates the super-adiabatic region and the SSL, and is at a slightly shallower depth than  $r_s$ .

In all cases in this study we choose  $r_s = 2.67 \approx 0.8r_o$  and  $\delta_s = 0.02$ . It is difficult to determine exactly how sharp this transition would be in a gas planet so for this simplified parameter study we chose a value and ensured that is not too steep as to lead to numerical resolution issues. Approximately the lower 1/3 of the shell is stably stratified and the upper 2/3 are convectively unstable.

Following Dietrich and Wicht (2018), we incorporate the variation in background entropy into the equations defining the reference state. In contrast to the latter study, we do not use a Jupiter model for the thermodynamic properties but simplify by assuming a polytropic equation of state with index  $n = 2$ . This leads to the following equations for the non-dimensional background temperature ( $\tilde{T}$ ) and density ( $\tilde{\rho}$ ) profiles

$$\frac{1}{\tilde{T}} \frac{d\tilde{T}}{dr} = \epsilon_s \frac{d\tilde{S}}{dr} - \frac{Di}{\tilde{T}} \tilde{g}(r) \quad (2.9)$$

$$\frac{1}{\tilde{\rho}} \frac{d\tilde{\rho}}{dr} = \epsilon_s \frac{d\tilde{S}}{dr} - \frac{nDi}{\tilde{T}} \tilde{g}(r). \quad (2.10)$$

with  $\epsilon_s$ , the relative deviation from the adiabat:

$$\epsilon_s = \frac{d}{c_p} \left| \frac{d\tilde{S}}{dr} \right|_{r_i} \quad (2.11)$$

For an adiabatic reference state  $\epsilon_s = 0$ . For the anelastic approximation to remain valid, the deviations from the adiabat must still be small. We set  $\epsilon_s = 10^{-4}$  to ensure that

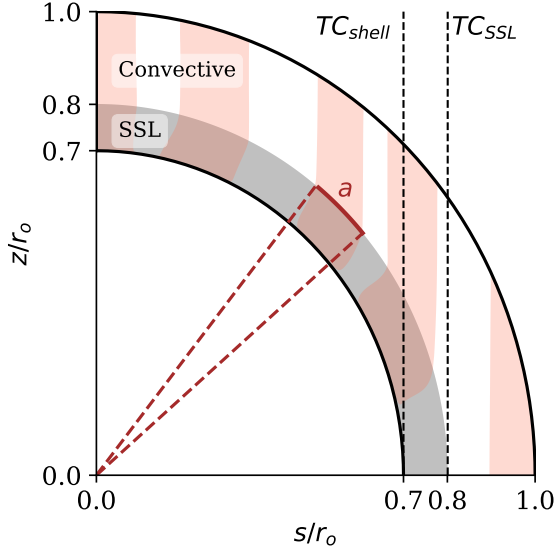


**Figure 2.1.** Schematic of simulated shell. The grey shaded region shows the stably stratified layer (SSL) with the convective region above. The pink stripes indicate a generic prograde/retrograde zonal flow structure with the width in arc-length ( $a$ ) at the SSL boundary marked for one jet. The tangent cylinders (TC's) associated with the SSL boundary and with the inner shell boundary are also shown by the black dashed lines.

$\epsilon_s A_s \ll 1$  for even the strongest stratification that we consider ( $A_s = 500$ ). This implies that the deviations of the reference state,  $\tilde{\rho}$  and  $\tilde{T}$ , from the adiabatic, polytropic solution are relatively minor.

### 2.2.3 Numerical Methods

The pseudo-spectral transform code MagIC 5.9 (available at <https://github.com/magic-sph/magic>) is used to solve equations 2.3-2.5, modified to incorporate the background states described by equations 2.9 and 2.10. They are solved by decomposing the mass flux into poloidal and toroidal potentials, implicitly ensuring the conservation of mass. These are then expanded in Chebychev polynomials, in radius  $r$ , and spherical harmonics in longitude  $\phi$  and latitude  $\theta$ . More details on the numerics can be found in W. et al. (2002); Gastine and Wicht (2012) or Schaeffer (2013), for example.

The numerical grid resolution is  $N_\phi \times N_\theta \times N_r = 1537 \times 768 \times 217$  and we use eight-fold symmetry in longitude. This assumption saves computational resources without compromising the main results. This is because firstly, the characteristic azimuthal wavenumber of the convection is much larger than eight. Secondly, much of the analysis is based on zonally averaged terms and, via comparison with a two-fold symmetry simulation, was shown to yield the same results.

### 2.2.4 Parameter values

In our simulations we set  $Ra = 10^9$ ,  $E = 10^{-5}$  and  $Pr = 0.5$ , which effectively scale to  $Ra = 1.975 \cdot 10^8$  and  $E = 2.25 \cdot 10^{-5}$  for the convective region.

As usual in such simulations, the choice of parameters is a compromise between the numerically feasible and the proximity to the relevant dynamical regime. Our Ekman number is small enough to render viscous forces fairly insignificant in the bulk of the fluid and the Rayleigh number is sufficiently super-critical to drive vigorous convection. The requirement to be in a rotation-dominated regime sets an upper limit for the Rayleigh number, for a fixed value of  $E$ . Here, a relevant parameter is the convective Rossby number, a measure of the ratio between buoyancy and Coriolis forces:

$$Ro_c = \sqrt{\frac{Ra}{Pr}} E. \quad (2.12)$$

In order to ensure that we are in a rotation-dominated regime we choose our parameters (eqs. 2.7) so that  $Ro_c < 1$  (we have  $Ro_c \sim 0.45$ ).

The ratio used to quantify the degree of stability of a stably stratified layer is  $N/\Omega$ , where  $N$  is the Brunt-Väisälä frequency and  $\Omega$  the rotation rate of the planet. This expresses the ratio of the restoring buoyancy force to the rotational forces. It is given by:

$$N/\Omega = \sqrt{\frac{Ra}{Pr} g(r) \frac{d\tilde{S}}{dr}} E = Ro_c \sqrt{g(r) \frac{d\tilde{S}}{dr}} \quad (2.13)$$

so in the deep SSL, where  $\frac{d\tilde{S}}{dr} = A_s$ , we have:

$$N/\Omega = Ro_c \sqrt{g(r_i) A_s}, \quad (2.14)$$

We also calculate local values  $(N/\Omega)_\ell$  by using gravity and entropy gradient at a given radius in eq. 2.13. Note that the gravity varies little across the SSL, so once the background entropy gradient reaches its maximum the ratio of  $N/\Omega$  becomes almost constant. In one parameter sweep we go from a fully convective case up to a ratio of  $N/\Omega = 14.286$ , keeping the Dissipation number fixed at  $Di = 1$ . This corresponds to a moderate variation of the background density across the whole shell by a factor of 5.9 and by 3.3 across the convecting region.

In addition to varying the amplitude of the stratification of the SSL we also vary the background density variation for a model with a moderately strong SSL ( $A_s = 25$ ,  $N/\Omega = 3.19$ ). This is done by varying the Dissipation number in steps of 0.25 (see Table 2.2). Our highest value of  $Di=2$  corresponds to a density contrast of 7. This is too small for a realistic model for the whole atmosphere of a gas planet but comes closer to the density contrast when ignoring the outermost few percent in radius.

In addition, we also carry out one purely convective simulation with aspect ratio 0.8 and stress-free boundary conditions at the inner shell boundary. This is done in order to compare the effect of an underlying SSL with a classical stress-free case. In this case, because of the reduced shell width the length-scale dependent parameters are adjusted accordingly to allow direct comparison.

$A_s$	$N/\Omega$	$(N/\Omega)_l$
-1	–	–
1	0.639	0.57
2.5	1.01	0.90
5	1.429	1.27
10	2.02	1.80
<b>25</b>	<b>3.194</b>	<b>2.85</b>
50	4.518	4.03
100	6.389	5.7
250	10.102	9.01
500	14.286	12.74

**Table 2.1.** The parameter range of  $A_s$  and the corresponding ratios of  $N/\Omega$  in the SSL and locally at  $r = r_s - \delta_s$ . The row in bold indicates the reference simulation which is at the centre of both parameter sweeps (see Table 2.2).

Di	$\tilde{\rho}_i/\tilde{\rho}_o$	$\tilde{\rho}(r_s)/\tilde{\rho}_o$
0.5	2.94	2.00
0.75	4.29	2.63
<b>1</b>	<b>5.90</b>	<b>3.35</b>
1.25	7.77	4.15
1.5	9.89	5.04
1.75	12.26	6.01
2	14.89	7.07

**Table 2.2.** The parameter range of Dissipation number,  $Di$  (see eq. 2.7), and the density ratios across the whole shell, in the second column, and across the convective later, in the third column. The degree of stratification is unchanged, with  $N/\Omega = 3.19$ .

## 2.3 Diagnostic Methods

### 2.3.1 Penetration Distance

One of the key diagnostic properties we investigate in this study is the penetration distance of the zonal winds into the SSL, which may be defined in several different ways.

Takehiro and Lister (2002) defined the penetration distance based on a local derivative of  $\bar{u}_\phi$  (where the overbar denotes an azimuthally averaged value) with respect to  $z$ , motivated by an assumed geostrophic extension of the flow into the stable layer. However, in our method we avoid making any assumption on the structure of the zonal winds.

We evaluate a penetration distance at a radius  $r_s - \delta_s$ , that is, slightly below the nominal boundary of the stable layer. Here, the local value of  $N/\Omega$  has nearly approached its maximum. We search for the local maxima and minima of the zonal flow,  $\bar{u}_\phi$ , as a function of  $\theta$  at two radii  $r_+$  and  $r_-$ , slightly above and below  $r_s - \delta_s$ , respectively, and denote them with  $\bar{u}_\phi^e$ . The penetration distance is then obtained as:

$$\delta(\bar{u}_\phi^e) = \left| \frac{\ln(\bar{u}_\phi^e(r_-)/\bar{u}_\phi^e(r_+))}{|r_+ - r_-|} \right|^{-1}, \quad (2.15)$$

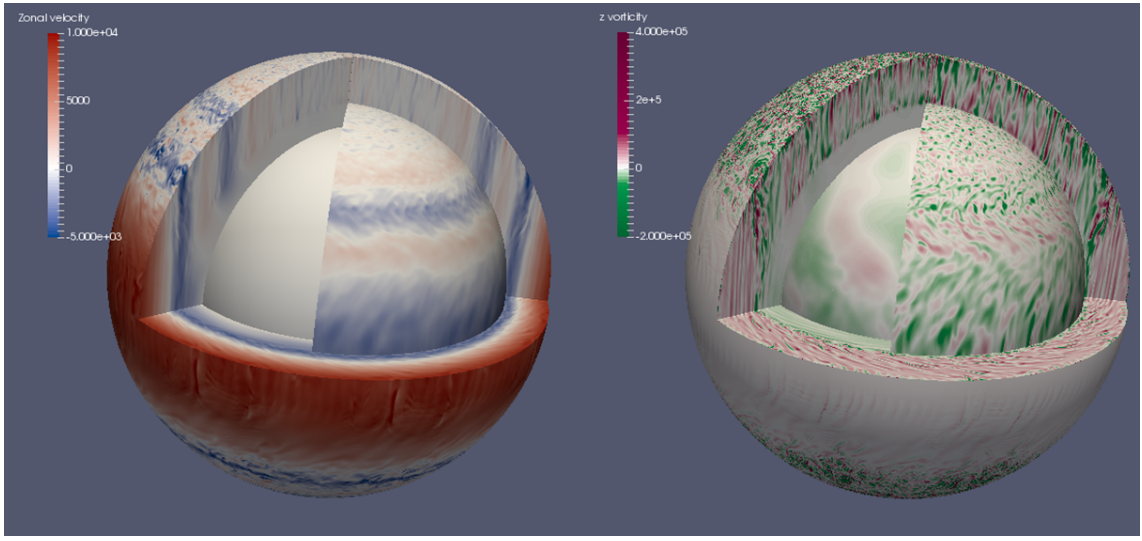


**Figure 2.2.** 3D renderings of snapshots of zonal flow,  $u_\phi$  (left) and  $z$  vorticity,  $\omega_z$  (right) for the canonical run highlighted in bold in Tables 2.1 and 2.2.

where the  $e$  indicates evaluation at the extrema.

The previous studies by Takehiro and Lister (2002) have found that for non-magnetic flows the penetration distance follows  $(N/\Omega)^{-1}L$  for weakly stratified stable layers. For penetrative convection the length-scale  $L$  is the characteristic length-scale of the convective eddies (Takehiro and Lister (2001), Dietrich and Wicht (2018), Gastine et al. (2020)). The few studies which have looked at the penetration of large-scale zonal flows have used either the width of the jets (i.e. along  $s$ , which assumes that the jets are geostrophic) or replaced  $L$  by a globally averaged arc-length (see Takehiro and Lister (2002), Takehiro and Sasaki (2018)). We find neither of these to be satisfying. The width, in  $s$ , of the jets is not appropriate on the SSL because of the breaking of geostrophy in this region. Furthermore, we see from Fig. 2.4 that the width of the jets varies dramatically with latitude. This leads us to our localised approach where we consider the penetration distance and width of each individual jet. As width we use the arc-length,  $a$ , as marked on Fig. 2.1. This is defined as the arc-length between the zero crossings of the  $\bar{u}_\phi$  profile on our chosen radial level,  $r = r_s - \delta_s$  (see Fig. 2.1).

### 2.3.2 Force Balance

In order to analyse what controls the zonal wind structure in the stably stratified region and in the transition zone to the convective layer, we explore the zonal force balance by considering the time-averaged (denoted by  $\langle \rangle$ ) axisymmetric, azimuthal component of the Navier-Stokes equation. In a statistically steady state, when integrating over a sufficiently

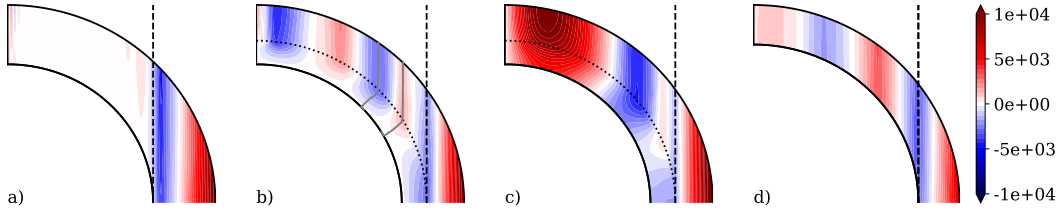


**Figure 2.3.** Azimuthally averaged zonal flow,  $\langle \bar{u}_\phi \rangle$ , averaged over time once quasi-steady state was reached. (a) and (d) are both fully convecting while (b) and (c) have an underlying stable layer with strong stratification  $N/\Omega = 14.3$ . (a) and (b) both have rigid lower boundary conditions. (c) and (d) have stress-free boundary conditions. The grey lines in (b) show the location of the  $\langle \bar{u}_\phi \rangle$  extrema for a retrograde and prograde jet.

long time interval, this is:

$$\begin{aligned}
 0 &= \langle \bar{F}_{AD} \rangle + \langle \bar{F}_C \rangle + \langle \bar{F}_R \rangle + \langle \bar{F}_v \rangle; \\
 \bar{F}_{AD} &= \frac{\bar{u}_s}{s} \partial_s(s\bar{u}_\phi) + \bar{u}_z \partial_z(\bar{u}_\phi) \\
 \bar{F}_C &= \frac{2}{E} \bar{u}_s \\
 \bar{F}_R &= \frac{1}{s^2 \tilde{\rho}} \partial_s \left[ \tilde{\rho} s^2 \bar{u}'_s \bar{u}'_\phi \right] + \frac{1}{\tilde{\rho}} \partial_z \left[ \tilde{\rho} \bar{u}'_z \bar{u}'_\phi \right] \\
 \bar{F}_v &= - \frac{1}{s^2 \tilde{\rho}} \partial_s \left[ \tilde{\rho} s^3 \partial_s \left( \frac{\bar{u}_\phi}{s} \right) \right] - \frac{1}{\tilde{\rho}} \partial_z \left[ \tilde{\rho} \partial_z (\bar{u}_\phi) \right], \tag{2.16}
 \end{aligned}$$

written here in cylindrical coordinates.  $\bar{F}_{AD}$  and  $\bar{F}_C$  are the advective force (so termed by Wicht and Christensen (2010)) and Coriolis force, respectively. The remaining terms are  $F_R$  and  $F_v$ ; the divergence of the momentum flux associated with Reynolds stresses, and the viscous force, respectively.

## 2.4 Results

### 2.4.1 The pattern and distribution of Zonal Winds

Fig. 2.2 shows 3D renderings of a snapshot of the zonal flows and  $z$  vorticity for the canonical run with  $N/\Omega = 5.90$  in the SSL and  $Di = 1$ . This gives a general impression of the jet structures; the alternating pattern observed on the surface and how this then extends downwards towards the SSL where the flows are then quenched. The rendering of  $\omega_z$  highlights the columnar structures formed in the rotation-dominated convective region, with the equatorial cut illustrating their slanted nature.

In Fig. 2.3 we compare the zonal wind structure of four simulations with and without a stable layer and different mechanical conditions at the inner boundary. Without a stable layer and with a rigid lower boundary (Fig. 2.3a), the sole jet pair is confined to the region outside the tangent cylinder (TC). Inside the TC, jet formation is suppressed by viscous

friction at the rigid boundary, as previously found in similar numerical models.

The presence of a strongly stratified stable layer seems to decouple the overlying convective region from a rigid lower boundary and allows for the development of strong alternating zonal jets also inside the TC (Fig. 2.3b). In this case the jet structure in the convective part of the shell is similar to the one obtained when the stable layer is removed and replaced by a free-slip condition at the bottom of the convecting region (Fig. 2.3d). In both cases the jet pattern is constrained by the geometry of the convective shell alone (Heimpel and Aurnou 2007), i.e., the TC to the SSL boundary now replaces the "classical" TC imposed at the inner shell boundary, as seen in Fig. 2.3b.

A very similar type of jet structure is formed when comparing Fig. 2.3b with Fig. 2.3c (the case with a SSL and stress-free boundary conditions below). The main difference is in the SSL as the winds can now penetrate a little deeper as they can reach the bottom boundary. However, the jet velocity still decreases with depth, in contrast to the case without a stable layer and a stress-free lower boundary (Fig. 2.3d).

The ratio of convective versus zonal Reynolds numbers, calculated from the non-axisymmetric poloidal and toroidal energies and the axisymmetric toroidal energy, is over 3 for cases (a) and (b) and over 5 for cases (c) and (d). This illustrates that in all four cases zonal flows dominate the dynamics but are not as prominent as on Jupiter.

The reason for the presence or absence of zonal jets inside the TC in the four cases shown in Fig. 2.3 can be understood as follows. The zonal winds are driven by comparatively weak Reynolds stresses. In the absence of electromagnetic forces they are opposed by viscous stresses due to velocity gradients (further explored in Section 2.4.3). In case of free-slip boundaries, the viscous force is of the order  $v\bar{u}_\phi/d_s^2$ , where  $d_s$  is the characteristic width of jets in s-direction. Because  $d_s$  is large, in non-dimensional terms of order one, viscous stresses are also weak. In case of a rigid lower boundary,  $d_s$  must be replaced by the thickness of the viscous Ekman layer, which is of order  $E^{-1/2}$ . For the value of E in our simulations this is about 1/300, hence, for the same value of  $\bar{u}_\phi$  the viscous stress would be larger by a factor 300, which effectively precludes the development of geostrophic jets in regions where they would come into contact with the rigid lower boundary. When a stable layer is present, the wind velocity decreases gradually and continuously throughout this layer towards the lower boundary. The stable stratification inhibits radial flows so effectively, that Ekman pumping is impossible, thereby preventing the formation of an Ekman layer at the lower boundary.

The degree of stratification has an influence on the number and amplitude of the zonal winds inside the tangent cylinder (see Fig. 2.4). For lower values of  $N/\Omega$  they are limited to mid-latitudes while for higher values they reach all the way to the poles. With increasing stratification they also gain in strength.

In our particular regime we observe that the position of the first retrograde jets that flank the equatorial jet is perfectly aligned with the TC; in the simulations with a SSL it is the TC associated with the SSL boundary. If this were a general rule, the observed latitudes of these jets at the surface of the gas planets would indicate the tangent cylinder locations. I.e. the depth at which there is a transition to a dynamo region or, as in our case, a SSL. Gastine and Wicht (2012) generally find the same location except in simulations where the retrograde (and higher latitude) jets are not well developed for higher  $Ra$ , or those with high density contrasts across the shell. Therefore, we merely remark upon it and conclude that it may either be a characteristic associated with being in a rotation dominated regime

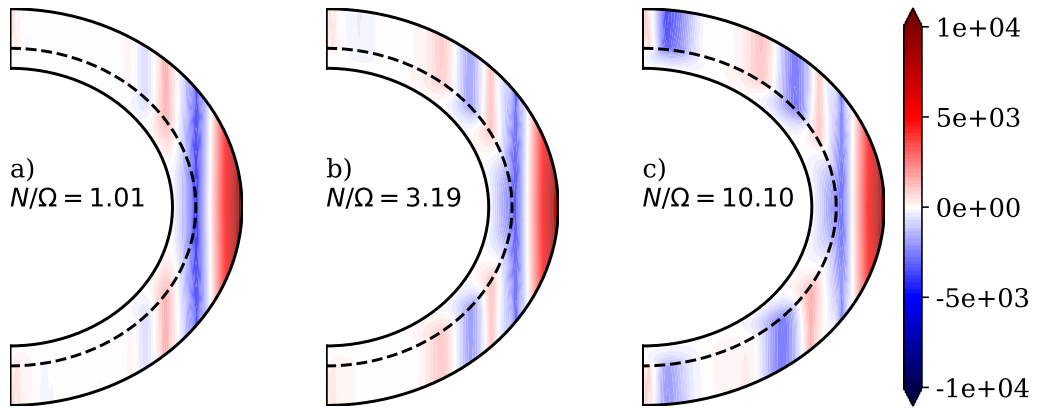


**Figure 2.4.** Azimuthally and temporally averaged zonal flow,  $\langle \bar{u}_\phi \rangle$ , for a range of simulations with varying  $N/\Omega$ , all with  $Di = 1$  (see Table 2.1).

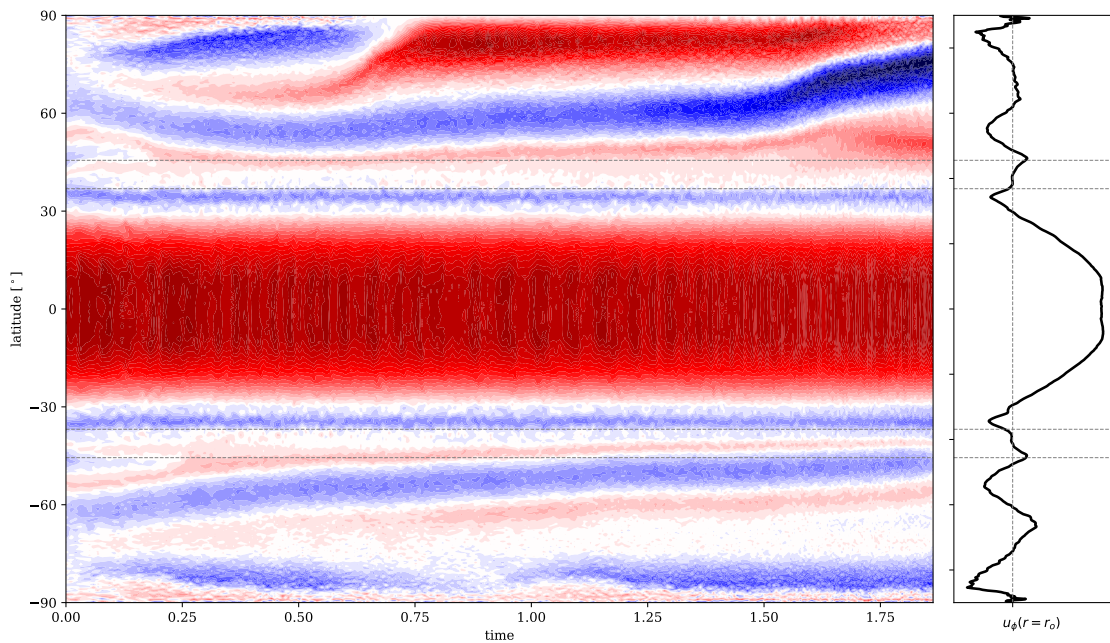


**Figure 2.5.** Azimuthally averaged surface zonal flow  $\bar{u}_\phi(r = r_o)$  for the simulation with  $N/\Omega = 14.3$  in the SSL, as a function viscous diffusion time. The two TC's, associated with the shell and with the SSL boundary, are indicated by the grey dashed lines. Red (blue) indicates prograde (retrograde) flow. The grey shaded area indicates the time over which the temporally averaged force balance analysis in Section 2.4.3 was analysed with the corresponding flow profile shown on the right.

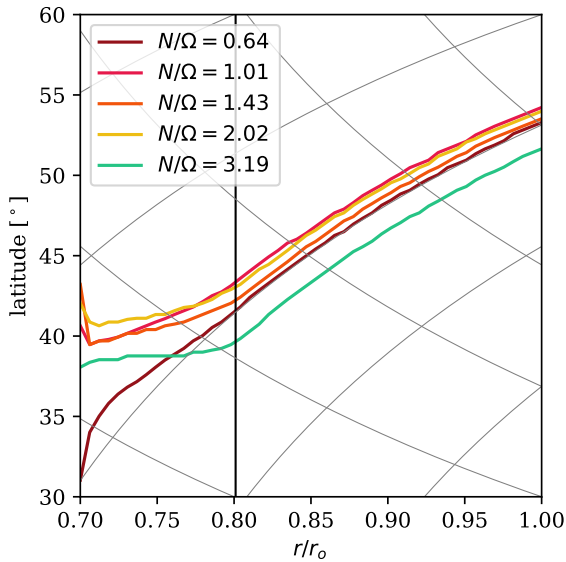


**Figure 2.6.** Location of the peak of the retrograde indicated in Fig. 2.3b with depth for different  $N/\Omega$ , indicated by line colour. The background grid indicates lines of constant  $s$  and  $z$ . The location of the SSL boundary is marked on at  $r = 0.8r_o$ .

( $Ro_c \approx 0.45$ ) or being highly super-critical. Verifying this would require further studies including the variation of parameters which we have chosen to keep constant.

The simulations which have jets at latitudes  $|\lambda| \gtrsim 45^\circ$ , observed when  $N/\Omega \gtrsim 6.4$ , vary with time, as illustrated by Fig. 2.5. A similar jet structure is maintained for around 0.2 viscous diffusion times before jets merge or split and a slightly different structure is sustained for a similar time. This also leads to a considerable degree of equatorial antisymmetry for these cases as the two hemispheres evolve independently. This is only observed inside the TC associated with the SSL boundary. Furthermore, the jets do not migrate consistently in the same direction, i.e. pole-wards or equator-wards. This is unlike the merging/splitting observed in the experimental work carried out by Lemasquerier et al. (2021), which had a clear bistable nature and a distinct transition between the two steady states, happening on shorter time scales than in our simulations. Jet migration was also observed and investigated by Chemke and Kaspi (2015) but here this was a very periodic and predictable phenomenon. What we observe has a much more random nature. Now considering the structure of the zonal flows with depth, while it is  $z$ -invariant in the convecting region, this changes upon entering the SSL (see Fig. 2.3b). In the stable layer the geostrophy is broken and the winds extend with decreasing amplitude in a radially downward direction. This is illustrated in Fig. 2.6 where the latitude of the peak of the first retrograde jet within the TC is shown as a function of radius. We observe that with a weakly stratified layer, eg. for  $N/\Omega = 0.639$ , the jet remains almost perfectly geostrophic, i.e. it is hardly deflected from a line of constant  $s$  (indicated by the grey grid-lines). With increasing  $N/\Omega$  we see that the jet location veers increasingly more off this track and into a radial direction, until around  $N/\Omega = 6.39$  (and values above this in our study, not plotted) where almost perfect latitudinal invariance is reached in the SSL.

This change in direction has not been found in the previous simulations by Takehiro and

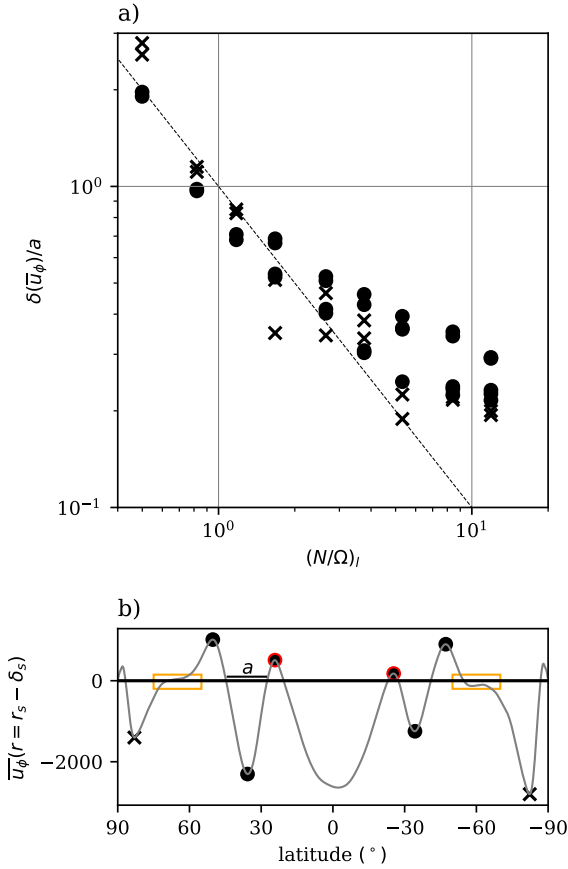


**Figure 2.7.** Ratio of individual jet's penetration distances,  $\delta(\bar{u}_\phi)$ , to their width in arc-length,  $a$ , as a function of local  $(N/\Omega)$ . The dotted line indicates  $\delta(\bar{u}_\phi)/a \propto (N/\Omega)^{-1}$ . b) an illustration of how the data points were evaluated.

Lister (2002) for zonal flows driven by deep convection and penetrating into an overlying stable layer. In their set-up very few jets form and their structure seems to remain z-invariant.

## 2.4.2 Zonal wind penetration distance

In Fig. 2.7a we plot the ratio of the penetration distance  $\delta(\bar{u}_\phi)$ , as found according to eq. 2.15, to the arc-length  $a$  for each individual jet as a function of the (local)  $(N/\Omega)_l$ , given by eq. 2.13. The division by the arc-length collapses the data points to some degree for a given value of  $N/\Omega$ . However, some scatter remains that in some cases reaches a factor of two. At least part of the scatter may be explained by the difficulty of defining  $a$ . This is illustrated in Fig. 2.7b; the zonal wind profile as a function of latitude on  $r = r_s - \delta_s$  for one particular case. We find that some jets are well developed at this radius and have clearly defined boundaries to their neighbours, whereas for others this is not the case. Firstly, we note that some jets which are clearly prograde (retrograde) at the surface are so diminished in amplitude at this depth, especially when flanked by strong retrograde (pro-

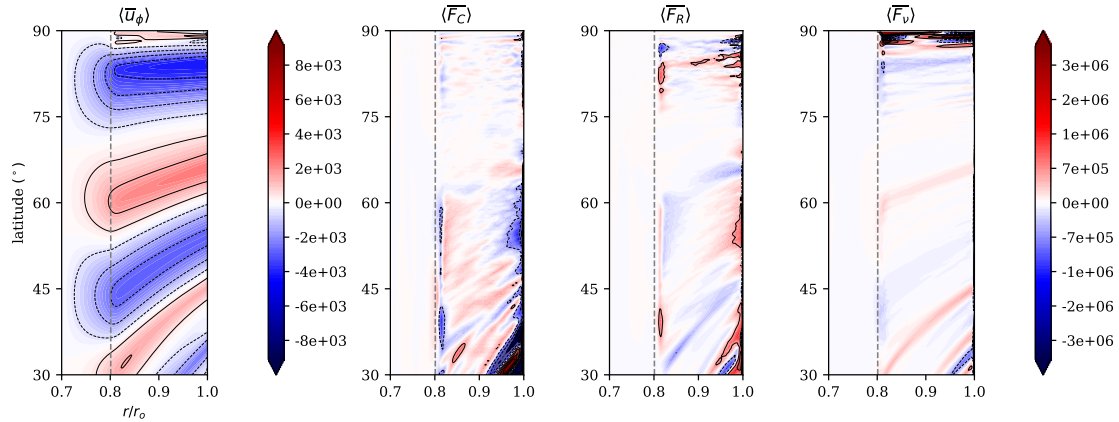


**Figure 2.8.** 2D plots of the terms in eq.2.16 for the simulation where  $N/\Omega = 14.29$  in the SSL and  $Di = 1.0$ . The dashed grey line indicates  $r_s$  ( $\sim 0.8r_o$ ), the mid-point of the  $d\tilde{S}/dr$  jump.

grade) jets, that calculating their local penetration distance becomes difficult. Two such examples are indicated by red circles around the markers which pinpoint the location of the local maxima in Fig. 2.7b. We therefore exclude all jets with amplitudes  $< 20\%$  of that of the strongest jet in Fig. 2.7a.

Secondly, we observe that the boundary between neighbouring jets is sometimes not sharp. Two such examples are highlighted by the orange boxes in Fig. 2.7b. This makes it more difficult to define the appropriate arc-length associated with the jet(s) in question, as the usual method of finding the distance between the points where  $\bar{u}_\phi = 0$  may yield misleading values. This is most commonly found for the jets closest to the poles, which we have marked these jets with a cross in both plots in Fig. 2.7.

In simulations without strong jets close to the poles, the northernmost/southernmost jets typically have a skewed shape in their  $\bar{u}_\phi$ -profiles with a rather slow decay of  $\bar{u}_\phi$  towards their poles. This also leads to large values of  $a$  which may be unrealistic. The jets closest to the poles often represent outliers in Fig. 2.7a. If we concentrate only on the others (filled circles in Fig. 2.7) the spread at a given  $N/\Omega$  shrinks to values that are less than a factor 1.6.

For the strongly stratified case we also checked the penetration distances of the jets at different points during its time evolution and the points fall around the same values as those plotted here. Therefore the relation does not seem to be affected by how long the jets remain in their locations.

In contrast to the results of Takehiro and Lister (2002), we find a clear dependence of the penetration distance on  $N/\Omega$ . For low values  $N/\Omega \lesssim 1$  it is roughly proportional to  $(N/\Omega)^{-1}$ . At larger values it progressively levels off. We can only guess the  $\delta(\bar{u}_\phi)$  could become independent of  $N/\Omega$  for  $N/\Omega \gtrsim 10$ .

### 2.4.3 Force Balance

In this section we consider the azimuthally averaged forces that act in  $\phi$ -direction in order to identify the regions that contribute most to the driving of the jets and to understand the change from geostrophic to radial jet structure in the SSL. Fig. 2.8 shows the balance introduced in section 2.3.2 for the simulation with the most strongly stratified stable layer ( $N/\Omega = 14.29$ ), calculated for the time interval indicated in Fig. 2.5 (around 0.05 viscous diffusion times), during which the jets are fairly steady. This time interval was chosen because the jet structure is more Jupiter-like, than in the later epoch where a prograde polar jet develops.

Fig. 2.8 shows 2D plots with latitude on the y-axis and normalised radius on the x-axis, focusing on one hemisphere at mid- to high-latitudes. The choice of axes helps to highlight the  $\theta$ -invariance of the decaying winds upon entering the SSL (left panel). We do not show the advective force as this has a negligible contribution relative to the other terms.

We find that the Reynolds stresses that drive the zonal flow are concentrated near the boundaries of the convective region. By integrating the terms over  $z$ , we confirm that the characteristic balance of the Reynolds stresses associated with the correlations of  $u'_s$  and  $u'_\phi$  and the viscous force (eg. Gastine and Wicht (2012)), given by:

$$\int_z \tilde{\rho} s \partial_s (\bar{u}_\phi / s) dz = \int_z \tilde{\rho} \bar{u}'_s \bar{u}'_\phi dz \quad (2.17)$$

holds over the convective region.

As the bottom of the convective region is reached, there are large contributions from  $\bar{F}_R$  as  $u'_r$  flows are quickly quenched. The coriolis force is proportional to the meridional circulation component away from the rotation axis. Since this is also effectively quenched by the stratification, the viscous force, being the only remaining force in our time-averaged force balance, must also decrease accordingly. This allows us to understand why the zonal jets obtain their spherical geometry in the stable layer as it implies a diffusive continuation of the jets into the SSL, where the wind velocity at the stable layer boundary can be considered as a boundary condition. As this boundary is spherical the extension of the winds into the SSL is predominantly in the radial direction.

The breaking of geostrophy in the SSL must be caused by thermal wind effects. By considering the azimuthal component of the curl of the momentum equation (eq. 2.3)  $\frac{2}{E} \partial_z (\bar{u}_\phi) \simeq \frac{Ra g}{Pr r} \partial_\theta (S')$  (neglecting viscous and inertial forces), we note that a latitudinal variation in the entropy must balance the non-geostrophic variation of the flow in  $z$ -direction. As described in Christensen et al. (2020), this entropy perturbation is created by radial advection of  $\tilde{S}$  by a meridional flow that grazes the top of the stable layer. From here the entropy perturbation propagates diffusively downward into the SSL.

### 2.4.4 Varying the Background Density Profile

Varying Dissipation number  $Di$ , i.e. the density contrast across the shell, has an effect on the number and distribution of jets. A lower density gradient (closer to Boussinesq) produces a greater number of zonal jets, reaching all the way to higher latitudes (see Fig. 2.9). When the density contrast across the shell is increased, we still find jets inside the tangent cylinder, but they are now restricted to mid-latitudes. Given that on Jupiter

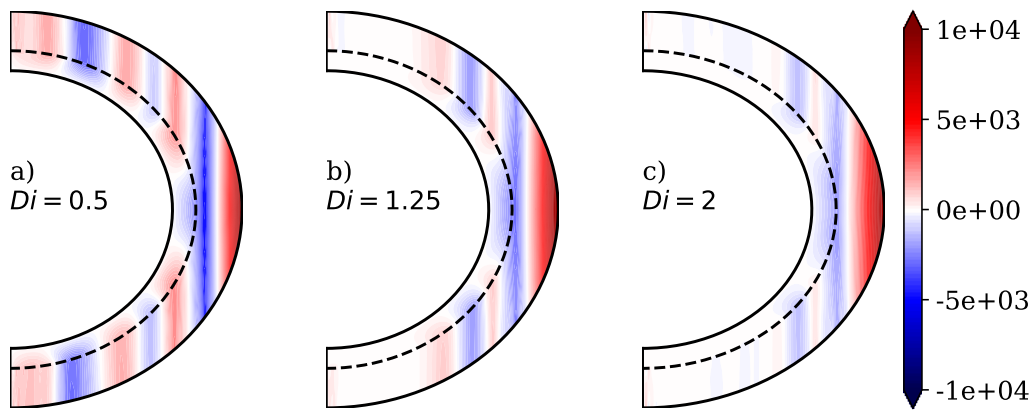


**Figure 2.9.** Azimuthally and temporally averaged zonal flow,  $\bar{u}_\phi$ , for a range of simulations with different background density profiles, all with  $N/\Omega = 3.19$  (see Table 2.2).

and Saturn, where high-latitude jets are observed, the density contrast in the outer regions is more drastic than in our models, this trend may pose a problem for simulations with moderate density contrasts.

However, with increasing density variation, the critical Rayleigh number increases (Jones et al. (2009), Gastine and Wicht (2012)). Therefore, as we carry out our parameter sweep with a constant  $Ra$ , the simulations with smaller  $Di$  are more super-critical than those with higher  $Di$ . Potentially, the strength and distribution of jets might be more affected by the differences in super-criticality than by the density gradient. From the work of Gastine and Wicht (2012) we estimate that the  $Di = 0.5$  simulation may be around twice as super-critical as the  $Di = 2$  simulation. Therefore, in order to test if and how much impact this has, we carry out one additional simulation at  $Di = 0.5$  where we reduce the Rayleigh number by a factor of two ( $Ra = 5 \cdot 10^8$ ) so that now the degree of super-criticality is approximately the same as in the simulation with  $Di = 2$ ,  $Ra = 10^9$ . In order to ensure that the ratio of  $N/\Omega$  in the SSL is the same we double  $A_s$  to 50. The time-averaged surface zonal velocity profile of this simulation is compared with the original simulation from the parameter sweep, shown in Fig. 2.10. The two simulations have very similar typical convective Reynolds numbers (both are around 500).

The velocity of the equatorial jet is reduced by about 10% upon lowering the Rayleigh number. To highlight the difference between the jets inside the tangent cylinder and the equatorial jet, the velocity is normalised by the respective equatorial value in Fig. 2.10. At the lower Rayleigh number the relative velocity of jets inside the TC is generally diminished. In particular, jets pole-ward of  $\pm 60^\circ$  latitude become very weak at the lower value of the Rayleigh number but are still significant at the higher value. In conclusion, the waning of high-latitude jets upon increasing the density gradient for a fixed value of  $Ra$  is at least partially caused by the diminishing degree of super-criticality.

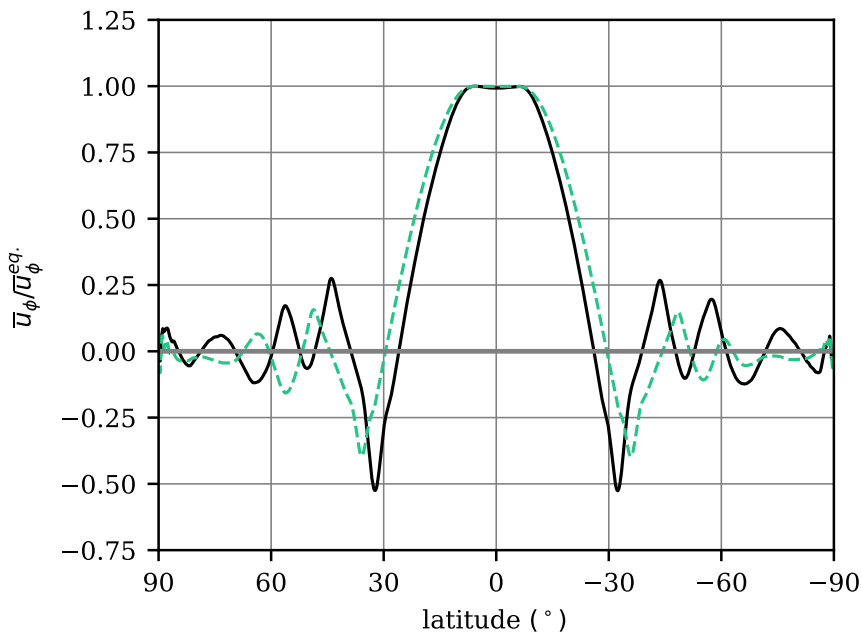


**Figure 2.10.** Time averaged surface zonal flow profiles of the original simulation with  $Di = 0.5$ ,  $Ra = 10^9$  (solid black), and of the simulation with  $Di = 0.5$ ,  $Ra = 5 \cdot 10^8$  and  $A_s$  doubled to 50, to match the value of  $N/\Omega$  in the stable layer (dashed green). Both profiles have been normalised by  $\bar{u}_\phi^{eq}$ , their equatorial jet amplitudes.

## 2.5 Discussion and Conclusions

We find that a strongly stratified stable layer may act to decouple zonal flows from resistive effects at a lower boundary that may otherwise impede zonal flows inside the tangent cylinder (TC) (Jones and Kuzanyan 2009). The width of the equatorial jet is now determined by the location of the TC associated with the boundary to the stably stratified layer (SSL), as opposed to the inner shell boundary, and strong multiple jets emerge within this TC. The SSL seems to protect the zonal winds in the convective region from feeling the viscous friction at the lower boundary directly. The stable layer will also help to decouple the zonal jets developing in a low-electrical-conductivity region from the Maxwell stresses exerted at depth where the conductivity has increased to significant values.

Takehiro and Lister (2002) find that for the penetration distance of zonal flows, viscous diffusion effects dominate. As a consequence, the penetration depth is independent of the degree of stratification and only determined by the width of a zonal jet. However, we observe that especially for weakly stratified stable layers, there is still a significant dependence on the degree of stratification. The differences may be explained by the fact that Takehiro and Lister (2002) studied the penetration of jets into an overlying stable region with a free-slip top boundary while we consider the penetration into a layer with no-slip lower boundary conditions. Since the thickness of our SSL is comparable to the jet width, the lower boundary condition may still affect the penetration.

However, we do observe in that viscosity plays a crucial role in constraining how zonal winds extend in the SSL. Examining the azimuthal forces reveals that already at a short

distance below the stable layer boundary the Reynolds stresses and the Coriolis force become insignificant, which leaves the very small viscous drag to determine the force balance. This leads to the jets extending predominantly in the radial direction into the stable layer and also helps us to explain why the penetration depth depends on the arc-length of the jets rather than on the width in  $s$ -direction.

Our simulations have been performed for a rather weak depth-dependence of the background density as compared to the actual variation in the outer layers of the gas planets. Varying this density contrast, we find that for the same value of the Rayleigh number jets tend to become weaker and disappear at high latitudes. This at least to some part due to the decreasing super-criticality of convection when the density contrast becomes larger. It remains to be explored if only a sufficient degree of super-criticality is needed to ensure the existence of high-latitude jets in the gas planets with their strong density contrast in their non-conducting outer regions, or if some other effects also play a role.

Gastine and Wicht (2012) also explore the impact of an increasing background gradient on the jet structure, exploring more extreme values than we could afford. Comparing simulations at the same level of super-criticality, they report that the amplitude of the higher latitude jets decreases with increasing density gradient. Using an aspect ratio of 0.6, only one prograde jet developed inside the TC in their simulations. Gastine et al. (2014) show that multiple strong jets inside the TC are indeed possible for strong background density gradients, a stress-free lower boundary and an aspect ratio of 0.85 when Ekman and Rayleigh numbers are chosen accordingly.

When trying to explain Jupiter's off gravity harmonics with the zonal winds, it is typically assumed that their structure remains (roughly) constant on cylinders. However, our simulations suggest that their decay at depth goes along with a transition from cylindrical to latitudinal invariance of the jet structure. It would be interesting to explore the possible consequences for the gravity moments. In a similar vein, the assumption of the same attenuation function for all jets irrespective of their width in the gravity study is also questionable, since the penetration distance into a stable layer is proportional to their latitudinal width. The jets observed on both planets' surfaces vary considerably in latitude and have very different length-scales if projected onto a SSL boundary at a specific depth. Our non-magnetic simulations do not fully capture the physical processes that are essential for controlling the latitudinal and radial distribution of zonal winds in the gas planets. At depths where the electrical conductivity becomes significant, magnetohydrodynamic effects will play a role. However, while Christensen et al. (2020) and Gastine and Wicht (2021) find that both a SSL and magnetic effects are essential for damping the winds at depth, our results suggest that a very strongly stratified layer, with a ratio of  $N/\Omega \gtrsim 4$ , would also be sufficient. A systematic study of their combined influence on jets driven by convection in the planets' atmospheric layers could further clarify the roles they play in the flow dynamics of Jupiter.



# 3 The Effects of a Stably Stratified Region with radially varying Electrical Conductivity on the Formation of Zonal Winds on Gas Planets

## *Abstract*

The outer areas of Jupiter and Saturn have multiple zonal winds, reaching the high latitudes, that penetrate deep into the planets' interiors, as suggested by gravity measurements. These characteristics are finally replicable in numerical simulations by including both a shallow stably stratified layer, below a convecting envelope, and increasing electrical conductivity. A dipolar magnetic field, assumed to be generated by a dynamo below our model, is imposed. We find that the winds' depth into the stratified layer depends on the local product of the squared magnetic field strength and electrical conductivity. The key for the drop-off of the zonal winds is a meridional circulation which perturbs the density structure in the stable layer. In the stable region its dynamics is governed by a balance between Coriolis and electromagnetic forces. Our models suggest that a stable layer extending into weakly conducting regions could account for the observed deep zonal wind structures.

## 3.1 Introduction

Zonal winds are alternately westwards/eastwards flows and feature across all four outer planets in our solar system. Those observed on the gas giants, Jupiter and Saturn, share some key characteristics. The dominating equatorial prograde flow on Jupiter (Saturn)

---

The contents of this chapter has been reproduced from the article: [P. N. Wulff](#), U. R. Christensen, W. Dietrich, J. Wicht. *The Effects of a Stably Stratified Region with radially varying Electrical Conductivity on the Formation of Zonal Winds on Gas Planets*, submitted to Journal of Geophysical Research: Planets (2023)

**Contribution:** I ran all of the simulations, performed analyses and wrote the first draft of the paper. After thorough revisions, much of the original content and structure is preserved. U. R. Christensen established the main research aims and approach, driven by analytical predictions. J. Wicht helped to implement the magnetic inner boundary condition in the MagIC code. All three co-authors contributed to writing the final draft, physical interpretations of the results and research supervision.

spans roughly  $30^\circ$  ( $60^\circ$ ) with an amplitude of around 100 m/s (400 m/s). This is flanked by a pair of slightly weaker retrograde jets and multiple jets reaching the high-latitude regions (Tollefson et al. 2017, García-Melendo et al. 2011). While these winds are weaker, they are still significantly stronger in amplitude than non-zonal flows. Jupiter's northern hemisphere also features an unusual prograde jet, as strong as the equatorial jet, at around  $21^\circ$  latitude, introducing a strong equatorial antisymmetry into the dynamics.

Surface measurements, first from Voyager 1 and 2 (Ingersoll et al. 1981) then from Cassini (Salyk et al. 2006), have shown a strong correlation between the eddy momentum flux (or Reynolds stresses) and the zonal wind speed as a function of latitude. This confirms current theories that Reynolds stresses, which are statistical correlations of the components of the flow at small and intermediate scales, drive the zonal winds.

The extent of the winds into the jovian interior has recently been constrained using the gravity moment measurements from Juno, yielding a depth between 2,500 – 3,000km; around 96% of the planet's radius (Kaspi et al. 2018, Dietrich et al. 2021, Galanti et al. 2021). The same investigation has also been carried out for Saturn, using the Cassini measurements, suggesting the winds extend to 8,000 – 9,000km depth, around 85% of the planetary radius (Galanti et al. 2019).

This is consistent with simulation-based studies where it has been found that the location of the flanking retrograde jets is usually coincident with the ‘tangent cylinder’, here loosely defined as the cylinder aligned with the axis of rotation with a radius corresponding to the depth at which jet quenching takes place. This has been found in numerical models studying both magnetic effects as a potential braking mechanism for the winds, with increasing electrical conductivity at depth (eg. Duarte et al. (2013)) or transition into a stably stratified region Wulff et al. (2022). Therefore, based on these basic geometric observations of the dynamics we would expect the winds to penetrate deeper on Saturn, with its much wider equatorial jet.

A strong prograde jet flanked by two retrograde jets in the equatorial region, outside the tangent cylinder, were already reproduced in hydrodynamic simulations (Christensen 2002, Heimpel et al. 2005, Gastine et al. 2014). However, simulations with rigid lower boundary conditions did not exhibit any zonal winds inside the tangent cylinder. Models with stress-free inner boundaries featured some high-latitude jets but failed to provide any insights into the winds’ damping mechanism in the interior.

In both planets the increasing electrical conductivity at depth (e.g. French et al. (2012)), plays a crucial role in the zonal winds’ downward propagation from the surface. It has been speculated that deeply penetrating zonal winds may cause the observed secular variation (Moore et al. 2019). However, Bloxham et al. (2022) argue that a slight correction of Jupiter’s rotation rate provides a better explanation, in combination with deeper flows in the dynamo region. Furthermore, considering reasonable limits for the total ohmic dissipation suggests that the winds may not penetrate into the highly conducting region of Jupiter (Liu et al. 2008, Wicht et al. 2019, Cao and Stevenson 2017). It was originally surmised that Lorentz forces, acting where the deep zonal flows reach the conducting region, were responsible for the braking of the winds. However, simulation-based studies such as Dietrich and Jones (2018) found that these Maxwell stresses at depth eradicate all large scale zonal flow above the conducting region, leading to zonal wind profiles with the strong flows confined to near the equator.

Christensen et al. (2020) suggested that a combination of a stably stratified layer (SSL)

and the magnetic effects at depth are responsible for the breaking of the zonal flows on Jupiter. They suggest that the winds decrease in the stable layer in accord with a thermal wind balance. The required density perturbation is caused by a meridional circulation which is affected by electromagnetic forces. Duer et al. (2021) present observational evidence for the existence of meridional flow associated with the winds. Gastine and Wicht (2021) conducted a global dynamo simulation with a strong radial variation of conductivity, which was successful in producing winds formed and being maintained above the highly electrically conducting region. Recently, Moore et al. (2022) also showed that dynamo simulations of Jupiter including a SSL at 90 – 95% radius produced dynamos with a dominant axial dipole component and a similar degree of complexity as the measured Jovian magnetic field.

In the context of Saturn a stable layer, shallower than the region of metallic conductivity, could help to explain both the formation of its high-latitude zonal winds and how they are quenched at depth, and its magnetic field. This is remarkably axisymmetric (Dougherty et al. 2018) and a stable layer at the top of its semi-conducting region would provide a skin-effect, reducing the smaller-scale field components (suggested by Stevenson (1979) and studied by Christensen and Wicht (2008), Stanley and Mohammadi (2008), Stanley (2010)). Furthermore, the difference in amplitude of its axial dipole field compared to the higher degree  $m = 0$  components (Cao et al. 2020) indicates that there may be both a deeper dynamo region generating the strong dipole field, located between a dilute core and the helium rain layer, as well as a shallower layer adding the weaker latitudinally banded perturbations, operating between the helium rain region and a shallower, thin, stable layer.

However, for both planets the main uncertainty in the hypothesis is the origin, location, depth and strength of such a relatively shallow stable layer. A helium rain layer (Stevenson and Salpeter 1977), providing a potential source of compositional stratification, is predicted to lie deeper than the extent of the zonal winds. In Jupiter, although there are some uncertainties concerning the H/He phase diagram, this would be below 86% radius based on *ab initio* EoS calculations of high-pressure experiments (Hubbard and Militzer 2016, Lorenzen et al. 2011, Brygoo et al. 2021). In Saturn helium immiscibility may occur at around 65% radius, e.g. Morales et al. (2013). In both planets, however, there is not only a large uncertainty with regards to the depth of a helium rain layer but also no good estimate for its vertical extent. For the case of Jupiter the shallower regions, above where a helium rain layer is thought to reside, are potentially also more complex, based on the accurate gravity measurements from Juno, which suggests the existence of a shallow stably stratified region (Debras and Chabrier 2019, Nettelmann et al. 2021, Debras et al. 2021), providing a potential link with the stable region associated with a quenching of the zonal winds.

In Wulff et al. (2022) we used purely hydrodynamic convection models to investigate the relationship between the degree of stratification of such a layer and the penetration of the winds, formed in the overlying convecting envelope, into the stable region below. We found that when the degree of stratification is strong, zonal flows form all the way to the higher latitudes, as is observed on both gas giants, even when imposing a no-slip boundary condition at the bottom of the stable layer. Furthermore, when encountering the SSL, the winds are quenched and geostrophy (i.e. their invariance with respect to the axis of rotation) is broken. However, the decay of the jet amplitude in this hydrodynamic study

was still too gradual with depth to fit secular variation data. Furthermore, we expect that at sufficient depth the electrical conductivity will be large enough for magnetic effects to play a role. Therefore, it is crucial to investigate how this will influence both the damping of the jets in the SSL as well as their strength and latitudinal distribution in the overlying convective region. In our study we also test the concept of Christensen et al. (2020). In their simplified models the zonal flow was driven by an imposed ad-hoc force. In our models the zonal winds are driven self-consistently by the convective eddies, which implies that a potential feedback of the winds on the eddy dynamics is also accounted for.

## 3.2 Methods

We simulate thermal convection in a spherical shell rotating with angular velocity  $\Omega \cdot \hat{\mathbf{e}}_z$ . The ratio of inner boundary radius,  $r_i$ , to outer radius,  $r_o$ , is 0.7. Only the upper part of the shell above  $0.83r_o$  is convectively unstable, whereas the lower part is stably stratified (described in detail in Section 3.2.3). We assume an exponentially varying electrical conductivity rising from a negligible value at  $r_o$  to a moderate value at  $r_i$  (see Section 3.2.4). We impose an axisymmetric dipolar magnetic field aligned with the rotation axis through a boundary condition at  $r_i$ , which represents a field generated by a dynamo operating below  $r_i$ . For our systematic study we use the Boussinesq approximation (i.e. incompressible flow), although we also perform additional simulations with the anelastic approximation (where a radially varying background density is prescribed). The Boussinesq simulations are cheaper computationally and allow a wider parameter study. In this study, we keep all hydrodynamic parameters as well as the degree of stability in the SSL at fixed values, but we vary the magnetic field strength and the profile of the electrical conductivity. The anelastic simulations are carried out for a subset of these parameters in order to confirm that the trends observed also hold in the compressible models.

### 3.2.1 MHD Equations

As our primary analysis focuses on simulations that use the Boussinesq approximation, we give the governing magneto-hydrodynamic (MHD) equations here in their incompressible form (see Wulff et al. (2022) for the hydrodynamic equations under the anelastic approximation). The key features we incorporate are the radially varying magnetic diffusivity  $\lambda(r)$  and  $dT_c/dr$ , the imposed stratification profile, where  $T_c$  is the background temperature. As we use a constant gravity,  $g$ , the equations then simplify to:

$$\frac{\partial \mathbf{u}}{\partial t} + (\mathbf{u} \cdot \nabla) \mathbf{u} + \frac{2}{E} \hat{\mathbf{e}}_z \times \mathbf{u} = -\nabla p + \frac{Ra}{Pr} \vartheta \hat{\mathbf{e}}_r + \frac{1}{EPm} (\nabla \times \mathbf{B}) \times \mathbf{B} + \nabla^2 \mathbf{u}, \quad (3.1)$$

$$\frac{\partial \mathbf{B}}{\partial t} = \nabla \times (\mathbf{u} \times \mathbf{B}) - \frac{1}{Pm} \nabla \times (\lambda(r) \nabla \times \mathbf{B}), \quad (3.2)$$

$$\frac{\partial \vartheta}{\partial t} + (\mathbf{u} \cdot \nabla) \vartheta + u_r \frac{dT_c}{dr} = \frac{1}{Pr} \nabla^2 \vartheta, \quad (3.3)$$

$$\nabla \cdot \mathbf{u} = 0, \quad (3.4)$$

$$\nabla \cdot \mathbf{B} = 0, \quad (3.5)$$

where  $\mathbf{u}$  is the velocity field,  $\mathbf{B}$  is the magnetic field, and  $p$  is pressure. Temperature fluctuations  $\vartheta$  are defined with respect to the hydrostatic reference state. We adopt a dimensionless formulation where the reference length scale is the shell thickness  $d = r_o - r_i$ , where  $i$  denotes the inner boundary values and  $o$  denotes outer boundary. Time is given in units of the viscous diffusion time  $\tau_v = d^2/\nu$ , where  $\nu$  is the fluid viscosity. The temperature scale is normalised by the value of the gradient of the background temperature at the outer boundary  $|dT_c/dr|_o$ , multiplied by  $d$  (see Gastine et al. (2020) for a Boussinesq study involving a stable layer implemented in a similar way). The non-dimensionalised velocity is equivalent to a Reynolds number  $Re = ud/\nu$ . The magnetic field is given in units of  $\sqrt{\rho_o \mu \lambda_i \Omega}$ , where  $\mu$  is the magnetic permeability and  $\lambda$  is the magnetic diffusivity which we prescribe as an analytical radial profile.

The dimensionless control parameters that appear in the equations above are the Ekman number ( $E$ ), Rayleigh number ( $Ra$ ), Prandtl number ( $Pr$ ) and magnetic Prandtl number ( $Pm$ ). They are defined as

$$E = \frac{\nu}{\Omega d^2}, \quad Ra = \frac{\alpha g d^4}{\kappa \nu} \left| \frac{dT_c}{dr} \right|_o, \quad Pr = \frac{\nu}{\kappa}, \quad Pm = \frac{\nu}{\lambda}, \quad (3.6)$$

where  $\kappa$  is the thermal diffusivity and  $\alpha$  is the thermal expansivity. The magnetic Prandtl number  $Pm$ , based on a reference value of the magnetic diffusivity, is kept at 0.5. However, the magnetic diffusivity at the lower boundary  $\lambda_i$  is varied.

### 3.2.2 Hydrodynamic Control Parameters

We perform our simulations at a (nominal) Rayleigh number  $Ra = 6 \times 10^8$ , Ekman number  $E = 10^{-5}$  and Prandtl number  $Pr = 0.5$ . This yields a convective Rossby number of:

$$Ro_c = E \sqrt{Ra/Pr} = 0.346, \quad (3.7)$$

so the Coriolis force dominates over inertia.

Some additional simulations are carried out under the anelastic approximation (see Wulff et al. (2022) for the governing equations), with polytropic index 2 and dissipation number 1, yielding a mild density stratification of  $\rho_i/\rho_o = 4$ . From Jones et al. (2009) and Gastine and Wicht (2012), for example, we know that the critical Rayleigh number increases with increasing density stratification. From the latter study we estimate that the increase is roughly two-fold, compared to our Boussinesq models. Therefore, to compare simulations with a similar degree of supercriticality, we double  $Ra$  for the anelastic simulations. The values given above are based on the full shell width  $d$ . Table 3.1 also lists both non-dimensional numbers, re-scaled to the thickness of the convective region (the outer  $\sim 57\%$ ). We also give the Rayleigh number based on the temperature (entropy for the anelastic cases) difference across the convective region alone, calculated from the horizontally averaged temperature (entropy) drop across the convecting region:

$$\text{Boussinesq: } Ra_\Delta = \frac{\alpha g (r_o - r_c)^3 \Delta T}{\kappa \nu}, \quad \text{Anelastic: } Ra_\Delta = \frac{\alpha g T_o (r_o - r_c)^3 \Delta s}{c_p \kappa \nu}, \quad (3.8)$$

where  $r_c$  is the bottom of the convective region.

Sim.	$E$	$E_s$	$E_c$	$Ra$	$Ra_c$	$Ra_\Delta$	$A_s$
H	$10^{-5}$	$5.24 \times 10^{-5}$	$3.15 \times 10^{-5}$	$6 \times 10^8$	$6.04 \times 10^7$	$3.6 \times 10^7$	200
B	$10^{-5}$	$5.24 \times 10^{-5}$	$3.15 \times 10^{-5}$	$6 \times 10^8$	$6.04 \times 10^7$	$2.6 \times 10^7$	200
A	$10^{-5}$	$5.24 \times 10^{-5}$	$3.15 \times 10^{-5}$	$1.2 \times 10^9$	$1.21 \times 10^8$	$6.2 \times 10^7$	100

**Table 3.1.** Nominal Ekman and Rayleigh numbers are based on the full shell thickness and the surface entropy flux. Their re-scaled values,  $E_c$  and  $Ra_c$ , are based on the thickness of the convective region  $d_c = r_o - r_c \approx 0.57$ . The re-scaled Ekman number for the stable region  $E_s$  is also given, based on  $d_s = r_c - r_i \approx 0.43$ .  $Ra_\Delta$  is the Rayleigh number defined by Eq. 3.8.  $A_s$  is the value of  $dT_c/dr$  ( $d\tilde{S}/dr$  for anelastic cases) in the stable region.

### 3.2.3 Stably Stratified Layer

The region  $r > r_c$  is fully convective, whereas at  $r < r_s$  the full degree of stability has been reached, with a transition region at  $r_s < r < r_c$ . This is implemented by prescribing an analytic background entropy gradient profile defined, using auxiliary variable  $\chi = (r - r_c)/(r_c - r_s)$ , by:

$$\frac{dT_c}{dr} = \begin{cases} A_s, & \text{if } r \leq r_s, \\ (A_s + 1) \cdot \chi^2 \cdot (2\chi + 3) - 1, & \text{if } r_s < r < r_c, \\ -1, & \text{if } r \geq r_c \end{cases} \quad (3.9)$$

This is plotted in Fig. 3.1a). In this study we keep  $r_c = 2.77 = 0.831r_o$ ,  $r_s = 2.68 = 0.804r_o$  and  $A_s = 200$  ( $A_s = 100$  for the anelastic cases). Neutral stability is reached around  $0.830r_o$ . The ratio of the Brunt-Väisälä frequency,  $N$ , to the rotation rate, is:

$$N/\Omega = \sqrt{\frac{RaE^2}{Pr} A_s}, \quad (3.10)$$

which is equal to 4.9, at  $r \leq r_s$ . This quantifies the effect of the restoring buoyancy force relative to the rotational forces and corresponds to a degree of stratification around the middle of the range studied in Wulff et al. (2022). This parameter is kept the same for the anelastic cases.

### 3.2.4 Magnetic Parameters

We vary the magnetic diffusivity  $\lambda$ , or the electrical conductivity  $\sigma = 1/\lambda$ , in this study but keep all other diffusivities ( $\nu$  and  $\kappa$ ) constant. We prescribe the magnetic diffusivity to be:

$$\lambda = \lambda_i \exp\left(\frac{1}{d_\lambda}(r - r_i)\right). \quad (3.11)$$

For the profiles where  $\lambda$  would exceed  $10^7$  we cap it at this value to avoid numerical problems. The electrical conductivity scale height is  $d_\sigma = d_\lambda = [(1/\lambda) \cdot d\lambda/dr]^{-1}$ . This simple exponential profile gives the convenience of having a constant scale height throughout the shell.

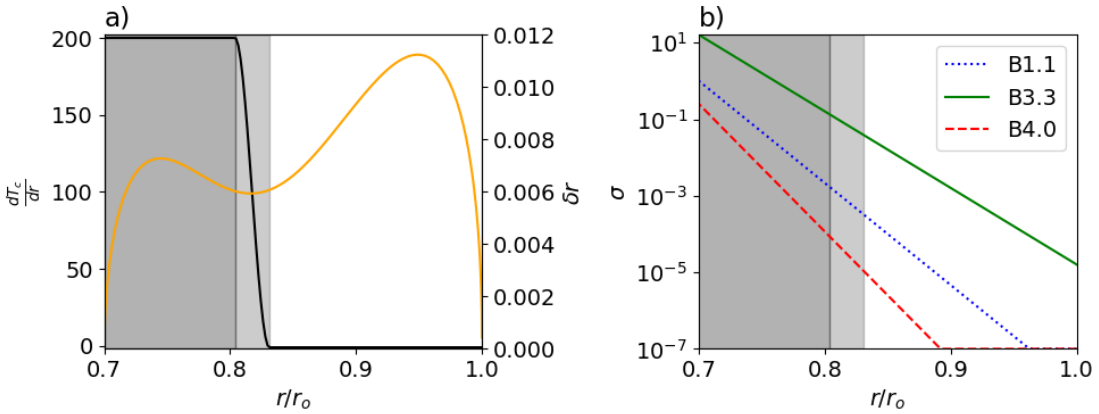


**Figure 3.1.** **a)**  $dT_c/dr$  profile (black) described in Section 3.2.3. The grey shaded region indicates  $r_s < r < r_c$  while the dark grey region is fully stratified. The radial grid-point separation is shown in orange (right y-axis). **b)** electrical conductivity  $\sigma = \lambda^{-1}$  for reference case B1.1 (blue) and extreme cases B3.3 (green) and B4.0 (red).

In our reference model  $\lambda_i = 1$  and  $d_\lambda = 1/\ln(10^8) \approx 0.054$ . To investigate and distinguish the effects of a different local value of electrical conductivity and a different scale-height, we vary both  $d_\lambda$  and  $\lambda_i$  in a systematic parameter study (see Table 3.2). The electrical conductivity profiles of the extremes of the study, B3.3 and B4.0, are shown in Fig. 3.1b). An axial dipole field (poloidal  $\ell = 1, m = 0$  component) with amplitude  $B_{dip}$  at the poles is imposed as a boundary condition at  $r_i$  (negative at the North pole). The other poloidal components and the toroidal field are matched to a field in the inner core, obtained by solving the induction equation in the inner core for a constant value  $\lambda_i$  of the diffusivity. At the outer boundary,  $r_o$ , the magnetic field is matched to a potential field in the exterior. In this study we systematically vary the strength of the applied dipole,  $B_{dip}$ .

### 3.2.5 Numerical Methods

All simulations in this study have been computed using the MHD code MagIC (available at <https://github.com/magic-sph/magic>). We use both the original Boussinesq version (see Wicht, 2002) and that which uses the anelastic approximation (Jones et al. 2011). The governing equations given in Section 3.2 are solved, with stress-free mechanical boundary conditions at both  $r_i$  and  $r_o$  and fixed entropy at the outer boundary and fixed entropy flux (downward in our models) at the inner boundary. This is done by expanding both velocity (or  $\tilde{\rho}\mathbf{u}$  in the anelastic cases) and magnetic fields into poloidal and toroidal potentials. For further details see Christensen and Wicht (2015). The potentials are expanded in Chebychev polynomials in the radial direction and spherical harmonics up to a degree  $\ell_{max}$  in the angular direction.

We use 145 radial grid-points for all simulations in the study. We use a non-linear mapping function (Tilgner 1999) to concentrate the grid-points around the transition from convecting to sub-adiabatic. This ensures both the boundary between the two layers as

Simulation	$\rho_i$	$B_{dip}$	$1/d_\lambda$	$\sigma_i$	$\Lambda(0.8r_o)$	Symbol
H	1	-	-	-	-	-
B1.0	1	0.25	$\ln(10^8)$	1	$6.04 \cdot 10^{-5}$	+
<b>B1.1</b>	<b>1</b>	<b>0.5</b>	<b><math>\ln(10^8)</math></b>	<b>1</b>	<b><math>2.42 \cdot 10^{-4}</math></b>	<b><math>\times</math></b>
B1.2	1	1	$\ln(10^8)$	1	$9.67 \cdot 10^{-4}$	◀
B1.3	1	2	$\ln(10^8)$	1	$3.87 \cdot 10^{-3}$	▶
B2.0	1	0.5	$\ln(10^8)$	0.25	$6.04 \cdot 10^{-5}$	+
B2.2	1	0.5	$\ln(10^8)$	4	$9.67 \cdot 10^{-4}$	◀
B2.3	1	0.5	$\ln(10^8)$	16	$3.87 \cdot 10^{-3}$	▶
B3.0	1	0.5	$\ln(10^6)$	0.25	$2.80 \cdot 10^{-4}$	+
B3.1	1	0.5	$\ln(10^6)$	1	$1.12 \cdot 10^{-3}$	$\times$
B3.2	1	0.5	$\ln(10^6)$	4	$4.49 \cdot 10^{-3}$	◀
B3.3	1	0.5	$\ln(10^6)$	16	$1.80 \cdot 10^{-2}$	▶
B4.0	1	0.5	$\ln(10^{10})$	0.25	$1.30 \cdot 10^{-5}$	+
B4.1	1	0.5	$\ln(10^{10})$	1	$5.21 \cdot 10^{-4}$	$\times$
B4.2	1	0.5	$\ln(10^{10})$	4	$2.08 \cdot 10^{-4}$	◀
B4.3	1	0.5	$\ln(10^{10})$	16	$8.33 \cdot 10^{-3}$	▶
A1.0	4	0.25	$\ln(10^8)$	1	$2.18 \cdot 10^{-5}$	+
A1.1	4	0.5	$\ln(10^8)$	1	$8.70 \cdot 10^{-5}$	$\times$
A1.2	4	1	$\ln(10^8)$	1	$3.48 \cdot 10^{-4}$	◀
A1.3	4	2	$\ln(10^8)$	1	$1.39 \cdot 10^{-3}$	▶
A2.0	4	0.5	$\ln(10^8)$	0.25	$2.18 \cdot 10^{-5}$	+
A2.2	4	0.5	$\ln(10^8)$	4	$3.48 \cdot 10^{-4}$	◀
A2.3	4	0.5	$\ln(10^8)$	16	$1.39 \cdot 10^{-3}$	▶

**Table 3.2.** Simulations carried out with critical varied parameters given. The reference case is in bold.

well as the shell boundary regions are well-resolved, as illustrated in Fig. 3.1. See the Appendix for details on the mapping

For the reference case, labelled B1.1, we carried out one simulation without any imposed azimuthal symmetry, using azimuthal resolution  $n_\phi = 1280$  and without hyper-diffusivity. For the other cases we introduced a four-fold azimuthal symmetry, reduced the number of grid-points to  $n_\phi = 864$  and applied hyper-diffusion, where the diffusion parameters (thermal and viscous) are multiplied by the factor

$$\nu(\ell) = \kappa(\ell) = 1 + D \left[ \frac{\ell + 1 - \ell_{hd}}{\ell_{max} + 1 - \ell_{hd}} \right]^\beta, \quad (3.12)$$

for  $\ell \geq \ell_{hd}$ , where  $\ell_{hd} = 250$ ,  $D = 4$  and  $\beta = 2$ . We verified that in the reference case the zonal winds formed and other features vital for our analysis did not change with imposed symmetry and hyper-diffusion.

All analysis was then based on the final stage of the simulations, which were integrated for 800,000 time-steps after they were fully equilibrated which is around  $0.2\tau_v$  ( $\sim 20,000$  rotations).

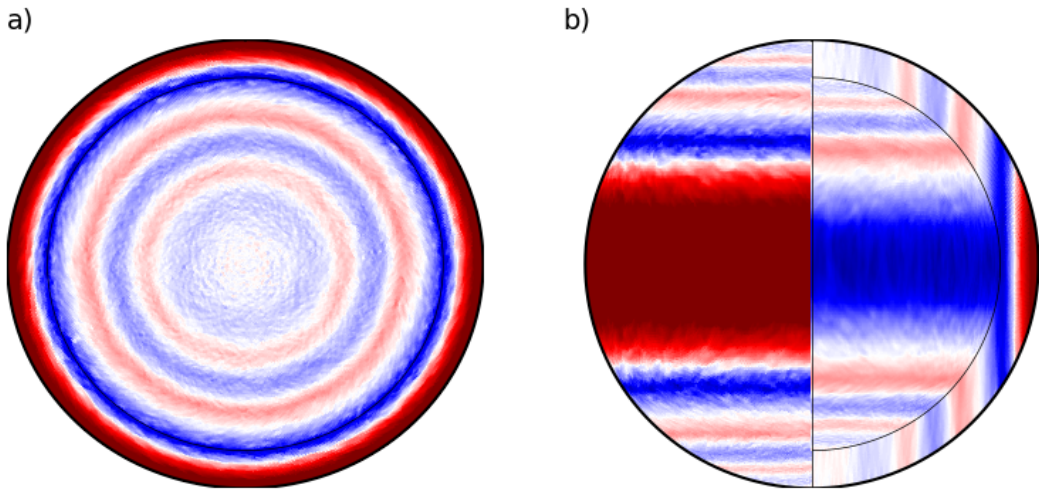


**Figure 3.2.** A snapshot of the azimuthal flow,  $u_\phi$ , for the reference case B1.1. Both plots use the same colour-scale with a dynamic range of  $\pm 6000$ , where red (blue) indicates prograde (retrograde) flow. **a)** View onto the surface of the spherical shell from the North Pole. **b)** Front view of the surface flow on the left and a cut down to the bottom of the convecting layer on the right.

## 3.3 Results

In our study we vary the strength of the imposed dipole field,  $B_{dip}$ , the electrical conductivity at the inner boundary,  $\sigma_i$ , and the conductivity scale height,  $d_\sigma$ . The parameters are summarised in Table 3.2. We explore the surface zonal wind profiles, their extension into the interior and the mechanisms by which they are quenched.

### 3.3.1 Zonal Wind Distribution

The snapshot of our reference case B1.1, in Fig. 3.2, shows that these simulations reproduce one of the key features found in the measurements of the zonal flows of the two gas giants: a set of alternating zonal jets reaching up the high latitudes. The equatorial prograde jet and its flanking retrograde jets dominate, but slightly weaker flows also persist up to the poles. These extend geostrophically, i.e. invariant with respect to  $z$  which is parallel to the rotation axis, throughout the convective region. We show the time-averaged, axisymmetric zonal flow for only one hemisphere of the hydrodynamic comparison case H in Fig. 3.3a. Plotted on top of this is the surface profile as a function of the cylindrical coordinate  $s = r \sin \theta$ , i.e. the distance from the axis of rotation. We observe that in case H, without either the additional magnetic forces or a mechanical rigid boundary condition which can act as a proxy for some force that brakes the jets, the jets are much wider and their amplitude (in this case that of the only retrograde jet present inside the tangent cylinder) only decreases slightly when reaching the stable layer. We note that a similar purely hydrodynamic simulation with a stress-free flow boundary shown in Figure 3d of Wulff et al. (2022) also shows a zonal flow pattern unlike that of Jupiter or Saturn,

with a few strong jets inside the tangent cylinder (TC) that decay only weakly towards the inner boundary. The differences to the present case can be attributed to the anelastic approximation and a larger degree of stability in Wulff et al. (2022).

However, Figures 3.3b and c demonstrate that under the influence of finite conductivity and a large-scale magnetic field, the zonal flows develop a multiple jet structure. Furthermore, the jets are quenched effectively in the stable layer. The two cases shown, B4.0 and B3.3, are the extremes in the study. In B4.0 the conductivity starts out rather small at the inner boundary and drops rapidly with radius. This case shows strong zonal winds in the tangent cylinder reaching the polar region. In B3.3 the conductivity at  $r_i$  starts out rather large and drops more weakly with radius. Here, significant jets are still found at mid-latitude, but they fade out at the high latitudes. The vertical extent of the convective region, i.e. the depth of the stable layer, is not altered in the study so the TC is in the same location and the equatorial prograde jet has the same width, with the peaks of the flanking retrograde jets being located on the TC.

The relation between the jet widths and jet amplitudes was confirmed to obey Rhines scaling well, when taking the convective region as the shell thickness (following the methodology detailed in Gastine et al. (2014)). This predicts that narrower jets are also weaker. In order to quantify the strength of the axisymmetric zonal flow inside the tangent cylinder (TC), we define the average surface zonal flow amplitude in this region as:

$$U_{surf} = \frac{1}{2\theta_c} \left( \int_0^{\theta_c} \sqrt{\langle \bar{u}_\phi(r_o, \theta) \rangle^2} \sin \theta d\theta + \int_{\pi-\theta_c}^{\pi} \sqrt{\langle \bar{u}_\phi(r_o, \theta) \rangle^2} \sin \theta d\theta \right), \quad (3.13)$$

where  $\sqrt{\langle \bar{u}_\phi(r_o, \theta) \rangle^2}$  is the time-averaged, axisymmetric, rms surface zonal flow and  $\theta_c = \sin^{-1}(r_c/r_o)$ , i.e. the colatitude associated with the location of the TC at the surface. This definition broadly captures both the extent and strength of the zonal flow and facilitates a comparison between all cases.

We observe that simulations with a stronger imposed dipole field strength,  $B_{dip}$ , and those with higher electrical conductivity,  $\sigma$ , have weaker winds inside the TC. We use a local Elsasser number  $\Lambda(r) = B_{dip}(r)^2 \sigma(r)/\rho\Omega$  as a proxy for the local strength of the Lorentz force, relative to the Coriolis force, although in this study we only explicitly test the dependency on  $B_{dip}$  and  $\sigma$ . This expresses not only the radial variation of the electrical conductivity but also the  $r^{-3}$  dependence of the dipole field strength (in our definition we use the axial dipole field amplitude at the poles).

In Fig. 3.3d we therefore plot  $U_{surf}$ , as a function of the Elsasser number evaluated at  $0.8r_o$ , i.e. in the upper part of the stable layer, just below  $r_s$ . The extremes of our parameter sweep are  $\Lambda(0.8r_o) = 1.30 \cdot 10^{-5}$  in case B4.0, up to  $1.80 \cdot 10^{-2}$  in case B3.3 (see Table 3.2).

The plot suggests that if magnetic forces remain insignificant near the SSL boundary, strong zonal winds can develop and be maintained in the overlying convecting region and are independent of the magnetic effects coming into play deeper in the stable region. However, when magnetic effects become more pronounced in the upper part of the stable layer, the zonal flow inside the TC becomes somewhat more diminished, in particular at high latitudes. Within our parameter sweep this is not a dramatic effect. As our focus is on models that have strong jets inside the TC so we do not go beyond case B3.3. We would expect these to disappear if the semiconducting region begins at even shallower

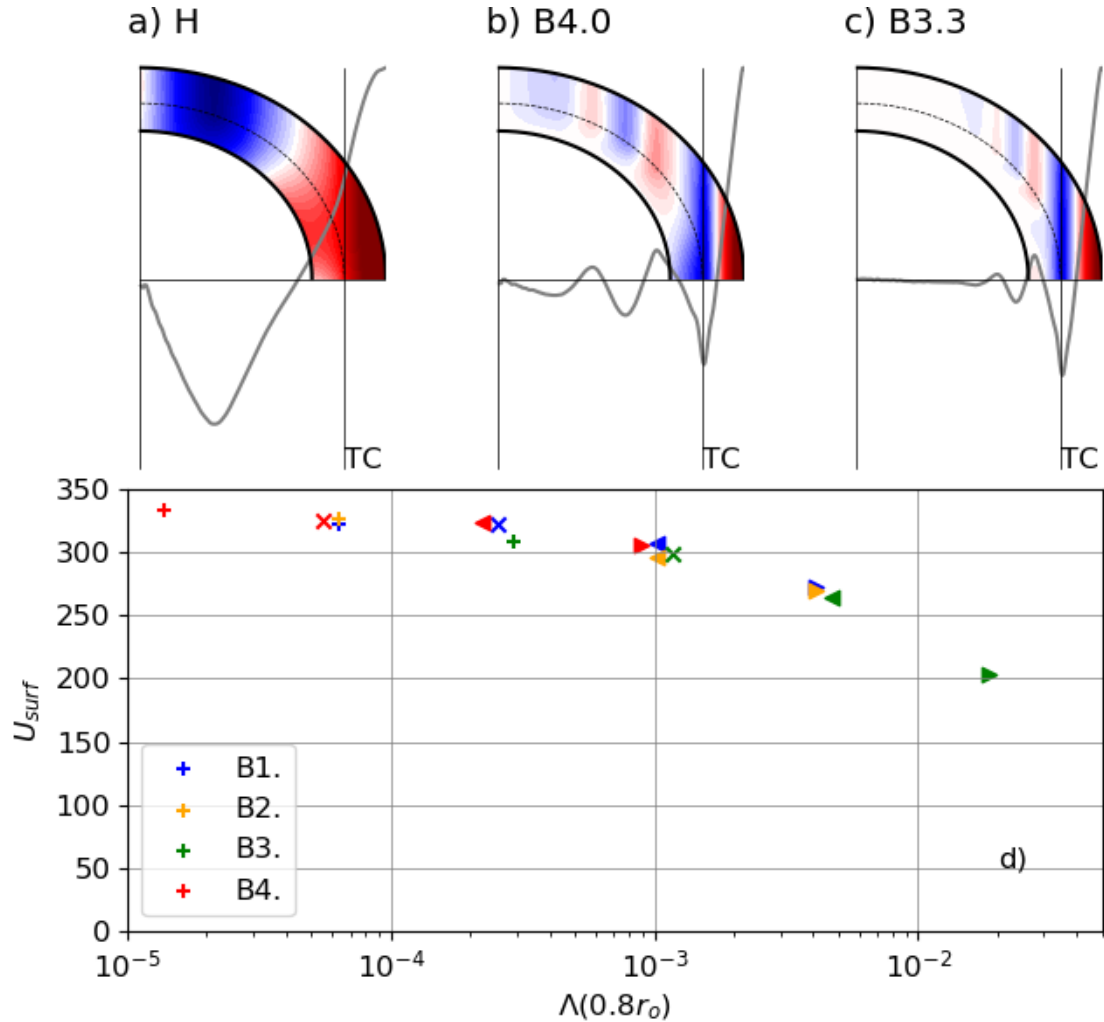


**Figure 3.3.** Time-averaged axisymmetric zonal flow for simulations H in panel **a**), B4.0 in panel **b**) and B3.3 in panel **c**) (see Table 3.2) with the same colour-scale as Fig. 3.2, with range  $\pm 6000$ . On top of these are plotted the respective surface wind profiles as a function of  $s$  for the hemisphere shown. The thin vertical lines indicate the locations of the tangent cylinders associated with the bottom of the convective region, TC. **d)** shows the average zonal flow velocity inside the TC (defined by eq. 3.13), as a function of the local Elsasser number evaluated at  $0.8r_o$ . See table 3.2 for the symbols for each case.

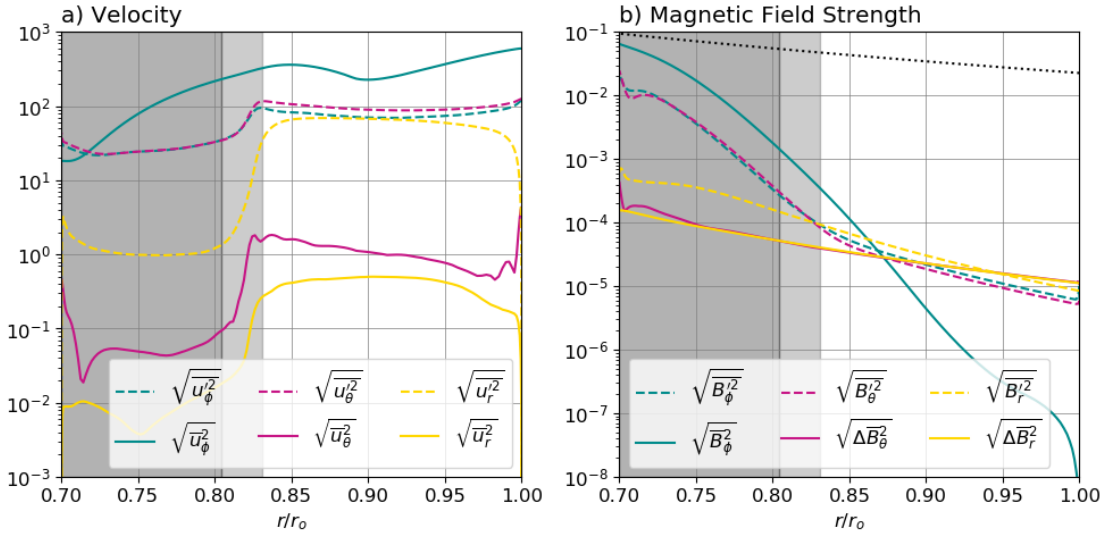


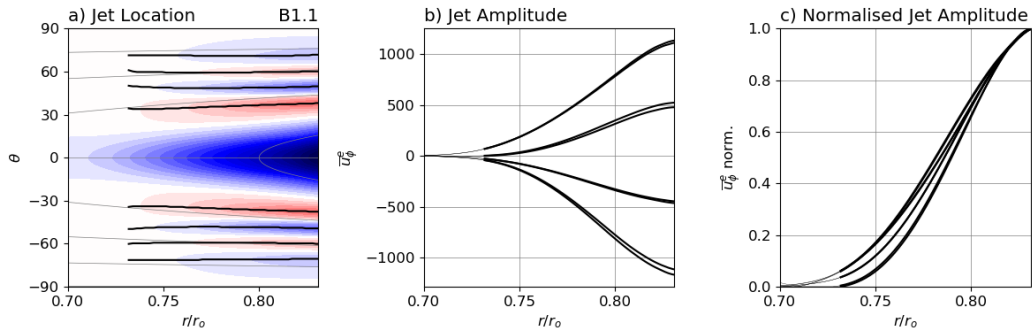
**Figure 3.4.** Radial profiles of time- and horizontally-averaged **a)** velocity and **b)** magnetic field strength (given in  $\Lambda$ ) for the reference case B1.1. The dashed lines show the average non-axisymmetric flow (field strength) and the solid lines are the axisymmetric parts, where colours indicate the three components. For  $\bar{B}_\theta$  and  $\bar{B}_r$ , we subtract the dipole component, of which the average amplitude is shown by the black dotted line. The dark grey (grey) shading indicates the (transition into the) SSL.

depths and  $\Lambda(0.8r_o)$  is increased by even just one more order of magnitude.

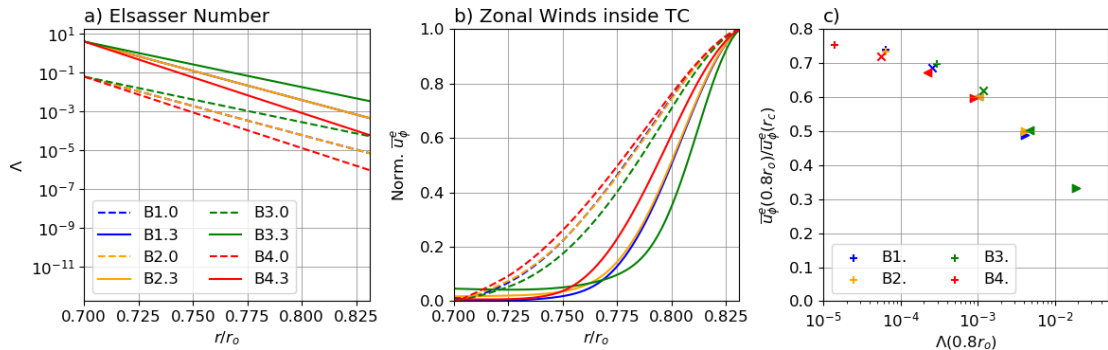
### 3.3.2 Flow Amplitude Versus Depth

Fig. 3.4a) shows the horizontally averaged rms velocity components for the reference simulation as a function of radius, where solid lines show the axisymmetric components (labelled with an overbar) and dashed lines the non-axisymmetric components (indicated by a prime). In the convective region, the convective flow amplitude ( $u'_\phi$ ,  $u'_\theta$  and  $u'_r$ ) is almost an order of magnitude weaker than the rms zonal wind amplitude (the jet peaks themselves are even stronger). Upon reaching the SSL, radial flow components are quenched most effectively and amplitudes drop by almost two orders of magnitude. At least part of the remaining radial motion seen in Fig. 3.4 may represent wave motion (gravity waves, inertial waves) and no overturning motion. Right at the SSL boundary both the latitudinal component of the meridional flow,  $\bar{u}_\theta$ , and the horizontal components of the convective flow,  $u'_\phi$  and  $u'_\theta$ , increase very slightly which may be attributed to the deflection of the radial flows. However, further into the SSL all other flow components are damped. We analyse this in more detail for the zonal flow.

We track the jet amplitude as a function of radius in the SSL. This is illustrated in Fig. 3.5a) where we show the locations of the maxima/minima of the jets inside the TC for simulation B1.1. This tracking is vital as the locations of the peak velocity is no longer  $z$ -invariant in the SSL in contrast to the convective region, as can be seen in Fig. 3.3b and c.



**Figure 3.5.** Illustration of the jet tracking method described, applied to the reference case B1.1. **a)** shows the zonal flow pattern in the SSL ( $r < r_c$ ). The black lines show the locations of the zonal flow extrema (denoted by superscript  $e$ ) and the grey lines indicate lines of constant  $s$ . **b)** shows the peak amplitudes of these 8 jets as a function of radius and in **c)** we normalise this by the jet flow velocity at  $r = r_c$ .



**Figure 3.6.** **a)** Elsasser number as a function of depth in the SSL ( $r < r_c$ ) for the end-members of each of the Boussinesq sets. **b)** shows the normalised jet amplitude profiles as shown in Fig. 3.5c where a single profile is obtained for each case by averaging over all 8 jets. **c)** ratio of zonal flow amplitude at  $0.8r_o$  and the jet flow velocity at  $r = r_c$ , obtained from the averaged profiles shown in **b)** and the remaining models omitted on this plot. See Table 3.2 for the symbols for each case.

Fig. 3.5b shows  $\bar{u}_\phi^e$  along the centres of these jets (we use superscript  $e$  to denote the extrema of  $\bar{u}_\phi$  as a function of latitude). This also highlights the strong equatorial symmetry of these particular simulations where the northern/southern hemisphere jet pairs have almost identical velocity profiles. Finally, Fig. 3.5c shows the same velocity profiles, with each one normalised by the respective jet velocity at  $r_c$ . This plot clearly illustrates that the relative decay with depth is rather similar for all jets, independent of their location inside the TC.

We average the radial profiles of all jets inside the TC, normalised by their velocity at the bottom of the convecting region, for each case to quantify the zonal wind decay. Fig. 3.6b compares averaged profiles for the end-member simulations of each of the Boussinesq sets while Fig. 3.6a shows the respective Elsasser number profiles in the SSL. Profiles with identical  $\Lambda(r)$  (sets B1. and B2.) nearly perfectly overlap which highlights that the Elsasser number is the crucial parameter here; doubling the axial dipole field strength has

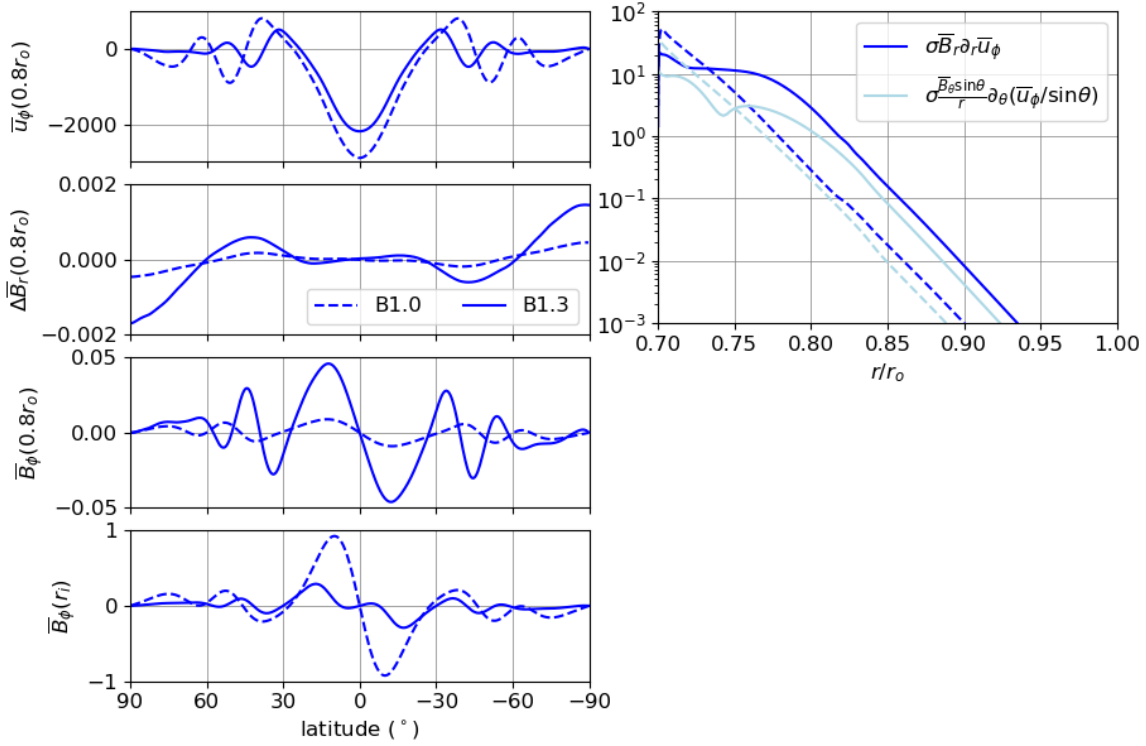


**Figure 3.7.** Left: Latitudinal profiles for cases B1.0 and B1.3. The top panels show  $\bar{u}_\phi$  and  $\Delta \bar{B}_r = \bar{B}_r - \bar{B}_r^{dip}$  on  $0.8r_o$ . The lower panels are  $\bar{B}_\phi$  at  $0.8r_o$  and  $r_i$ . Right: Horizontally averaged, rms amplitude of the two terms in the  $\Omega$ -effect for the same cases, where dashed(solid) corresponds to B1.0(B1.3) and dark(light) blue corresponds to the radial(latitudinal) shear term.

exactly the same effect as quadrupling the electrical conductivity. When considering the other profiles shown we clearly see that in simulations with the lowest Elsasser numbers the decay of the zonal wind is very gradual. This is illustrated in Fig. 3.6c where we plot the ratio of the jet amplitude at  $0.8r_o$  and the amplitude at  $r_c$ , again averaging over all 8 jets to obtain one value per simulation. Therefore, magnetic effects are crucial in reducing the penetration distance of zonal winds into the SSL.

### 3.3.3 Magnetic Field Induction

Fig. 3.4b shows the horizontally averaged induced magnetic field components for the reference case. The induced axisymmetric toroidal field is almost as strong as the dipole field at the lower boundary, for this case, but drops off rapidly with radius. The induced axisymmetric radial and latitudinal fields,  $\Delta \bar{B}_r$  and  $\Delta \bar{B}_\theta$ , i.e. the perturbations of the imposed poloidal field, are almost three orders of magnitude smaller but do not drop off in amplitude as sharply over the SSL.

We investigate the difference in the induction when changing the imposed axial dipole field strength in Fig. 3.7. On the left the top three plots are latitudinal profiles of  $\bar{u}_\phi$ ,  $\Delta \bar{B}_r = \bar{B}_r - \bar{B}_r^{dip}$  and  $\bar{B}_\phi$  at  $0.8r_o$ . These are all as we may expect, with B1.3 having the strongest induced magnetic fields. This is due to it having the largest imposed dipole amplitude, eight times stronger than case B1.0 with the same conductivity profile, leading

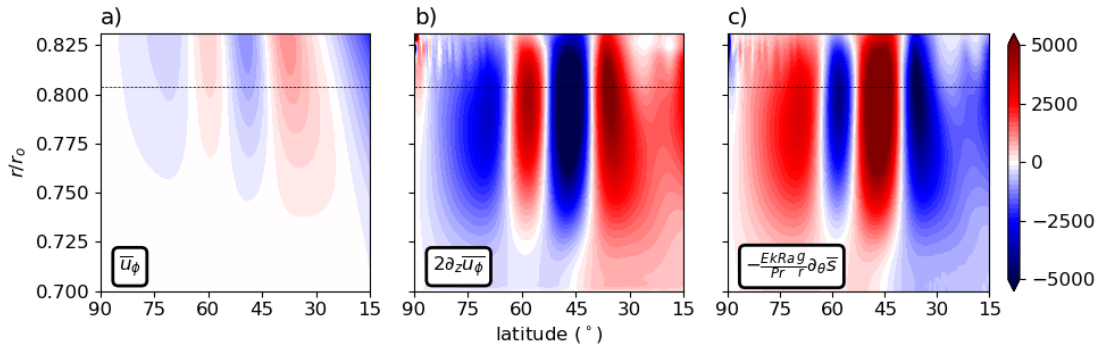


**Figure 3.8.** The transition region and SSL of the reference case B1.1, shown for the northern hemisphere. All terms are zonally and temporally averaged. **a)**  $\bar{u}_\phi$ , the zonal flow, **b)** the vertical gradient of the zonal flow and **c)** the latitudinal entropy fluctuation. The thin horizontal line indicates  $r_s$ , i.e. the bottom of the transition region into the SSL.

to a larger  $\Omega$ -effect. The  $\Omega$ -effect describes the induction of axisymmetric toroidal field by the shearing of the axisymmetric poloidal field by differential rotation and has the two components  $\bar{B}_r \partial_r \left( \frac{\bar{u}_\phi}{r} \right)$  and  $\frac{\bar{B}_\theta \sin \theta}{r} \partial_\theta \left( \frac{\bar{u}_\phi}{\sin \theta} \right)$ . From this we see that the assumption that a stronger dipole will lead to a stronger induced field holds only when the simulations with different  $B_{dip}$  have similar distributions of  $\bar{u}_\phi$ . However, in Fig. 3.6b we see that the zonal wind is quenched very effectively in case B1.3, so  $\bar{u}_\phi$  is almost zero at mid-depth of the stable layer, while this only happens near the bottom in case B1.0. Therefore, the  $\Omega$ -effect is stronger for case B1.0 than for B1.3 in the lower third of the stable layer and the amplitude of the induced field,  $\bar{B}_\phi$ , exceeds that of B1.3 significantly, as can be seen in the bottom panel of Fig. 3.7. In fact, for case B1.0 it also exceeds the amplitude of the imposed dipole field at the lower boundary which for this case is  $B_r(r_i, \theta = 0) = -0.25$ . Thus, the model, B1.0, which has the most interaction between the zonal flow and the electrically conducting region (i.e. over the greatest depth range) actually has the weakest induced field strength near the top of its conducting region.

The morphology of the induced  $\bar{B}_\phi$  field can also be better understood by comparing the contributions of the two terms that make up the  $\Omega$ -effect; the radial and the latitudinal shear of the zonal wind. This is shown on the right in Fig. 3.7, where the rms amplitude of the two terms has been averaged horizontally to produce radial profiles. For both cases, B1.0 and B1.3, the radial shear is the more dominant term throughout the shell. Therefore, the decay of the jets with depth produces a stronger gradient than the transition between oppositely flowing jets. This also leads to the induced azimuthal field being strongest almost exactly on the zonal wind peaks.

### 3.3.4 Zonal Wind Truncation Mechanism

A thermo-magnetic wind equation can be derived by taking the  $\phi$ -component of the curl of the Navier-Stokes equation, then averaging over azimuth and assuming steady state:

$$0 = \frac{2E}{s} \bar{u}_\phi \partial_z \bar{u}_\phi - E s \bar{u}_s \partial_s \frac{\bar{\omega}_\phi}{s} - E \bar{u}_z \partial_z \bar{\omega}_\phi + 2 \partial_z \bar{u}_\phi - \frac{RaE}{Pr} \frac{1}{r} \partial_\theta \bar{\vartheta} \\ + \frac{1}{Pm} [\nabla \times (\mathbf{j} \times \mathbf{B})]_\phi + E [\nabla^2 \bar{\omega}]_\phi, \quad (3.14)$$

where  $\omega = \nabla \times \mathbf{u}$  is the vorticity and  $\mathbf{j} = \nabla \times \mathbf{B}$ . The first three terms are from the advection term, the fourth and fifth terms are from the Coriolis force and buoyancy, respectively. The last two terms are from the Lorentz force and the viscous force. We find that in our simulations, the equation can be reduced to:

$$0 \approx 2 \partial_z \bar{u}_\phi + \frac{RaE}{Pr} \frac{1}{r} \partial_\theta \bar{\vartheta}, \quad (3.15)$$

as all other terms were found to be negligible. This is shown in Fig. 3.8**b** and **c** where we plot the vertical gradient of the zonal wind (first term of eq. 3.15) and the latitudinal temperature gradient (second term of eq. 3.15). The two are in nearly perfect balance; the magnetic term of the thermo-magnetic wind equation is negligibly small. As in the hydrodynamic simulations in Wulff et al. (2022), the decrease of the zonal wind in the stable layer is controlled by a thermal wind balance. The associated density perturbation is caused by a meridional flow. As Lorentz forces play a critical role for the penetration of the winds into the stable layer, this should happen via their influence on the meridional circulation. To elucidate this, we consider (as in Wulff et al. (2022)) the time-averaged (denoted by  $\langle \rangle$ ) axisymmetric, azimuthal component of the Navier-Stokes equation, given by:

$$0 = \langle \bar{F}_{Ad} \rangle + \langle \bar{F}_C \rangle + \langle \bar{F}_R \rangle + \langle \bar{F}_v \rangle + \langle \bar{F}_{Ma} \rangle + \langle \bar{F}_{Mna} \rangle; \\ \bar{F}_{Ad} = \frac{\bar{u}_s}{s} \partial_s (s \bar{u}_\phi) + \bar{u}_z \partial_z (\bar{u}_\phi) \\ \bar{F}_C = \frac{\frac{2}{E} \bar{u}_s}{\bar{u}_s} \\ \bar{F}_R = \frac{\frac{1}{s^2} \partial_s [s^2 \bar{u}'_s \bar{u}'_\phi]}{s^2} + \partial_z [\bar{u}'_z \bar{u}'_\phi] \\ \bar{F}_v = -\frac{1}{s^2} \partial_s [s^3 \partial_s (\frac{\bar{u}_\phi}{s})] - \partial_z [\partial_z (\bar{u}_\phi)] \\ \bar{F}_{Ma} = \frac{-\frac{1}{EPm} [\frac{1}{s^2} \partial_s (s^2 \bar{B}_\phi \bar{B}_s) + \partial_z (\bar{B}_\phi \bar{B}_z)]}{EPm} \\ \bar{F}_{Mna} = \frac{-\frac{1}{EPm} [\frac{1}{s^2} \partial_s (s^2 \bar{B}'_\phi \bar{B}'_s) + \partial_z (\bar{B}'_\phi \bar{B}'_z)]}{EPm}. \quad (3.16)$$

This includes the: ‘advection’ force  $\bar{F}_{Ad}$ , Coriolis force  $\bar{F}_C$  and viscous force  $\bar{F}_v$ . The forces associated with the Reynolds stresses and the Maxwell stresses are  $\bar{F}_R$ , and  $\bar{F}_{Ma}$  and  $\bar{F}_{Mna}$  respectively, where the former is the contribution from the large-scale (axisymmetric) magnetic field components and the latter is from the small-scale (non-axisymmetric) field components.

We find that the advective force remains negligibly small and therefore omit it in Fig. 3.9 where we show the zonal force balance. Furthermore, the Maxwell stresses arising from the correlation of the small-scale magnetic field components,  $\bar{F}_{Mna}$ , also remain very

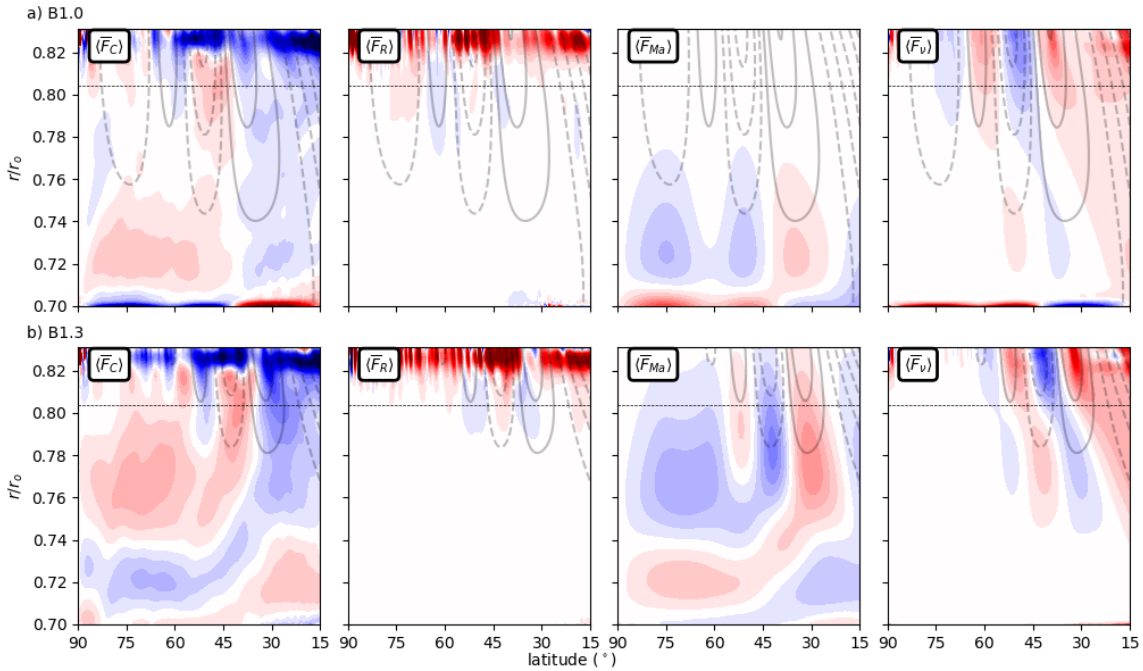


**Figure 3.9.** The zonally and temporally averaged azimuthal component of the force balance, shown for cases **a)** B1.0 and **a)** B1.3, in the transition region and SSL for one hemisphere. The panels show the Coriolis term,  $\bar{F}_C$ ; Reynolds stresses,  $\bar{F}_R$ ; viscosity,  $\bar{F}_v$ ; and Lorentz forces,  $\bar{F}_{Ma}$ . The horizontal black line indicates  $r_s$ , which is also roughly the depth at which Lorentz forces become significant and  $\bar{F}_R$  becomes negligible. Solid (dashed) grey contours indicate positive (negative)  $\bar{u}_\phi$ .

small, even at depth and are thus also not shown in Fig. 3.9. This is because in our study the stable layer suppresses small-scale flows so effectively. The conductivity distribution implies that the Lorentz forces only start acting in the SSL in these simulations, where only very weak non-axisymmetric induced magnetic field components contribute.

The first panels in Fig. 3.9 show the Coriolis force, which is directly proportional to the  $s$ -component of the meridional flow. This meridional flow is driven in the convecting (not shown) and transition region, where the associated Coriolis force is balanced mainly by the Reynolds stresses. The Reynolds stress force is enhanced in the transition region, by the same mechanism as in the purely hydrodynamic study (Wulff et al. 2022), where radial flows and also all small-scale motion is quenched (see Fig. 3.4). Therefore there is a sharp drop-off in the correlation of the convective flows just below  $r_c$ , leading to large derivatives with respect to  $s$  and  $z$  (see eq. 3.16 for the definition of  $\bar{F}_R$ ). The large Reynolds stress force is primarily balanced by the Coriolis force  $\bar{F}_C$  of an enhanced meridional circulation. Inside the SSL there is a good match of  $\bar{F}_C$  and the force associated with the Maxwell stresses,  $\bar{F}_{Ma}$ . This is the essential difference to the hydrodynamic models where only viscosity can balance  $\bar{F}_C$  in this region. In the MHD case, the meridional flow remains significant in the SSL, so entropy perturbations are induced (see Fig. 3.8) and the zonal flow can be quenched more effectively in the SSL. This is broadly in agreement with the mechanism proposed by Christensen et al. (2020), where the winds were driven by an ad-hoc force rather than self-consistently by Reynolds stresses. We observe that the viscous force also plays a significant role in the SSL, as the zonal flow velocity is de-

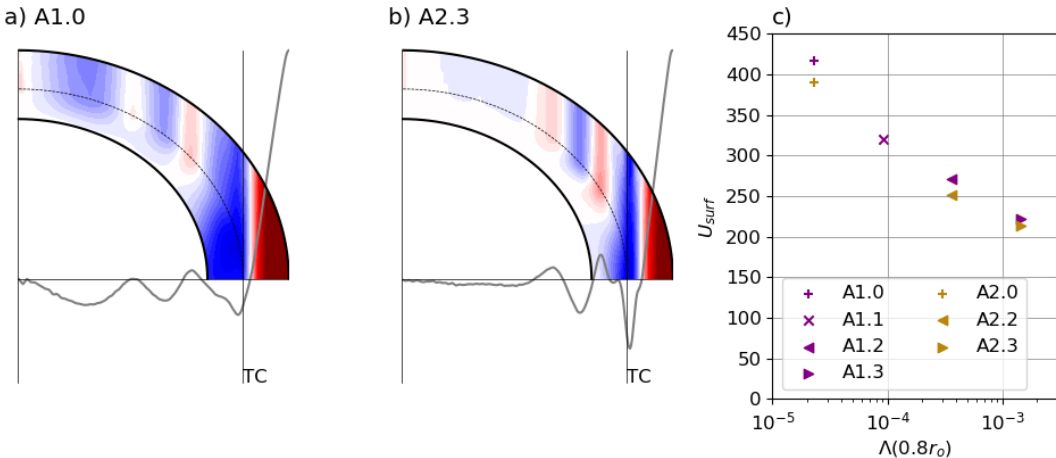


**Figure 3.10.** a) and b) show the time-averaged axisymmetric zonal flow for simulations A1.0 and A2.3 (see Table 3.2) with the same colour-scale as Fig. 3.2, with range  $\pm 6000$ . On top of these are plotted the respective surface profiles as a function of  $s$  for the hemisphere shown. The thin vertical lines indicate the locations of the tangent cylinders associated with the bottom of the convective region, TC. c) shows the average zonal flow velocity inside the TC (defined by eq. 3.13), as a function of the local Elsasser number evaluated at  $0.8r_o$ . See table 3.2 for the symbols for each case.

ing rapidly. At the much lower Ekman numbers that apply to the gas planets, viscosity is expected to play no significant role.

Comparing Figures 3.9a) and b) we first note that in case B1.3 where the dipole strength is increased (Fig. 3.9b)), the Lorentz forces already begin to act in the SSL transition region. This illustrates how they are able to impact the structure of the zonal winds in the top part of the stable region. Deeper in the stable region similar meridional circulation cells develop for both models, to balance the Lorentz forces. However, they are shifted upwards in case B1.3 relative to B1.0. In model B1.0 the winds only reach near-zero amplitude near the inner shell boundary and the transition from equator-ward (pole-ward) flow in the high- (mid-) latitude region to oppositely flowing meridional circulation occurs close to this boundary. In case B1.3 the winds are already quenched at around  $0.74r_o$  which is where the circulation cells are centred in this model.

### 3.3.5 Anelastic Simulations

For seven models with different field strengths and conductivity profiles we replaced the Boussinesq approximation by the anelastic approximation in order to test its impact on the results (sets A1. and A2. in Table 3.2). Qualitatively, the zonal flows formed in these simulations are very similar to their Boussinesq counterparts, with the strongest jets being the prograde equatorial jet and its flanking retrograde jets, complemented by another four weaker jets inside the tangent cylinder (see figures 3.10a and b)). In these simulations we also observed some time-variability in the zonal flow structure, similar to that discussed in Wulff et al. (2022), which we do not explore further within this work.

Fig. 3.10 is the counterpart to Fig. 3.3, showing the dependence of the rms zonal flow amplitude at the surface, inside the TC, on the local Elsasser number. While  $\Lambda$  covers a

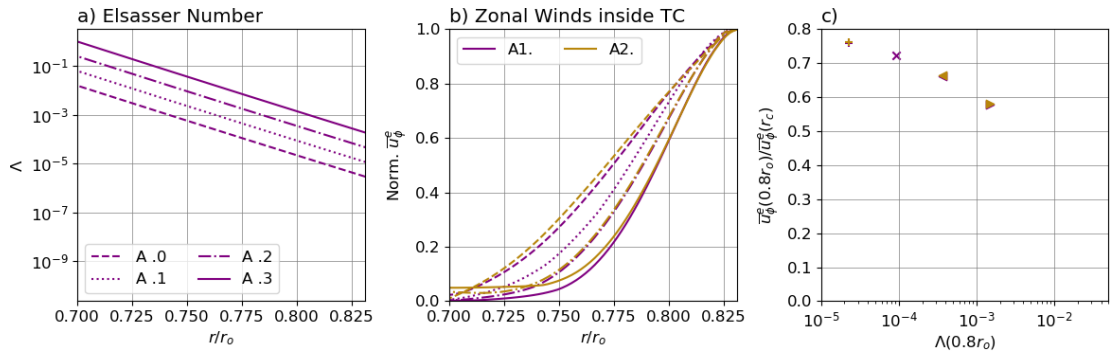


**Figure 3.11.** **a)** Elsasser number as a function of depth in the SSL ( $r < r_c$ ) for all 7 anelastic models. **b)** shows the normalised jet amplitude profiles as shown in Fig. 3.5c where a single profile is obtained for each case by averaging over all 8 jets. **c)** shows ratio of zonal flow amplitude at  $0.8r_o$  and the jet flow velocity at  $r = r_c$ , obtained from the averaged profiles shown in **b)**. See Table 3.2 for the symbols for each case.

smaller range than the Boussinesq study, the same trend is clearly seen: stronger winds develop in models where magnetic effects, characterised by  $B_{dip}^2\sigma$ , become significant only deeper into the stable layer.

We also test the relationship of the local Elsasser number and the zonal wind penetration distance for these anelastic models. We use the same analytical technique described in Section 3.3.2 and track the jet amplitudes in the stable layer. This is shown in Fig. 3.11. As Fig. 3.11a shows, the two sets A1. and A2. have the same 4 radially varying Elsasser number profiles (with A1.1 forming part of both sets). However, in one set the axial dipole field strength,  $B_{dip}$ , is varied while in the other the electrical conductivity profile is varied (the conductivity scale height remains the same). Fig. 3.11b shows that the models with the same  $\Lambda(r)$  have near-to identical zonal flow decay in the stable layer, with the zonal winds in models with a stronger imposed dipole strength or a greater electrical conductivity (A1.3 and A2.3 respectively) being quenched most effectively. Although the variation of the background density with radius is rather weak in our models, this suggests that our observations from the Boussinesq models also hold when there is a variable background density. Furthermore, Fig. 3.11c, where we plot the ratio of jet amplitude at  $0.8r_o$  to that at  $r_c$ , shows that the  $1/\tilde{\rho}(r)$  dependency of the local Elsasser number leads to a more gradual damping of  $\bar{u}_\phi$  in these models compared to cases B1. and B2., their Boussinesq equivalents. Fig. 3.11c has the same axes as Fig. 3.6c to highlight that these models fit on the same trend line. This is possible for this analysis as the relative decay is evaluated, while the absolute jet amplitudes are difficult to compare with the Boussinesq models.

## 3.4 Discussion and Conclusions

We find that the amplitude and latitudinal extent of zonal flow in the convective region, depends directly on the amplitude of the magnetic forces near the top of the underlying stable region. If these are negligible, due to both a weak dipole field strength and very weak conductivity, the zonal flow at the surface develops a structure and amplitude inde-

pendent of the magnetic effects acting deep in the stable region below. If Lorentz forces are non-negligible at the bottom of the convective region, they will impact the jets formed above, in particular diminishing those inside the tangent cylinder (see Figures 3.3d) and 3.10c)).

The penetration distance of zonal flows into the stable layer is dependent on the product  $\sigma B^2$  at depth. For a fixed profile of  $\sigma B^2$ , it can be expected from Wulff et al. (2022) that the degree of stratification,  $N/\Omega$ , also influences the damping of the zonal winds in the stable layer, as well as other parameters. Christensen et al. (2020) suggest that for a fixed  $\sigma$  and  $B$ , and in the limit of negligible viscosity, the combination  $(N/\Omega)^2 E_\kappa^{-1}$  is relevant, where  $E_\kappa = \kappa/\Omega d^2$  is an Ekman number based on the effective thermal diffusivity in the stable layer.

When investigating the braking mechanism of the winds in the stable layer, we confirm the findings of Christensen et al. (2020) and are also able to explore this further using different models. Firstly, the quenching of  $\bar{u}_\phi$  in the stable layer is governed by a thermal wind balance, without magnetic winds playing a role. The temperature perturbation required to facilitate this is generated by meridional circulation in the stable region. Secondly, a significant toroidal field is induced due to the  $\Omega$ -effect, while the induced poloidal field remains orders of magnitude smaller than the imposed dipole field.

Lorentz forces only start acting in the stable region, where small-scale motions are very weak. Therefore they are primarily due to the correlation of the toroidal field, induced by the zonal flows, and the imposed dipole field, as the correlations of the non-axisymmetric field components remain negligible (in contrast to what Dietrich and Jones (2018) found when varying the radial conductivity profile, without a stable layer). As the Lorentz forces are balanced by Coriolis forces, i.e. the meridional circulation, they indirectly influence the damping of the zonal flows in the stable region. While viscous forces are not dominant in the force balance for the meridional flow, they are not negligible either in our simulations (see Fig. 3.9), in contrast to what may be assumed in the gas planets.

More comprehensive simulations that include the dynamo region (Gastine and Wicht 2021, Moore et al. 2022) also showed zonal winds inside the tangent cylinder that drop off inside a shallow stably stratified region. Our simpler models, comprising only of the outer regions of the gas planets and imposing a dipolar magnetic field are computationally more economical and allow a more extensive parameter study. Therefore, we are able to compare the influence of varying magnetic parameters and study what factors make the zonal wind damping more efficient. Furthermore, in contrast to Moore et al. (2022) our models feature multiple zonal jets, making them more gas planet-like and allowing us to make a systematic study of jet formation and structure.

A possible avenue for future work would be to introduce a more complex imposed field at the lower boundary, to study the influence of non-axial-dipole components of the magnetic field, such as intense flux concentrations, similar to Jupiter's observed Great Blue Spot, on the zonal winds.

## 4 Conclusion and Outlook

The striking zonal winds observed on the gas giants are mysterious in terms of their driving mechanism, latitudinal coverage, depth extent and structure. For this thesis a thorough analysis of the physical mechanisms controlling the formation and braking of zonal winds in stably stratified and semi-conducting regions was performed, yielding the following results:

- Stably stratified layers (SSL) lead to the decay of zonal flows penetrating down from a convective region. Unlike other potential braking mechanisms such as viscous stresses, at a rigid lower boundary, or Maxwell stresses due to increasing conductivity, a SSL does not prevent strong zonal winds from forming in the overlying convective envelope.
- A higher degree of stable stratification, characterised by the ratio of the Brunt-Väisälä frequency and rotation,  $N/\Omega$  leads to a more efficient quenching of the zonal winds. Wider jets penetrate further into the SSL than narrower jets.
- In the overlying convective region the wind structure is cylindrical and the jets continue downwards invariant along the rotation axis. Upon reaching the SSL, they are not only attenuated in amplitude, but the structure also becomes more radially aligned.
- Magnetic effects lead to a shorter penetration depth of the zonal winds into the stable layer. The rate of decay is dependent on  $\sigma B^2$ , where  $\sigma$  is the electrical conductivity and  $B$  is the magnetic field strength, which we have characterised using the internal axial dipole field.
- Larger values of  $\sigma B^2$  at the upper boundary of the SSL lead to diminished zonal flows at the surface as the convective envelope is incompletely decoupled from the conducting region below. If  $\sigma B^2$  is sufficiently small in the transition region, zonal winds are maintained at the higher latitudes.
- A zonal wind balance governs the attenuation of zonal flows in the SSL. This is initiated when the Coriolis force must balance forces arising from Reynolds stresses as convection is quenched at the SSL boundary. If there is increasing conductivity and a strong internal magnetic field, Coriolis forces are also required in this deeper part of the SSL, to balance Lorentz forces. This additional induced meridional flow leads to stronger latitudinal entropy fluctuations, braking the jets even more efficiently.

## 4.1 Depth and Extent of Stably Stratified Layer

Neither study sought to emulate either planet directly, in terms of density or transport property profiles for example. Nevertheless, the results from this generalised approach can be used to draw conclusions with regards to the outer regions of both Jupiter and Saturn.

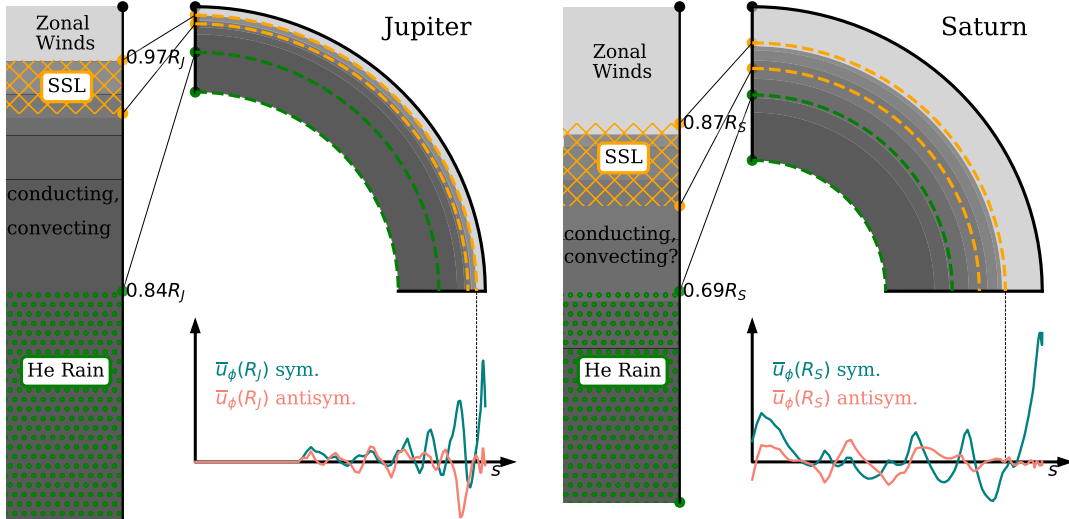


**Figure 4.1.** Schematic of proposed interior structures for Jupiter (left) and Saturn (right). Grey shading indicates electrical conductivity (as in Fig. 1.3), where the outer region is non-conducting;  $\sigma < 1\text{S/m}$ . A deep helium rain region is indicated in green. A suggested shallower stably stratified layer is indicated in orange, where the given upper boundary is given by zonal wind depths inferred from gravity measurements. The tangent cylinder attached to this boundary is marked, with the surface zonal wind profiles as a function of  $s$  given for reference. They are shown decomposed into their equatorially (anti)symmetric parts.

### Depth of Stably Stratified Layer

The extent of the outer convective region, where the zonal winds extend geostrophically downwards, has already been constrained by the gravity moment analysis, as described in Section 1.2.1. Our results suggest that this is the main indicator as to the upper boundary of the stably stratified layer, responsible for the onset of zonal wind braking. Models with strong zonal flows consistently show that zonal wind decay is only initiated at the SSL boundary. Furthermore, the constraint that equatorially antisymmetric components of the zonal winds should be restricted to inside the Tangent Cylinder, TC, (see Fig. 1.14) as jets outside the TC must be transhemispheric, also suggests a lower bound to the depth of the convective region. Fig. 4.1 shows the agreement between these two restrictions. The schematic indicates a suggested structure of the outer interiors of Jupiter and Saturn. The upper boundary of the stable layer is located at the inferred depths of the zonal winds

(Galanti and Kaspi 2020) and the respective equatorially symmetric and antisymmetric zonal wind profiles show that the flow outside this TC is predominantly symmetric. This is primarily useful for Jupiter, with its strong prograde jet at around 25°N where such a strong discontinuity at the equator must be accounted for.

### Extent of Stably Stratified Layer

The thickness of a shallow stably stratified region is more difficult to constrain than its upper boundary.

In the case of Jupiter the layer cannot be too thick as the magnetic field will otherwise be too axisymmetrised due to the magnetic skin effect. A thin layer could lead to incomplete decoupling from the conducting region below which may account for Jupiter's weaker high-latitude jets, compared to Saturn (see Fig. 2.4 and 3.3). Gastine and Wicht (2021) point out that for the stable layer to quench convection effectively, it should be at least as thick as the penetration depth of the convective eddies. This is dependent on the degree of stratification (e.g. Takehiro and Lister (2001), Dietrich and Wicht (2018), also discussed in Section 2.3.1):

$$\delta = (N/\Omega)^{-1} d_c \quad (4.1)$$

where  $\delta$  is the penetration distance and  $d_c$  is the characteristic length scale of the convective eddy. Therefore, a thin layer could still attenuate both convection and the zonal winds effectively if  $N/\Omega$  is large. Meanwhile, the magnetic skin effect is independent of the degree of stratification (see Stevenson (1982), for example) so this would not have an adverse affect on the magnetic field.

On Saturn we have an opposite constraint. As described in Section 1.2.5, its magnetic field is extraordinarily axisymmetric. Therefore, the stable stratification must reach far into the conducting region, leading to a sufficient magnetic skin effect. Some estimates are given in Christensen et al. (2018), Cao et al. (2020), for example, although the minimum thickness is dependent on the magnetic diffusivity. A shallower stable layer, in a region with higher magnetic diffusivity, must be thicker to attenuate the dipole tilt by the same degree. It is even possible that there is no magnetoconvection between the helium rain region and the stable layer responsible for quenching the zonal flow. Whether a model with stable stratification spanning such a large part of the planet can produce a Saturn-like magnetic field likely depends on the extent of dynamo region. If a potential dilute core leads to stable stratification below, this would imply only a fairly thin region is left for dynamo action to take place.

In both planets the presence of a shallow stably stratified region also compels us to reevaluate our estimates of the dynamo radii. They are currently estimated to be 81-83%  $R_J$  (Connerney et al. 2022, Sharan et al. 2022) and 75%  $R_S$  (Dougherty et al. 2018), respectively, so both below our suggested upper boundary of stable stratification. Depending on how much overlap the layer has with the conducting region, we must reexamine how the measured surface fields are extrapolated downwards.

### Nature of Stably Stratified Layer

The discussion of the current understanding of the gas giants' interiors (Section 1.2) illustrated that these models indicate onset of hydrogen-helium immiscibility at around  $0.84R_J$

and  $0.69R_S$ , respectively. Clearly this is much too deep to be reached by zonal winds in both Jupiter and Saturn. Therefore, current models suggest we cannot hold stratification due to helium rain accountable for braking the zonal winds.

Not knowing the origin of this shallow stable stratification and whether it is compositional or thermal, means that it is challenging to estimate its degree of stability  $N/\Omega$ .

## 4.2 Downward Continuation of Zonal Winds

Our study has some consequences when we consider how gravity moments have previously been used to estimate the depth of the zonal winds on both Jupiter and Saturn. Galanti et al. (2021) have already explored a variety of ways to extrapolate the surface winds of the Gas Giants into their interiors and show that immediately below the surface they must continue geostrophically downwards, as a fully convecting region would demand. Our results show that this may not be appropriate where jet-attenuation begins. As shown by Dietrich et al. (2021), Fig. 10, a significant part of the wind-related gravity signal is formed in the region where the amplitude of the jets decreases, where it contributes with an opposite sign compared to the shallower regions. Unless the jets drop off on a short length scale, the difference between a radial and a geostrophic extension may have a significant influence on the gravity signal and should be taken into account in future studies of wind-related gravity. In a similar vein, the assumption of the same attenuation function for all jets irrespective of their width in the gravity study is also questionable, since the penetration distance into a stable layer is proportional to their latitudinal width. The jets observed on both planets' surfaces vary considerably in latitude and have very different length-scales if projected onto a SSL boundary at a specific depth.

## 4.3 Further Work

Suggestions for further work include:

- Imposing a more complex magnetic field at the inner shell boundary. It is not clear if a field that has a tilted dipole or is more small-scaled may influence the damping of the winds differently.
- Investigating the possible thickness of the stably stratified layer by modelling a sandwich layer. This could help constrain the extent of the stable stratification by analysing how different stable layer thicknesses effect both the zonal winds and the magnetic fields at the surface.
- Exploring the effect of the Ekman number. Driving down the Ekman number by at least one order of magnitude with a preferred model from the study described in Chapter 2 would help us to gauge what effect our enhanced viscosity has.

This work will also be invaluable when attempting to simulate the dynamo region. The two studies provide guidance on the strength of the stable layer and its depth, relative to

Jupiter or Saturn's electrical conductivity profile. Implementing it will affect the magnetic field morphology at the surface, helping to evaluate the model's similarities with the gas giants' measured magnetic fields.



# Bibliography

- A. Adriani, A. Mura, G. Orton, C. Hansen, F. Altieri, M. Moriconi, J. Rogers, G. Eichstädt, T. Momary, A. Ingersoll, G. Filacchione, G. Sindoni, F. Tabataba-Vakili, B. Dinelli, F. Fabiano, S. Bolton, J. Connerney, S. Atreya, J. Lunine, and M. Amoroso. Clusters of cyclones encircling Jupiter's poles. *Nature*, 555:216–219, 2018. doi: 10.1038/nature25491.
- A. Antuñano, T. del Río-Gaztelurrutia, A. Sánchez-Lavega, and R. Hueso. Dynamics of Saturn's polar regions. *Journal of Geophysical Research: Planets*, 120(2):155–176, 2015. doi: <https://doi.org/10.1002/2014JE004709>.
- J. M. Aurnou and M. Heimpel. Zonal jets in rotating convection with mixed mechanical boundary conditions. *Icarus*, 169:492–498, 2004.
- J. M. Aurnou and P. L. Olson. Strong zonal winds from thermal convection in a rotating spherical shell. *Geophysical Research Letters*, 28(13):2557–2559, 2001. doi: <https://doi.org/10.1029/2000GL012474>.
- K. H. Baines, T. W. Momary, L. N. Fletcher, A. P. Showman, M. Roos-Serote, R. H. Brown, B. J. Buratti, R. N. Clark, and P. D. Nicholson. Saturn's north polar cyclone and hexagon at depth revealed by Cassini/VIMS. *Planetary and Space Science*, 57(14):1671–1681, 2009. doi: <https://doi.org/10.1016/j.pss.2009.06.026>.
- R. F. Beebe, A. P. Ingersoll, G. E. Hunt, J. L. Mitchell, and J. P. Müller. Measurements of wind vectors, eddy momentum transports, and energy conversions in Jupiter's atmosphere from Voyager 1 images. *Geophysical Research Letters*, 7(1):1–4, 1980. doi: <https://doi.org/10.1029/GL007i001p00001>.
- J. Bloxham, K. M. Moore, L. Kulowski, H. Cao, R. K. Yadav, D. J. Stevenson, J. E. P. Connerney, and S. J. Bolton. Differential rotation in Jupiter's interior revealed by simultaneous inversion for the magnetic field and zonal flux velocity. *Journal of Geophysical Research: Planets*, 127(5):e2021JE007138, 2022. doi: <https://doi.org/10.1029/2021JE007138>.
- S. I. Braginsky and P. H. Roberts. Equations governing convection in Earth's core and the geodynamo. *Geophysical and Astrophysical Fluid Dynamics*, 79:1–97, 1995. doi: 10.1080/03091929508228992.
- S. Brygoo, P. Loubeyre, M. Millot, J. Rygg, P. Celliers, J. Eggert, Raymond Jeanloz, and G. Collins. Evidence of hydrogen-helium immiscibility at Jupiter-interior conditions. *Nature*, 593:517–521, 2021. doi: 10.1038/s41586-021-03516-0.

## Bibliography

---

- F. H. Busse. Thermal instabilities in rapidly rotating systems. *Journal of Fluid Mechanics*, 44(3):441–460, 1970. doi: 10.1017/S0022112070001921.
- F. H. Busse. A simple model of convection in the jovian atmosphere. *Icarus*, 29(2): 255–260, 1976. doi: [https://doi.org/10.1016/0019-1035\(76\)90053-1](https://doi.org/10.1016/0019-1035(76)90053-1).
- F. H. Busse and R. D. Simitev. Quasi-geostrophic approximation of anelastic convection. *Journal of Fluid Mechanics*, 751:216–227, 2014. doi: 10.1017/jfm.2014.293.
- S. Cabanes, J. M. Aurnou, B. Favier, and M. Le Bars. A laboratory model for deep-seated jets on the gas giants. *Nature Physics*, 13:387–390, 2017.
- H. Cao and D. J. Stevenson. Zonal flow magnetic field interaction in the semi-conducting region of giant planets. *Icarus*, 296:59–72, 2017. doi: 10.1016/j.icarus.2017.05.015.
- H. Cao and D. J. Stevenson. Gravity and zonal flows of giant planets: From the euler equation to the thermal wind equation. *Journal of Geophysical Research: Planets*, 122 (4):686–700, 2017. doi: <https://doi.org/10.1002/2017JE005272>.
- H. Cao, M. K. Dougherty, G. J. Hunt, G. Provan, S. W. H. Cowley, E. J. Bunce, S. Kellock, and D. J. Stevenson. The landscape of Saturn’s internal magnetic field from the Cassini grand finale. *Icarus*, 344:113541, 2020. doi: <https://doi.org/10.1016/j.icarus.2019.113541>.
- R. Chemke and Y. Kaspi. Poleward migration of eddy driven jets. *Journal of Advances in Modeling Earth Systems*, 7, 2015. doi: 10.1002/2015MS000481.
- U. Christensen. Zonal flow driven by strongly supercritical convection in rotating spherical shells. *Journal of Fluid Mechanics*, 470:115 – 133, 2002. doi: 10.1017/S0022112002002008.
- U. R. Christensen. Zonal flow driven by deep convection in the major planets. *Geophys. Res. Lett.*, 28(13):2553–2556, 2001. doi: 10.1029/2000GL012643.
- U. R. Christensen and J. Wicht. Models of magnetic field generation in partly stable planetary cores: Applications to Mercury and Saturn. *Icarus*, 196(1):16–34, 2008. doi: <https://doi.org/10.1016/j.icarus.2008.02.013>.
- U. R. Christensen and J. Wicht. 8.10 Numerical Dynamo Simulations. In *Treatise on Geophysics*, 2nd edn. (ed. Schubert, G.), page 245–277. Elsevier, 2015.
- U. R. Christensen, H. Cao, M. K. Dougherty, and K. Khurana. *Saturn’s Magnetic Field and Dynamo*, page 69–96. Cambridge Planetary Science. Cambridge University Press, 2018. doi: 10.1017/9781316227220.004.
- U. R. Christensen, J. Wicht, and W. Dietrich. Mechanisms for Limiting the Depth of Zonal Winds in the Gas Giant Planets. *ApJ*, 890:61, 2020. doi: 10.3847/1538-4357/ab698c.

- J. E. P. Connerney, S. Kotsiaros, R. J. Oliversen, J. R. Espley, J. L. Joergensen, P. S. Joergensen, J. M. G. Merayo, M. Herceg, J. Bloxham, K. M. Moore, S. J. Bolton, and S. M. Levin. A new model of Jupiter's magnetic field from Juno's first nine orbits. *Geophysical Research Letters*, 45(6):2590–2596, 2018. doi: <https://doi.org/10.1002/2018GL077312>.
- J. E. P. Connerney, S. Timmins, R. J. Oliversen, J. R. Espley, J. L. Joergensen, S. Kotsiaros, P. S. Joergensen, J. M. G. Merayo, M. Herceg, J. Bloxham, K. M. Moore, A. Mura, A. Moirano, S. J. Bolton, and S. M. Levin. A new model of Jupiter's magnetic field at the completion of Juno's prime mission. *Journal of Geophysical Research: Planets*, 127(2):e2021JE007055, 2022. doi: <https://doi.org/10.1029/2021JE007055>.
- F. Debras and G. Chabrier. New models of Jupiter in the context of Juno and Galileo. *The Astrophysical Journal*, 872(1):100, 2019. doi: 10.3847/1538-4357/aaff65.
- F. Debras, G. Chabrier, and D. J. Stevenson. Superadiabaticity in Jupiter and giant planet interiors. *The Astrophysical Journal Letters*, 913(2):L21, 2021. doi: 10.3847/2041-8213/abfdcc.
- A. D. Del Genio and J. M. Barbara. Constraints on Saturn's tropospheric general circulation from Cassini iss images. *Icarus*, 219:689–700, 2012. doi: 10.1016/j.icarus.2012.03.035.
- J. W. Dewberry, C. R. Mankovich, J. Fuller, D. Lai, and W. Xu. Constraining Saturn's interior with ring seismology: Effects of differential rotation and stable stratification. *The Planetary Science Journal*, 2, 2021.
- W. Dietrich and C. A. Jones. Anelastic spherical dynamos with radially variable electrical conductivity. *Icarus*, 305:15–32, 2018. doi: 10.1016/j.icarus.2018.01.003.
- W. Dietrich and J. Wicht. Penetrative convection in partly stratified rapidly rotating spherical shells. *Frontiers in Earth Science*, 6, 2018. doi: 10.3389/feart.2018.00189.
- W. Dietrich, P. Wulff, J. Wicht, and U. R. Christensen. Linking zonal winds and gravity – II. Explaining the equatorially antisymmetric gravity moments of Jupiter. *Monthly Notices of the Royal Astronomical Society*, 505(3):3177–3191, 2021.
- M. K. Dougherty, H. Cao, K. K. Khurana, G. J. Hunt, G. Provan, S. Kellock, M. E. Burton, T. A. Burk, E. J. Bunce, S. W. H. Cowley, M. G. Kivelson, C. T. Russell, and D. J. Southwood. Saturn's magnetic field revealed by the Cassini grand finale. *Science*, 362(6410):eaat5434, 2018. doi: 10.1126/science.aat5434.
- R. M. Dreizler and E. K. U. Gross. *Density Functional Theory*. Springer, 1990.
- L. D. V. Duarte, T. Gastine, and J. Wicht. Anelastic dynamo models with variable electrical conductivity: An application to gas giants. *Physics of the Earth and Planetary Interiors*, 222:22–34, 2013. doi: 10.1016/j.pepi.2013.06.010.
- L. D. V. Duarte, J. Wicht, and T. Gastine. Physical conditions for Jupiter-like dynamo models. *Icarus*, 299:206–221, 2018. doi: <https://doi.org/10.1016/j.icarus.2017.07.016>.

## Bibliography

---

- K. Duer, N. Gavriel, E. Galanti, Y. Kaspi, . N. Fletcher, T. Guillot, S. J. Bolton, S. M. Levin, S. K. Atreya, D. Grassi, A. P. Ingersoll, C. Li, L. Li, J. I. Lunine, G. S. Orton, F. A. Oyafuso, and J. H. Waite. Evidence for multiple ferrel-like cells on Jupiter. *Geophysical Research Letters*, 48(23):e2021GL095651, 2021. doi: <https://doi.org/10.1029/2021GL095651>.
- D. Durante, M. Parisi, D. Serra, M. Zannoni, V. Notaro, P. Racioppa, D. R. Buccino, G. Lari, L. Gomez Casajus, L. Iess, W. M. Folkner, G. Tommei, P. Tortora, and S. J. Bolton. Jupiter's gravity field halfway through the Juno mission. *Geophysical Research Letters*, 47(4):e2019GL086572, 2020. doi: <https://doi.org/10.1029/2019GL086572>.
- L. Fletcher, Y. Kaspi, T. Guillot, and A. Showman. How well do we understand the belt/zone circulation of giant planet atmospheres? *Space science reviews*, 216:30, 2020. doi: 10.1007/s11214-019-0631-9.
- L. Fletcher, F. Oyafuso, M. Allison, A. Ingersoll, Liming Li, Yohai Kaspi, Eli Galanti, Michael Wong, Glenn Orton, Keren Duer, Z. Zhang, C. Li, T. Guillot, S. Levin, and S. Bolton. Jupiter's temperate belt/zone contrasts revealed at depth by Juno microwave observations. *Journal of Geophysical Research: Planets*, 126, 2021. doi: 10.1029/2021JE006858.
- J. Fortney, B. Militzer, C. Mankovich, R. Helled, S. Wahl, N. Nettelmann, W. Hubbard, D. Stevenson, L. Iess, M. Marley, and N. Movshovitz. *Saturn's Interior After the Cassini Grand Finale*. Cambridge University Press, 2023.
- M. French, A. Becker, W. Lorenzen, N. Nettelmann, M. Bethkenhagen, J. Wicht, and R. Redmer. Ab initio simulations for material properties along the Jupiter adiabat. *The Astrophysical Journal Supplement Series*, 202(1):5, 2012. doi: 10.1088/0067-0049/202/1/5.
- E. Galanti and Y. Kaspi. Combined magnetic and gravity measurements probe the deep zonal flows of the gas giants. *Monthly Notices of the Royal Astronomical Society*, 501, 2020. doi: 10.1093/mnras/staa3722.
- E. Galanti, Y. Kaspi, and E. Tziperman. A full, self-consistent treatment of thermal wind balance on oblate fluid planets. *Journal of Fluid Mechanics*, 810:175–195, 2017. doi: 10.1017/jfm.2016.687.
- E. Galanti, Y. Kaspi, Y. Miguel, T. Guillot, D. Durante, P. Racioppa, and L. Iess. Saturn's Deep Atmospheric Flows Revealed by the Cassini Grand Finale Gravity Measurements. *Geophysical Research Letters*, 46:616–624, 2019. doi: 10.1029/2018GL078087.
- E. Galanti, Y. Kaspi, K. Duer, L. Fletcher, A. P. Ingersoll, C. Li, G. S. Orton, T. Guillot, S. M. Levin, and S. J. Bolton. Constraints on the latitudinal profile of Jupiter's deep jets. *Geophysical Research Letters*, 48(9):e2021GL092912, 2021. doi: <https://doi.org/10.1029/2021GL092912>.
- E. García-Melendo, S. Pérez-Hoyos, A. Sánchez-Lavega, and R. Hueso. Saturn's zonal wind profile in 2004–2009 from Cassini ISS images and its long-term variability. *Icarus*, 215(1):62–74, 2011. doi: <https://doi.org/10.1016/j.icarus.2011.07.005>.

- T. Gastine and J. Wicht. Effects of compressibility on driving zonal flow in gas giants. *Icarus*, 219(1):428–442, 2012. doi: 10.1016/j.icarus.2012.03.018.
- T. Gastine and J. Wicht. Stable stratification promotes multiple zonal jets in a turbulent jovian dynamo model. *Icarus*, 2021. doi: 10.1016/j.icarus.2021.114514.
- T. Gastine, J. Wicht, and J. M. Aurnou. Zonal flow regimes in rotating anelastic spherical shells: An application to giant planets. *Icarus*, 225(1):156–172, 2013. doi: <https://doi.org/10.1016/j.icarus.2013.02.031>.
- T. Gastine, M. Heimpel, and J. Wicht. Zonal flow scaling in rapidly-rotating compressible convection. *Physics of the Earth and Planetary Interiors*, 232:36–50, 2014. doi: <https://doi.org/10.1016/j.pepi.2014.03.011>.
- T. Gastine, J. Aubert, and A. Fournier. Dynamo-based limit to the extent of a stable layer atop Earth’s core. *Geophysical Journal International*, 222(2):1433–1448, 2020. doi: 10.1093/gji/ggaa250.
- G. A. Glatzmaier. Numerical simulations of stellar convective dynamos. i. the model and method. *Journal of Computational Physics*, 55(3):461–484, 1984. doi: [https://doi.org/10.1016/0021-9991\(84\)90033-0](https://doi.org/10.1016/0021-9991(84)90033-0).
- T. Guillot and D. Gautier. Giant planets. In *Treatise on Geophysics*, pages 529–557. Elsevier, 2015. doi: 10.1016/b978-0-444-53802-4.00176-7.
- T. Guillot, L. Fletcher, R. Helled, M. Ikoma, M. Line, and V. Parmentier. *Giant Planets from the Inside-Out*. 2022.
- M. Hedman and P. Nicholson. Kronoseismology: Using density waves in Saturn’s c ring to probe the planet’s interior. *The Astronomical Journal*, 146, 2013. doi: 10.1088/0004-6256/146/1/12.
- M. Heimpel and J. Aurnou. Turbulent convection in rapidly rotating spherical shells: A model for equatorial and high latitude jets on Jupiter and Saturn. *Icarus*, 187(2):540–557, 2007. doi: <https://doi.org/10.1016/j.icarus.2006.10.023>.
- M. Heimpel and N. Gómez-Pérez. On the relationship between zonal jets and dynamo action in giant planets. *Geophysical Research Letters*, 38(14), 2011. doi: <https://doi.org/10.1029/2011GL047562>.
- M. Heimpel, J. Aurnou, and J. Wicht. Simulation of equatorial and high-latitude jets on Jupiter in a deep convection model. *Nature*, 438:193–6, 2005. doi: 10.1038/nature04208.
- M. Heimpel, T. Gastine, and J. Wicht. Simulation of deep-seated zonal jets and shallow vortices in gas giant atmospheres. *Nature Geoscience*, 9(1):19–23, 2016. doi: 10.1038/ngeo2601.
- M. H. Heimpel, R. K. Yadav, N. A. Featherstone, and J. M. Aurnou. Polar and mid-latitude vortices and zonal flows on Jupiter and Saturn. *Icarus*, 379:114942, 2022. doi: <https://doi.org/10.1016/j.icarus.2022.114942>.

## Bibliography

---

- R. Helled. The interiors of Jupiter and Saturn. *Oxford Art Journal*, 2019.
- R. Helled and T. Guillot. *Internal Structure of Giant and Icy Planets: Importance of Heavy Elements and Mixing*. Springer International Publishing, 2018. doi: 10.1007/978-3-319-30648-3\_44-2.
- W. B. Hubbard. High-precision maclaurin-based models of rotating liquid planets. *The Astrophysical Journal Letters*, 756(1):L15, 2012. doi: 10.1088/2041-8205/756/1/L15.
- W. B. Hubbard. Concentric maclaurin spheroid models of rotating liquid planets. *The Astrophysical Journal*, 768(1):43, 2013. doi: 10.1088/0004-637X/768/1/43.
- W. B. Hubbard and B. Militzer. A Preliminary Jupiter Model. *ApJ*, 820(1):80, 2016. doi: 10.3847/0004-637X/820/1/80.
- L. Iess, W. Folkner, D. Durante, M. Parisi, Y. Kaspi, E. Galanti, T. Guillot, W. Hubbard, D. Stevenson, J. Anderson, D. Buccino, L. Casajus, A. Milani, R. Park, P. Racioppa, D. Serra, P. Tortora, M. Zannoni, H. Cao, and S. Bolton. Measurement of Jupiter's asymmetric gravity field. *Nature*, 555:220–222, 2018. doi: 10.1038/nature25776.
- L. Iess, B. Militzer, Y. Kaspi, P. Nicholson, D. Durante, P. Racioppa, A. Anabtawi, E. Galanti, W. Hubbard, M. J. Mariani, P. Tortora, S. Wahl, and M. Zannoni. Measurement and implications of Saturn's gravity field and ring mass. *Science*, 364(6445):eaat2965, 2019. doi: 10.1126/science.aat2965.
- A. P. Ingersoll and D. Pollard. Motion in the interiors and atmospheres of Jupiter and Saturn: scale analysis, anelastic equations, barotropic stability criterion. *Icarus*, 52(1):62–80, 1982. doi: 10.1016/0019-1035(82)90169-5.
- A. P. Ingersoll, R. F. Beebe, J. L. Mitchell, G. W. Garneau, G. M. Yagi, and J. P. Müller. Interaction of eddies and mean zonal flow on Jupiter as inferred from Voyager 1 and 2 images. *Journal of Geophysical Research: Space Physics*, 86(A10):8733–8743, 1981. doi: <https://doi.org/10.1029/JA086iA10p08733>.
- C. A. Jones and K. M. Kuzanyan. Compressible convection in the deep atmospheres of giant planets. *Icarus*, 204(1):227–238, 2009. doi: <https://doi.org/10.1016/j.icarus.2009.05.022>.
- C. A. Jones, K. M. Kuzanyan, and R. H. Mitchell. Linear theory of compressible convection in rapidly rotating spherical shells, using the anelastic approximation. *Journal of Fluid Mechanics*, 634:291–319, 2009. doi: 10.1017/S0022112009007253.
- C. A. Jones, P. Boronski, S. Brun, G. A. Glatzmaier, T. Gastine, M. Miesch, and J. Wicht. Anelastic convection-driven dynamo benchmarks. *Icarus*, 216, 2011. doi: 10.1016/j.icarus.2011.08.014.
- Y. Kaspi. Inferring the depth of the zonal jets on Jupiter and Saturn from odd gravity harmonics. *Geophysical Research Letters*, 40(4):676–680, 2013. doi: <https://doi.org/10.1029/2012GL053873>.

- Y. Kaspi, G. Flierl, and A. Showman. The deep wind structure of the giant planets: Results from an anelastic general circulation model. *Icarus*, 202:525–542, 2009. doi: 10.1016/j.icarus.2009.03.026.
- Y. Kaspi, J. E. Davighi, E. Galanti, and W. B. Hubbard. The gravitational signature of internal flows in giant planets: Comparing the thermal wind approach with barotropic potential-surface methods. *Icarus*, 276:170–181, 2016. doi: <https://doi.org/10.1016/j.icarus.2016.04.001>.
- Y. Kaspi, E. Galanti, W. B. Hubbard, D. J. Stevenson, S. J. Bolton, L. Iess, T. Guillot, J. Bloxham, J. E. P. Connerney, H. Cao, D. Durante, W. M. Folkner, R. Helled, A. P. Ingersoll, S. M. Levin, J. I. Lunine, Y. Miguel, B. Militzer, M. Parisi, and S. M. Wahl. Jupiter’s atmospheric jet streams extend thousands of kilometres deep. *Nature*, 555: 223–226, 2018. doi: 10.1038/nature25793.
- Y. Kaspi, E. Galanti, A. Showman, D. Stevenson, T. Guillot, L. Iess, and S. Bolton. Comparison of the deep atmospheric dynamics of Jupiter and Saturn in light of the Juno and Cassini gravity measurements. *Space Science Reviews*, 216, 2020. doi: 10.1007/s11214-020-00705-7.
- D. Kong, K. Zhang, and G. Schubert. Odd gravitational harmonics of Jupiter: Effects of spherical versus nonspherical geometry and mathematical smoothing of the equatorially antisymmetric zonal winds across the equatorial plane. *Icarus*, 277:416–423, 2016. doi: <https://doi.org/10.1016/j.icarus.2016.05.037>.
- D. Kong, K. Zhang, G. Schubert, and J. D. Anderson. Origin of Jupiter’s cloud-level zonal winds remains a puzzle even after Juno. *Proceedings of the National Academy of Sciences*, 115(34):8499–8504, 2018. doi: 10.1073/pnas.1805927115.
- D. Lai. Jupiter’s dynamical love number. *The Planetary Science Journal*, 2(4):122, jul 2021. doi: 10.3847/psj/ac013b.
- D. Lemassquerier, B. Favier, and M. Le Bars. Zonal jets at the laboratory scale: hysteresis and rossby waves resonance. *Journal of Fluid Mechanics*, 910:A18, 2021. doi: 10.1017/jfm.2020.1000.
- J. Liu, P. Goldreich, and D. Stevenson. Constraints on deep-seated zonal winds inside Jupiter and Saturn. *Icarus*, 196:597–615, 2008. doi: 10.1016/j.icarus.2007.11.036.
- W. Lorenzen, B. Holst, and R. Redmer. Metallization in hydrogen-helium mixtures. *Phys. Rev. B*, 84:235109, 2011. doi: 10.1103/PhysRevB.84.235109.
- C. Mankovich and J. Fuller. A diffuse core in Saturn revealed by ring seismology. *Nature Astronomy*, 5, 2021. doi: 10.1038/s41550-021-01448-3.
- C. Mankovich, M. S. Marley, J. J. Fortney, and N. Movshovitz. Cassini ring seismology as a probe of Saturn’s interior. I. rigid rotation. *The Astrophysical Journal*, 871(1):1, 2019. doi: 10.3847/1538-4357/aaf798.

## Bibliography

---

- C. R. Mankovich. Saturn's rings as a seismograph to probe Saturn's internal structure. *AGU Advances*, 1(2):e2019AV000142, 2020. doi: <https://doi.org/10.1029/2019AV000142>.
- J. May, T.D. Carr, and M.D. Desch. Decametric radio measurement of Jupiter's rotation period. *Icarus*, 40(1):87–93, 1979. doi: [https://doi.org/10.1016/0019-1035\(79\)90055-1](https://doi.org/10.1016/0019-1035(79)90055-1).
- Miguel, Y., Bazot, M., Guillot, T., Howard, S., Galanti, E., Kaspi, Y., Hubbard, W. B., Militzer, B., Helled, R., Atreya, S. K., Connerney, J. E. P., Durante, D., Kulowski, L., Lunine, J. I., Stevenson, D., and Bolton, S. Jupiter's inhomogeneous envelope. *A&A*, 662:A18, 2022. doi: [10.1051/0004-6361/202243207](https://doi.org/10.1051/0004-6361/202243207).
- B. Militzer and W. Hubbard. Relation of gravity, winds, and the moment of inertia of Jupiter and Saturn. *The Planetary Science Journal*, 4:95, 2023. doi: [10.3847/PSJ/acd2cd](https://doi.org/10.3847/PSJ/acd2cd).
- B. Militzer, F. Soubiran, . M. Wahl, and W. Hubbard. Understanding Jupiter's interior. *Journal of Geophysical Research: Planets*, 121(9):1552–1572, 2016. doi: <https://doi.org/10.1002/2016JE005080>.
- B. Militzer, S. Wahl, and W. B. Hubbard. Models of Saturn's Interior Constructed with an Accelerated Concentric Maclaurin Spheroid Method. *ApJ*, 879(2):78, 2019. doi: [10.3847/1538-4357/ab23f0](https://doi.org/10.3847/1538-4357/ab23f0).
- B. Militzer, W. B. Hubbard, S. Wahl, J. I. Lunine, E. Galanti, Y. Kaspi, Y. Miguel, T. Guillot, K. M. Moore, M. Parisi, J. E. P. Connerney, R. Helled, H. Cao, C. Mankovich, D. J. Stevenson, R. S. Park, M. Wong, S. K. Atreya, J. Anderson, and S. J. Bolton. Juno spacecraft measurements of Jupiter's gravity imply a dilute core. *The Planetary Science Journal*, 3(8):185, 2022. doi: [10.3847/PSJ/ac7ec8](https://doi.org/10.3847/PSJ/ac7ec8).
- K. Moore, H. Cao, J. Bloxham, D. Stevenson, J. Connerney, and S. Bolton. Time-variation of Jupiter's internal magnetic field consistent with zonal wind advection. *Nature Astronomy*, 05 2019.
- K. M Moore, R. K. Yadav, L. Kulowski, H. Cao, J. Bloxham, J. E. P. Connerney, S. Kotiaros, J. L Jørgensen, J. M. G. Merayo, D. J. Stevenson, S. J. Bolton, and S. M. Levin. A complex dynamo inferred from the hemispheric dichotomy of Jupiter's magnetic field. *Nature*, 561(7721):76—78, 2018. doi: [10.1038/s41586-018-0468-5](https://doi.org/10.1038/s41586-018-0468-5).
- K. M. Moore, A. Barik, S. Stanley, D. J. Stevenson, N. Nettelmann, R. Helled, T. Guillot, B. Militzer, and S. Bolton. Dynamo simulations of Jupiter's magnetic field: The role of stable stratification and a dilute core. *Journal of Geophysical Research: Planets*, 127(11):e2022JE007479, 2022. doi: <https://doi.org/10.1029/2022JE007479>.
- M. A. Morales, S. Hamel, K. Caspersen, and E. Schwegler. Hydrogen-helium demixing from first principles: From diamond anvil cells to planetary interiors. *Phys. Rev. B*, 87 (17):174105, 2013. doi: [10.1103/PhysRevB.87.174105](https://doi.org/10.1103/PhysRevB.87.174105).

- N. F. Ness, M. H. Acuña, R. P. Lepping, J. E. P. Connerney, K. W. Behannon, L. F. Burlaga, and F. M. Neubauer. Magnetic field studies by Voyager 1: Preliminary results at Saturn. *Science*, 212(4491):211–217, 1981. doi: 10.1126/science.212.4491.211.
- N. F. Ness, M. H. Acuña, K. W. Behannon, L. F. Burlaga, J. E. P. Connerney, R. P. Lepping, and F. M. Neubauer. Magnetic field studies by Voyager 2: Preliminary results at Saturn. *Science*, 215(4532):558–563, 1982. doi: 10.1126/science.215.4532.558.
- N. Nettelmann, A. Becker, B. Holst, and R. Redmer. Jupiter Models with Improved Ab Initio Hydrogen Equation of State (H-REOS.2). *ApJ*, 750(1):52, 2012. doi: 10.1088/0004-637X/750/1/52.
- N. Nettelmann, R. Püstow, and R. Redmer. Saturn layered structure and homogeneous evolution models with different eos. *Icarus*, 225(1):548–557, 2013. doi: <https://doi.org/10.1016/j.icarus.2013.04.018>.
- N. Nettelmann, N. Movshovitz, D. Ni, J. J. Fortney, E. Galanti, Y. Kaspi, R. Helled, C. R. Mankovich, and S. Bolton. Theory of figures to the seventh order and the interiors of Jupiter and Saturn. *The Planetary Science Journal*, 2(6):241, 2021. doi: 10.3847/psj/ac390a.
- G. S. Orton, C. Hansen, M. Caplinger, M. Ravine, S. Atreya, A. P. Ingersoll, E. Jensen, T. Momary, L. Lipkaman, D. Krysak, R. Zimdar, and S. Bolton. The first close-up images of Jupiter’s polar regions: Results from the Juno mission JunoCam instrument. *Geophysical Research Letters*, 44(10):4599–4606, 2017. doi: <https://doi.org/10.1002/2016GL072443>.
- M. Parisi, Y. Kaspi, E. Galanti, D. Durante, S. J. Bolton, S. M. Levin, D. R. Buccino, L. N. Fletcher, W. M. Folkner, T. Guillot, R. Helled, L. Iess, C. Li, K. Oudrhiri, and M. H. Wong. The depth of Jupiter’s great red spot constrained by Juno gravity overflights. *Science*, 374(6570):964–968, 2021. doi: 10.1126/science.abf1396.
- C. C. Porco, R. A. West, A. McEwen, A. D. Del Genio, A. P. Ingersoll, P. Thomas, S. Squyres, L. Dones, C. D. Murray, and T. V. Johnson. Cassini Imaging of Jupiter’s Atmosphere, Satellites, and Rings. *Science*, 299(5612):1541–1547, 2003. doi: 10.1126/science.1079462.
- P. Read, R. Young, and D. Kennedy. The turbulent dynamics of Jupiter’s and Saturn’s weather layers: order out of chaos? *Geoscience Letters*, 7, 2020. doi: 10.1186/s40562-020-00159-3.
- P. L. Read, A. Antuñano, S. Cabanes, G. Colyer, T. Gaztelurrutia, and A. Sanchez-Lavega. Energy exchanges in Saturn’s polar regions from Cassini observations: Eddy-zonal flow interactions. *Journal of Geophysical Research: Planets*, 127(5):e2021JE006973, 2022. doi: <https://doi.org/10.1029/2021JE006973>.
- P. B. Rhines. Waves and turbulence on a beta-plane. *Journal of Fluid Mechanics*, 69(3):417–443, 1975. doi: 10.1017/S0022112075001504.

## Bibliography

---

- A. C. Riddle and J. W. Warwick. Redefinition of system iii longitude. *Icarus*, 27(3):457–459, 1976. doi: [https://doi.org/10.1016/0019-1035\(76\)90025-7](https://doi.org/10.1016/0019-1035(76)90025-7).
- C. Salyk, A. P. Ingersoll, J. Lorre, A. Vasavada, and A. D. Del Genio. Interaction between eddies and mean flow in Jupiter’s atmosphere: Analysis of Cassini imaging data. *Icarus*, 185:430–442, 2006. doi: 10.1016/j.icarus.2006.08.007.
- A. Sanchez-Lavega, J. F. Rojas, and P. V. Sada. Saturn’s zonal winds at cloud level. *Icarus*, 147(2):405–420, 2000. doi: <https://doi.org/10.1006/icar.2000.6449>.
- N. Schaeffer. Efficient spherical harmonic transforms aimed at pseudospectral numerical simulations. *Geochemistry, Geophysics, Geosystems*, 14:751–758, 2013. doi: 10.1002/ggge.20071.
- M. Schöttler and R. Redmer. Ab initio calculation of the miscibility diagram for hydrogen-helium mixtures. *Phys. Rev. Lett.*, 120:115703, 2018. doi: 10.1103/PhysRevLett.120.115703.
- S. Sharan, B. Langlais, H. Amit, T. Erwan, M. Pinceloup, and O. Verhoeven. The internal structure and dynamics of Jupiter unveiled by a high-resolution magnetic field and secular variation model. *Geophysical Research Letters*, 49, 2022. doi: 10.1029/2022GL098839.
- A. A. Simon, M. H. Wong, and G. S. Orton. First Results from the Hubble OPAL Program: Jupiter in 2015. *ApJ*, 812(1):55, 2015. doi: 10.1088/0004-637X/812/1/55.
- E. J. Smith, L. Davis, D. E. Jones, P. J. Coleman, D. S. Colburn, P. Dyal, and C. P. Sonett. Saturn’s magnetic field and magnetosphere. *Science*, 207(4429):407–410, 1980. doi: 10.1126/science.207.4429.407.
- S. Stanley. A dynamo model for axisymmetrizing Saturn’s magnetic field. *Geophys. Res. Lett.*, 37:L05201, 2010. doi: 10.1029/2009GL041752.
- S. Stanley and A. Mohammadi. Effects of an outer thin stably stratified layer on planetary dynamos. *Physics of the Earth and Planetary Interiors*, 168(3):179–190, 2008. doi: <https://doi.org/10.1016/j.pepi.2008.06.016>.
- D. J. Stevenson. Solubility of helium in metallic hydrogen. *Journal of Physics F: Metal Physics*, 9(5):791, 1979. doi: 10.1088/0305-4608/9/5/007.
- D. J. Stevenson. Reducing the non-axisymmetry of a planetary dynamo and an application to Saturn. *Geophysical and Astrophysical Fluid Dynamics*, 21:113–127, 1982.
- D. J. Stevenson and E. E. Salpeter. The dynamics and helium distribution in hydrogen-helium fluid planets. *ApJS*, 35:239–261, 1977. doi: 10.1086/190479.
- A. Sánchez-Lavega, R. Hueso, S. Pérez-Hoyos, and J.F. Rojas. A strong vortex in Saturn’s south pole. *Icarus*, 184(2):524–531, 2006. doi: <https://doi.org/10.1016/j.icarus.2006.05.020>.

- A. Sánchez-Lavega, T. del Río-Gaztelurrutia, R. Hueso, S. Pérez-Hoyos, E. García-Melendo, A. Antuñano, I. Mendikoa, J. F. Rojas, J. Lillo, D. Barrado-Navascués, J. M. Gomez-Forrellad, C. Go, D. Peach, T. Barry, D. P. Milika, P. Nicholas, and A. Wesley. The long-term steady motion of Saturn's hexagon and the stability of its enclosed jet stream under seasonal changes. *Geophysical Research Letters*, 41(5):1425–1431, 2014. doi: <https://doi.org/10.1002/2013GL059078>.
- A. Sánchez-Lavega, L. A. Sromovsky, A. P. Showman, A. D. Del Genio, R. M. B. Young, R. Hueso, E. Garcia-Melendo, Y. Kaspi, G. S. Orton, N. Barrado-Izagirre, D. S. Choi, and J. M. Barbara. *Gas giants*, pages 72–103. Cambridge University Press, 2019. doi: 10.1017/9781107358225.005.
- S. Takehiro. Penetration of alfvén waves into an upper stably-stratified layer excited by magnetoconvection in rotating spherical shells. *Physics of the Earth and Planetary Interiors*, 241:37–43, 2015. doi: <https://doi.org/10.1016/j.pepi.2015.02.005>.
- S. Takehiro and J. R. Lister. Penetration of columnar convection into an outer stably stratified layer in rapidly rotating spherical fluid shells. *Earth and Planetary Science Letters*, 187(3):357–366, 2001. doi: [https://doi.org/10.1016/S0012-821X\(01\)00283-7](https://doi.org/10.1016/S0012-821X(01)00283-7).
- S. Takehiro and J. R. Lister. Surface zonal flows induced by thermal convection trapped below a stably stratified layer in a rapidly rotating spherical shell. *Geophysical Research Letters*, 29(16):50–1–50–4, 2002. doi: <https://doi.org/10.1029/2002GL015450>.
- S. Takehiro and Y. Sasaki. Penetration of steady fluid motions into an outer stable layer excited by mhd thermal convection in rotating spherical shells. *Physics of the Earth and Planetary Interiors*, 276:258–264, 2018. doi: <https://doi.org/10.1016/j.pepi.2017.03.001>.
- A. Tilgner. Spectral methods for the simulation of incompressible flows in spherical shells. *International Journal for Numerical Methods in Fluids*, 30(6):713–724, 1999. doi: [https://doi.org/10.1002/\(SICI\)1097-0363\(19990730\)30:6<713::AID-FLD859>3.0.CO;2-Y](https://doi.org/10.1002/(SICI)1097-0363(19990730)30:6<713::AID-FLD859>3.0.CO;2-Y).
- J. Tollefson, M. H. Wong, I. de Pater, A. A. Simon, G. S. Orton, J. H. Rogers, S. K. Atreya, R. G. Cosentino, W. Januszewski, R. Morales-Juberías, and P. S. Marcus. Changes in Jupiter's Zonal Wind Profile preceding and during the Juno mission. *Icarus*, 296:163–178, 2017. doi: 10.1016/j.icarus.2017.06.007.
- J. Verhoeven and S. Stellmach. The compressional beta effect: A source of zonal winds in planets? *Icarus*, 237:143–158, 2014. doi: 10.1016/j.icarus.2014.04.019.
- Johannes W., C. A. Jones, and K. Zhang. Instability of zonal flows in rotating spherical shells: An application to Jupiter. *Icarus*, 155(2):425–435, 2002. doi: <https://doi.org/10.1006/icar.2001.6733>.
- S. M. Wahl, W. B. Hubbard, B. Militzer, T. Guillot, Y. Miguel, N. Movshovitz, Y. Kaspi, R. Helled, D. Reese, E. Galanti, S. Levin, J. E. Connerney, and S. J. Bolton. Comparing Jupiter interior structure models to Juno gravity measurements and the role of a dilute

- core. *Geophysical Research Letters*, 44(10):4649–4659, 2017. doi: <https://doi.org/10.1002/2017GL073160>.
- J. Wicht. Inner-core conductivity in numerical dynamo simulations. *Physics of the Earth and Planetary Interiors*, 132(4):281–302, 2002. doi: 10.1016/S0031-9201(02)00078-X.
- J. Wicht and U. R. Christensen. Torsional oscillations in dynamo simulations. *Geophysical Journal International*, 181(3):1367–1380, 2010. doi: 10.1111/j.1365-246X.2010.04581.x.
- J. Wicht, T. Gastine, L. D. V. Duarte, and W. Dietrich. Dynamo action of the zonal winds in Jupiter. *A&A*, 629:A125, 2019. doi: 10.1051/0004-6361/201935682.
- J. Wicht, W. Dietrich, P. Wulff, and U. R Christensen. Linking zonal winds and gravity: the relative importance of dynamic self-gravity. *Monthly Notices of the Royal Astronomical Society*, 492(3):3364–3374, 2020. doi: 10.1093/mnras/staa036.
- P. N. Wulff, W. Dietrich, U. R. Christensen, and J. Wicht. Zonal winds in the gas planets driven by convection above a stably stratified layer. *Monthly Notices of the Royal Astronomical Society*, 517(4):5584–5593, 2022. doi: 10.1093/mnras/stac3045.
- K. Zhang, D. Kong, and G. Schubert. Thermal-gravitational wind equation for the wind-induced gravitational signature of giant gaseous planets: Mathematical derivation, numerical method, and illustrative solutions. *The Astrophysical Journal*, 806(2):270, 2015. doi: 10.1088/0004-637X/806/2/270.
- V. N. Zharkov and V. P. Trubitsyn. *Physics of planetary interiors*. Pachart Pub. House, 1978.

## Appendix to Chapter 3

### Radial Grid-point Redistribution

The collocation points are redistributed by the following function:

$$r = \frac{1}{2} \left[ \alpha_2 + \frac{\tan[\lambda(r_{cheb} - x_0)]}{\alpha_1} \right] + \frac{r_i + r_o}{2} \quad (2)$$

where  $r_{cheb}$  are the Gauss-Lobatto collocation points and  $r_{cheb} \in [-1, 1]$ . The three parameters are:

$$\lambda = \frac{\tan^{-1}(\alpha_1(1 - \alpha_2))}{1 - x_0}, \quad x_0 = \frac{K - 1}{K + 1}, \quad K = \frac{\tan^{-1}(\alpha_1(1 + \alpha_2))}{\tan^{-1}(\alpha_1(1 - \alpha_2))} \quad (3)$$

where we use  $\alpha_1 = 2$ ,  $\alpha_2 = -0.2$ .

# Acknowledgements

I have to begin by giving my deepest thanks to Wieland Dietrich. Without him, this project is likely to have fallen prey to the surreal times that lasted for the first 2 years of my Ph.D. It is thanks to him that now, after 1.5 much more cheerful years, I can say that this has been one of the best experiences of my life. There were too many days to count where he would be the only real-life person I would converse with, when fleeing home-office to the institute. He kept me sane, kept the project rolling - albeit slowly - and kept my love of science alive. I cannot express how grateful I am for the support he has given me over these years and the time he has always selflessly offered has not gone unappreciated.

Next, I must thank Uli Christensen. I am forever grateful for your extraordinary patience in those first two years and the heartening encouragement you gave when things were finally happening. From you I have learnt to keep asking questions and always search for the simplest ways to approach a problem. I hope to be lucky enough to gain even just a tiny fraction of his wisdom over the years.

I also want to thank Johannes Wicht, for the countless hours of discussion. He reminded me that to fully understand a problem it is always worth taking the time to get to the solutions yourself and no amount of textbooks will do that for you.

I thank Vincent Böning and Jörn Warnecke for reminding me to keep thinking about my work in a wider context (or at least that it's worthwhile trying to make it interesting for Sun-people every now and again). Vincent also gave me a sense of solidarity, attempting to get to grips with a new topic and a new code in a group of experts. Jörn I thank for his absolutely incredible help with getting this thesis in a readable shape.

Ankit Barik has played an important role in this final year. The week we finally met in person he made my first AGU an absolutely wonderful experience. Doing a Ph.D. in these times meant that it took until the final year to actually meet people and having him by my side made it feel like a breeze. The advice and friendship he has given me since then has inspired me and makes me look forward to the next years.

Onto the people that have made Göttingen feel like a home these last years. I have to thank Tanay, both for discovering running with me and being such a good friend. Our Thursdays became a fixed point in a week for me. Sometimes they became chats about life, sometimes the outlet to rant about work and sometimes it was whooping with exhilaration while sprinting through a blizzard. If it hadn't been for you I would never have considered signing up for that first marathon (or the second, or the ultra...). Thank you for helping to keep me sane.

I would also like to thank the rest of the Ph.D.'s here, Jonas (even though you made me student rep), Dusan, Argiris, Amanda and all the others. I am forever grateful for the sense of community you gave me here.

I am grateful for my rowing friends, in particular Juliane and Gesa. The peace and

## Acknowledgements

---

companionship of being on the water together, oblivious to the rest of the world, for even just a few hours on a weekend always kept me grounded.

Some friends I did not have enough time with the last four years, but who I knew were always there for me. Kathryn, I cannot thank you enough for your support and friendship. Thank you also to all my other Cambridge friends who always did their best to bridge the distance between us.

And finally, I would like to thank my mum and dad. It's been some tough years in many ways and I could never have done it all without your ceaseless love, support and guidance.

# Publications and Presentations

## Publications

**P. Wulff**, U.R. Christensen, W. Dietrich, J. Wicht.

The Effects of a Stably Stratified Region with radially varying Electrical Conductivity on the Formation of Zonal Winds on Gas Planets.

Submitted to Journal of Geophysical Research: Planets (2023).

V.G.A. Böning, **P. Wulff**, W. Dietrich, J. Wicht, U.R. Christensen.

Direct driving of simulated planetary jets by upscale energy transfer.

A&A, 670 (2023) A15. <https://doi.org/10.1051/0004-6361/202244278>

**P. Wulff**, W. Dietrich, U.R. Christensen, J. Wicht.

Zonal winds in the gas planets driven by convection above a stably stratified layer.

MNRAS, Volume 517, Issue 4, December 2022, Pages 5584–5593, <https://doi.org/10.1093/mnras/stac3045>

W. Dietrich, **P. Wulff**, J. Wicht, U.R. Christensen.

Linking zonal winds and gravity – II. Explaining the equatorially antisymmetric gravity moments of Jupiter.

MNRAS, Volume 505, Issue 3, August 2021, Pages 3177–3191, <https://doi.org/10.1093/mnras/stab1566>

J. Wicht, W. Dietrich, **P. Wulff**, U.R. Christensen.

Linking zonal winds and gravity: the relative importance of dynamic self-gravity.

MNRAS, Volume 492, Issue 3, March 2020, Pages 3364–3374, <https://doi.org/10.1093/mnras/staa036>

## Presentations

**P. Wulff**, U.R. Christensen, W. Dietrich, J. Wicht.

The Effects of a Stably Stratified Region on the Formation of Zonal Winds on Gas Planets.

EGU 2023. <https://doi.org/10.5194/egusphere-egu23-15308>.

**P. Wulff**, W. Dietrich, U.R. Christensen, J. Wicht.

Transition into Dynamo Region or Sub-Adiabaticity? Relevance and Evidence of Damping Mechanisms for Zonal Jets on Giant Planets.

AGU Fall Meeting 2022.

**P. Wulff**, W. Dietrich, U.R. Christensen, J. Wicht.

Zonal winds in the gas planets driven by convection above a stably stratified layer.

EGU 2022. <https://doi.org/10.5194/egusphere-egu22-9684>.

# Curriculum Vitae

**Name:** Paula Naomi Wulff

**Date of Birth:** 12.12.1995

**Nationality:** German

## Education

### Doctoral candidate

2020 - 2023

University of Göttingen

Göttingen, Germany

In the International Max Planck Research School (IMPRS) framework at the Max Planck Institute for Solar System Research.

*Thesis Title:* Numerical Modelling of Zonal Winds in Gas Planets.

*Supervisors:* Ulrich Christensen, Johannes Wicht, Wieland Dietrich and Andreas Tilgner

### MSc in Physics

2017 - 2020

University of Göttingen

Göttingen, Germany

*Thesis Title:* Zonal Wind-induced Gravity Anomalies

*Supervisors:* Ulrich Christensen, Johannes Wicht and Wieland Dietrich

### BA in Natural Sciences

2014 - 2017

University of Cambridge, Churchill College

Cambridge, UK Specialising in Physics

### High School

2007 - 2014

Belvedere Academy

Liverpool, UK